Ultrafast Time-Resolved and Spin-Dependent Photocurrent Studies in Topological Insulators

By

HENRY CLARK TRAVAGLINI

DISSERTATION

Submitted in partial satisfaction of the requirements for the degree of

DOCTOR OF PHILOSOPHY

in

Physics and Astronomy

in the

OFFICE OF GRADUATE STUDIES

of the

UNIVERSITY OF CALIFORNIA

DAVIS

Approved:

Dong Yu, Chair

Inna Vishik

Gergely Zimanyi

Committee in Charge

2023

Abstract

Bismuth selenide is a prototypical topological insulator, which is a remarkable class of materials due to their linear dispersion relation owing to their time-reversal symmetry-protected Dirac cones. Recently, antimony-doped bismuth selenide MOSFETs grown by chemical vapor deposition have displayed millimeter-long diffusion lengths at cryogenic temperatures with a tunable chemical potential. Motivated by the hypothesis that these highly extended and efficient photocurrents are reliant on the topological surface states, I will discuss recent experiments to probe this observation through several avenues: first, by creating MOSFET architecture that allows us to locally gate the chemical potential; second, through ultrafast photocurrent studies achieved with a Ti:sapphire laser to dramatically modulate the carrier concentration; third, by studying illuminated magnetotransport studies to shed light on contributions to weak antilocalization; fourth, through a tandem approach of experimental and theoretical investigations into the excitations generated through helical radiation. Our results provide clues about the nature of the carriers responsible for these uniquely nonlocal photocurrents which may be due to the carrier states forming an exciton condensate.

Acknowledgements

Many people have helped me become the person I am today. A smaller subset of these folks have, for reasons that are sometimes mysterious to me, refused to stop believing in my improvement as a scientist and human being.

Many PIs who wield great power have been very important in my education. I'd like to thank my advisor, Dr. Dong Yu, for his steadfast patience and advice over the course of this degree. He has truly shown the patience of Job, and has also helped me become a more confident scientific writer and communicator. Dr. Wei Pan, at Sandia National Labs, has taught me much about the fine details of magnetotransport and cryogenic systems. I am eternally grateful for the opportunity to become acquainted with the Lab and the kind and thoughtful people who work within it. Dr. Gergely Zimanyi and Dr. Inna Vishik agreed to read this dissertation, and in addition to this selfless act, have also given me good advice inside the classroom (in 240C and Spectroscopies of Quantum Materials) and outside it.

Coworkers are the people who make a workplace tolerable, and I have been very fortunate to work with fellow graduate students who are frighteningly brilliant *and* well-adjusted. Dr. Luke McClintock, Bob Wang, Dr. Yasen Hou, Tony Song, and Rodrigo Becerra Silva have been wonderful to work with. I also have been privileged to work with some brilliant undergraduate students: Jay Huang, Yuqing Zhu, Mykyta Dementyev, and Rongqing Shang are all future tastemakers and I will follow their trajectories with the same great interest that they have shown me.

Many people have helped me at UC Davis who are not physics PhDs or physics PhD candidates, too! The CNM2 staff has been fantastic to learn from: Ryan Anderson, Paula Lee, Dr. Chan Ho Kim, Dr. Vishal Narang, Dr. Yusha Bey, and Dr. Rand Jean have been instrumental in developing my skills with cleanroom process development. The crew at the machine shop in Crocker Nuclear Lab, with Dave Hemer in particular, provided me with a safe space (well, actually a very dangerous space) to use my brain in new ways. The staff in the business office are the unsung heroes of the physics department and perhaps saved me from my own absentmindedness more so than anyone else on this list: Gwen Prezler, Falicia Savala, and Lenna Crabbe-Charlesworth have been especially helpful.

My family deserves the most credit in making this frivolous pursuit of knowledge possible. My parents John and Kris, my sister Grace, and my partner Lynae have shown me a well of love and support that cannot be described with words or equations.

9

I am a keeper of sheep.
The sheep are my thoughts
And my thoughts are all sensations.
I think with my eyes and my ears
And with my hands and feet
And with my nose and mouth.

To think a flower is to see it and smell it
And to eat a fruit is to know its meaning.

That's why on a warm day
I feel sad because I enjoy it so much,
And stretching out on the grass,
And closing my hot eyes,
I feel my whole body lying stretched out on reality,
I know the truth and I am happy.

-Fernando Pessoa

Table of Contents

List of Acronyms

2-DEG = Two-dimensional electron gas

MBE = Molecular beam epitaxy

ARPES = Angle resolved photoemission spectroscopy

HDPC = Helicity-dependent photocurrent

SHE = Spin Hall effect

SNL = Sandia National Laboratory

SPCM = Scanning photocurrent microscopy

STM = Scanning tunneling spectroscopy

EQE = External quantum efficiency

ISHE = Inverse spin Hall effect

IQE = Internal quantum efficiency

MOSFET = Metal-oxide-semiconductor field effect transistor

VLSCVD = Vapor-liquid-solid chemical vapor deposition

TI = Topological insulator

PISHE = Photo-induced spin Hall effect

QWP = Quarter waveplate

QL = Quintuple layer

HWP = Half waveplate

List of Figures

List of Tables

Chapter 1

Introduction

The invention of computation is one of humankind's great intellectual achievements. As the size of transistors approaches the atomic limit, deviations from Moore's law–the prediction that the number of transistors on an integrated circuit doubles every two years–will fail[2]. In order to continue to innovate, we must look beyond the goal of shrinking the transistor and explore new foundations for device physics.

Research activities in physics in the 21st century have been marked by a rapid exploration of these new foundations through a wide variety of approaches. From the fabrication of traditional transistor structures with exotic materials such as quantum dots[3–5], graphene[6–8], and transition metal dichocalgindes[9]; to the invention of completely new paradigms such as spin-[10,11] and valley-tronics[12,13] that can enable quantum computing[14]. These new efforts are enabled by advances in materials synthesis processes, like molecular beam epitaxy (MBE)[15,16], vapor-liquid-solid chemical vapor deposition (VLSCVD)[17] and sputtering[18]; these are in turn investigated by modern spectroscopic techniques like scanning tunneling microscopy (STM)[19–21], angle-resolved photoemission spectroscopy (ARPES)[22], and scanning photocurrent microscopy (SPCM)[23,24]. Indeed, nature has provided us with a rich landscape from which the next limits of human enterprise will arise.

In this dissertation, we will examine a small corner of this landscape through a single lens: the topological insulator (TI) bismuth selenide (Bi_2Se_3) through optical interactions. We will first introduce Bi_2Se_3 as a resident of the class of topological quantum materials. Then, we will discuss efforts of ultrafast photocurrent studies, followed by illuminated magnetic field-dependent studies, and then completed with polarization-dependent photocurrent studies

Despite Bi_2Se_3's status as a well-studied canonical material, it still contains plenty of secrets that may help elucidate the deep mysteries of nature.

1.1 Topology: The Link Between 20th and 21st Century Condensed Matter Physics

1.1.1 Topology in Condensed Matter Phyiscs

What is topology? Let's first imagine that we're in a foreign, vaguely hostile place: a mathematics department. Here, people talk about topological invariants as objects that retain some property under a *homeomorphisms*, which describe a function that allows you to continuously deform an object from one shape to another without cutting or tearing. One famous homeomorphism, present in perhaps thousands of dissertations and talks, describes shaping a doughnut into a cup of coffee. This is an example of a *genus 1* object under a homeomorphism, where the genus roughly describes the number of "holes" in an object[26] (fig 1.1). Regardless of which homeomorphism you apply to an object, the genus will be invariant. In plain speech, the number of holes in an object will remain the same no matter how you stretch and shape it.

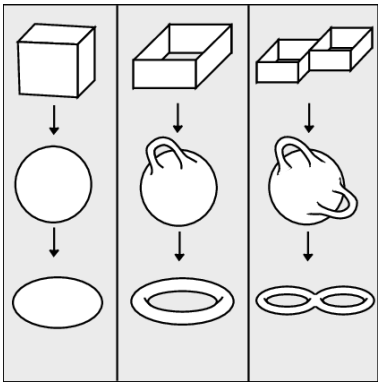

Figure 1.1: From left to right: homeomorphisms for objects of genus 0, genus 1, and genus 2. Figure adapted from[25].

In physics, the applications of topology are manyfold. When discussing electronic structure in condensed matter physics, concepts from topology are frequently used to generically characterize observable quantities that are invariant under changes with their generating Hamiltonian. The quantum Hall effect is a wonderful example of this picture, which describes very precisely quantized conductance values that are invariant under changes to the Hamiltonian of the system.

1.1.2 Quantizing the Hall Effect

The Hall effect, discovered in 1879 by Edwin Hall[27] while attempting to complete his PhD, describes the effect of a transverse voltage that results from electronic transport perpendicular to a magnetic field (fig 1.2). A current in a perpendicular magnetic field will experience the Lorentz force:

$$\mathbf{f} = \rho\mathbf{E} + \mathbf{J} \times \mathbf{B}. \tag{1.1}$$

The conductivity (σ) and resistivity (ρ) will be generically described by tensors because of the mixing of components from the cross product in the Lorentz force:

$$J_\mu = \sigma_{\mu\nu} E_\nu \tag{1.2}$$

$$E_\mu = \rho_{\mu\nu} J_\nu \tag{1.3}$$

If $\mathbf{B} = B_0\hat{\mathbf{z}}$, $\mathbf{J} = J_0\hat{\mathbf{x}}$, and we apply the steady state condition ($\mathbf{f} = 0$) to guarantee that there is no current in the $\hat{\mathbf{y}}$ direction, we must have

$$\rho_{xy} = \frac{B}{nq} = R_H, \tag{1.4}$$

which tells us that the transverse resistivity is linearly dependent on the magnetic field B, up to a constant determined by the carrier capacity n and charge sign q. This quantity, also known as the Hall resistance, can tell an experimenter direct information about the carrier

density and charge sign. The classical Hall effect is thus extremely useful, and has countless applications in materials science and electrical engineering for both material characterization[28] and device applications[29].

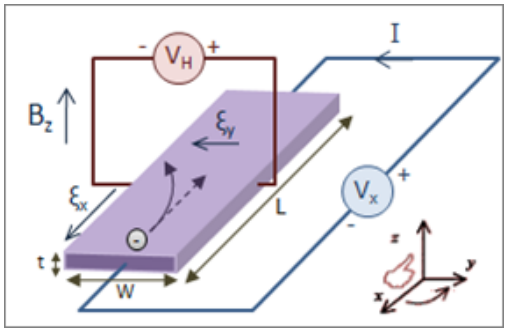

Figure 1.2: Schematic set up for classical Hall effect measurement, depicting the deflection of a charge current in an applied magnetic field. Adapted from[30].

The quantum Hall effect was discovered in 1980 by Klaus von Klitzing, Micael Pepper, and Gerhard Dorda[31]. They observed that low temperature two dimensional electron gases (2DEGs) would display a Hall coefficient that showed quantum Hall plateaus (fig 1.3)

$$R_H = \frac{1}{\nu}\frac{h}{e^2}, \tag{1.5}$$

where ν is an integer. Accompanying these plateaus is a vanishing longitudinal resistance:

$$R \propto \rho_{xx} \longrightarrow 0. \tag{1.6}$$

An amazing feature of these plateaus is that the integer ν is extremely precise, to an experimental precision of about 10^{-9}[33]! The value e^2/h is the quanta of conductance, which in a quantum Hall state can be scaled by an integer value. This quantized value is ignorant of experimental details like scattering time or magnetic field (in some neighborhood of B). This is a classic example of concepts from topology appearing in condensed matter physics. Making the correspondence more explicit, the Hall conductance has another name as the first Chern number of the filled Bloch band[33], which is a topological invariant that can be calculated a priori of an experiment.

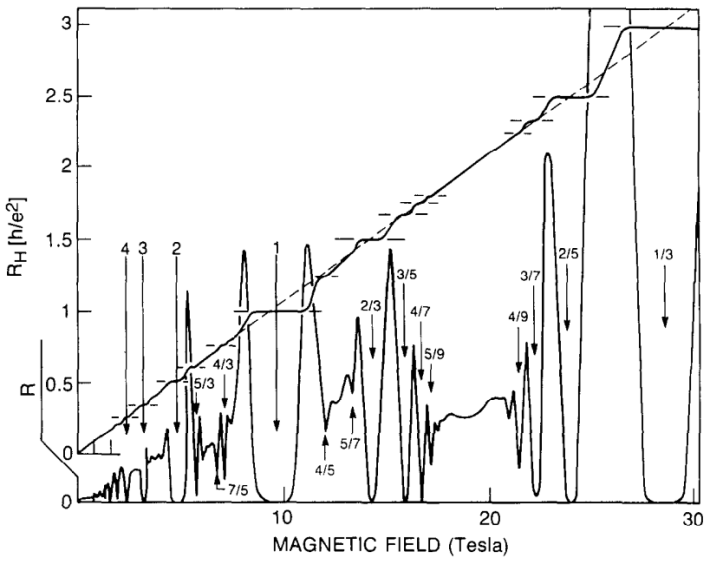

Figure 1.3: Hall coefficient and longitudinal resistance of a 2DEG in an external magnetic field, displaying quantized Hall plateaus and their associated dissipationless transport. Adapted from[32].

Shortly after the quantum Hall effect was discovered, Daniel Tsui, Horst Stormer, and Arthur Gossard[34] reported measurements in similar systems that displayed fractional values for ν. But that story is beyond the scope of this dissertation as the author does not wish to bore the reader.

1.1.3 Topological Quantum Materials

The quantum Hall effect and its associated state are the progenitors of the broader landscape of topological quantum materials. This is an extremely broad class of materials that includes, insulators, superconductors, semimetals, semiconductors, *whatever*. Topological materials are broadly unified in their mathematical classification by the calculation of topological invariants, which can take the form of an integer: Z (also known as the Chern number[35], which was previously discussed in the context of the quantum Hall effect–which is a state that is ignorant to (small) changes in magnetic field) calculated by integrating the Berry curvature over the Brillouin zone[36], or Z_2, which describe topological insulators and can be calculated by different methods depending on if the material has inversion symmetry[37] or not[38].

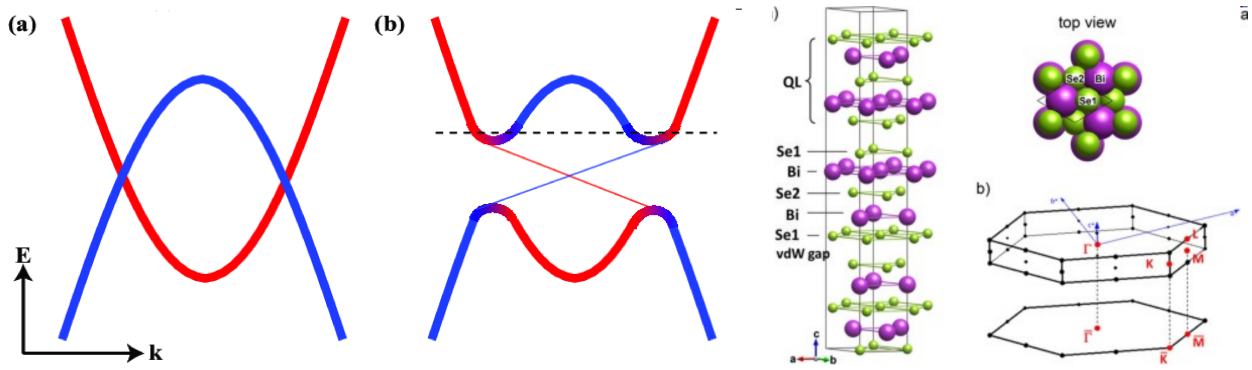

Figure 1.4: Left: effects of spin-orbit coupling on band inversion, where trivial gapless bands (a) are modified by spin-orbit coupling to open a gap with surface states (b). Figure sourced from [39]. Right: quintuple layer arrangement and Brillouin zone of bismuth selenide. Figure sourced from [40].

1.1.4 Topological Insulators

TIs are a class of materials that feature insulating behavior in the bulk states, and metallic topological surface states (TSSs). These TSSs have linear dispersion relationships, a vanishing density of states near the bandgap, and spin-momentum locking of charge carriers that suppress backscattering. The origin of the TSS comes from a combination of band inversion and strong spin-orbit coupling, illustrated in figure 1.4. Without spin-obit coupling, the conduction and valence band in bismuth selenide will cross and form a trivial conductor– this can be modeled with DFT calculations using the bismuth and selenium orbitals and no spin-orbit coupling [41]. When spin-orbit coupling is introduced, a gap is opened and we are left with a conduction band that has contributions from the valence band (and vice versa) [42]. This form of band inversion is *not* necessarily topological! To confirm that there is indeed topological order, one must confirm that the Z_2 invariants are nonzero. If you find that the Z_2 invariants are nonzero, then congratulations! You have a topologically ordered bulk! The vacuum is *not* topologically ordered, which means you must close this gap at the boundary between the crystal and the vacuum– which provides a plausibility argument for the metallic nature of surface states in TIs.

1.2 Bismuth Selenide

One very popular example of this class of materials is Bi_2Se_3-sometimes referred to as the hydrogen atom of its material family, after its relatively simple features, where the band inversion is easy to identify. Other features include a single non-degenerate Dirac cone, and bulk states with a large direct bandgap of 0.3 eV, which in turn make separating the electrical conduction of the bulk states and the TSSs viable–but still challenging.

Bismuth selenide is easy to exfoliate because crystals are formed by quintuple layers of atoms weakly held together with a van der Waals force.

1.2.1 Bismuth Selenide and Doping Control

Even though Bi_2Se_3 has a simple band structure, there are still fundamental challenges that must be overcome in order to reveal its secrets. Primarily, bulk states are difficult to separate from the TSSs in stochiometric bismuth selenide, since the Fermi level lies within the bulk conduction band due to naturally occurring selenium vacancies. This can be overcome by a tandem strategy of electrostatic gating and chemical doping, which can lower the Fermi level to a region closer to the Dirac point (fig. 1.5). Additionally, nanostructure devices will have a generically weaker bulk conductivity due to the increased surface-to-volume ratio, and can even exhibit quantum confinement effects for sufficiently thin devices[44]–but not too thin, for the Dirac cones on the top and bottom surface state will hybridize and open a gap when the crystal is six quintuple layers or thinner[45].

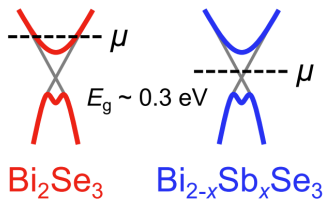

Figure 1.5: Antimony doping will lower the chemical potential in bismuth selenide. Sourced from[43].

1.2.1.1 Atimony as a Dopant

Antimony can be chemically substituted for bismuth during the growth process without fundamentally changing the TSSs[46] because they are isovalent elements. Because antimony is smaller, it has a tendency to mitigate the degenerate doping effects of selenium vacancies and therefore lowers the Fermi level[47].

Because Sb_2Se_3 is a trivial insulator[48], a sufficient amount of Sb substitution will cause a metal-insulator transition where the TSSs vanish[49]. Experimental results show that these effects may occur in $Bi_{2-x}Sb_xSe_3$ at Sb substitutions as low as 20%[50] or 30$[51].

The Yu lab has developed a recipe for antimony-doped bismuth selenide nanoribbons and nanoplates via the vapor-liquid-solid technique, which has its chemical structure and composition confirmed via x-ray diffraction and energy dispersive X-ray spectroscopy. At an atomic percentage of roughly 6-7% antimony, we found that the metal-oxide-semiconductor field effect transistor (MOSFET) devices displayed an extended photocurrent, which had not previously been reported in any topological insulator system[52]. Prior to this initial study, only rapidly decaying local photocurrent had been observed[53,54].

1.3 Stealing from the Engineers to do Physics: Device Fabrication

The Yu lab is unique at Davis due to its strongly vertically integrated workflow: graduate students are responsible for every single part of an experiment's life cycle–from crystal growth to device fabrication, and from optical data acquisition to analysis and modeling. Most of the methods of our device fabrication techniques are borrowed from work originally crafted by engineering and materials science groups. In general, our devices are grown by either solution methods (used for our perovskite research program[55,56]), or by chemical vapor deposition systems (used for our inorganic material research programs[57]). These crystals are then transferred to silicon chips to be fabricated into metal-oxide-semiconductor field effect transistors (MOSFETs).

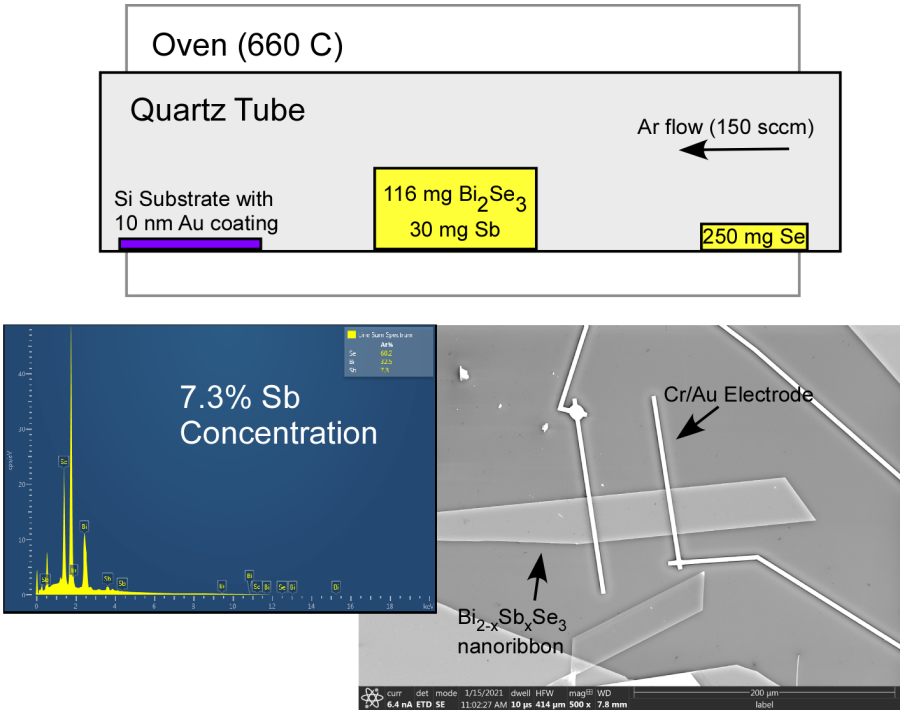

Figure 1.6: Top: schematic of CVD growth method, with locations of precursors and growth substrates. Bottom left: electron dispersive x-ray spectroscopy that identifies large antimony substitution in bismuth selenide. Bottom right: as-fabricated bismuth selenide MOSFET.

1.3.1 Crystal Growth and MOSFET fabrication

While Bi_2Se_3 does have a nonzero bulk bandgap, its small size (0.3eV) makes decoupling the trivial bulk states from the interesting topological surface states. One strategy to mitigate the bulk contribution is to study micro- and nano-scale samples. In the Yu lab, our main strategy is to grow microcrystals via VLSCVD techniques. Other growth techniques such as MBE[58], solution-based growths[59], and sputtering[60] can be used as well. VLSCVD methods are relatively cheap and straightforward to operate but suffer from reproducibility issues. Our general strategy for chemical vapor deposition is centered around reducing n-type selenium vacancies so that our devices are as intrinsic as possible.

Our crystals are grown from bulk Bi_2Se_3 precursors (ThermoScientific Chemicals, Vacuum Deposition Grade, 99.999%), antimony powder (ThermoScientific Chemicals, -200 mesh, 99.999%), and selenium shot (ThermoScientific Chemicals, 2-6mm, 99.999%). The

bulk bismuth selenide (116 mg) and antimony precursors (35 mg) are placed in a quartz boat in the middle of the oven (set as a reference point to 20 mm on a ruler), the growth substrates (Si or SiO2 wafer with 10 nm of Au deposited via E-Beam evaporation) are placed downstream (the edge closest to the bulk precursors should be at 8 mm on the ruler), and the excess selenium (five pellets) is placed near the end of the oven upstream (the center of mass should be at 36.5 mm), as shown in the top portion of figure 1.6. The locations of the growth substrate and excess selenium are *critical*: if the substrate is in the wrong location, the effective growth temperature will be incorrect and devices will be of poor quality. If the excess selenium is in the wrong location, then the excess selenium will not evaporate at a uniform rate during the growth and cause an excess of n-type selenium vacancies in the crystals. After loading the oven, the system undergoes three purging cycles where the tube is pumped to 50 mTorr and then filled with pure Ar. After purging is complete, the system is continuously pumped for 2 hours while flowing 150 sccm of Ar to remove adsorbed contaminants. Then, while maintaining the 150 sccm Ar flow, the growth is performed at 680C for four hours at room pressure. More details, including notes on process development, can be found elsewhere[52,61,62].

Growth substrates are removed from the oven after they naturally cool to room temperature. Crystals from the growth substrate are checked with energy dispersive x-ray spectroscopy to confirm that the correct amount of antimony substitution has occurred (7% is generally good, fig. 1.6 bottom left). Crystals are then transferred to a silicon chip with a 300nm SiO_2 gate dielectric. The devices are spin-coated with a trilayer resist coating: two layers of MMA(8.5) MAA EL 9 (Kayaku) as a copolymer, and one layer of 950PMMA C 2 (Kayaku) as a primary resist. Gold electrodes are fabricated through electron beam lithography (5nm of chromium is used as an adhesion layer, followed by a 295nm Au layer) and lift-off is done in gently heated acetone or Remover 1165. Once the chips have completed liftoff they are rinsed with isopropanol (IPA) and dried with anhydrous N_2. It is only now that we have complete MOSFETs, ready for testing (fig. 1.6 bottom right).

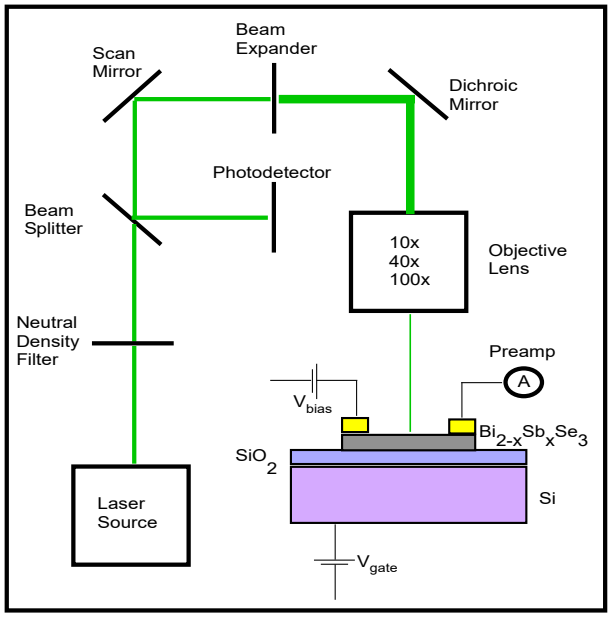

Figure 1.7: Schematic of scanning photocurrent microscopy set up, showing the optical path and incorporation of MOSFET device. The incident angle of the laser on the device can be (with great inconvenience) tuned.

1.4 Illuminating the Behavior of Intrinsic Bismuth Selenide

I will first describe the principle of our main experimental technique of spatially resolved photocurrent and then summarize the initial optoelectronic studies on intrinsic bismuth selenide using scanning photocurrent microscopy performed by my predecessor Dr. Yasen Hou[52].

1.4.1 Scanning Photocurrent Microscopy

Scanning photocurrent microscopy (SPCM) is a powerful tool that is well suited to studying the transport properties of semimetallic and semiconducting materials. SPCM is the practice of raster scanning a focused illumination source (usually a laser) across a device (usually a MOSFET) and recording the electrical current at each point (usually binned in sub-micron-sized pixels).

SPCM is really good at creating spatial maps of charge transport. Consider a laser injection site in an n-type device. This will inject an amount of charge carriers equal to $\Delta p = p - p_0$, where p is the total hole concentration and p_0 is the dark hole concentration.

This modifies the continuity equation (away from the generation point):

$$\frac{\partial p}{\partial t} = \frac{\Delta p}{\tau} - \frac{1}{e}\nabla \cdot \mathbf{j} \tag{1.7}$$

where τ is the hole lifetime. The current density is governed by the drift-diffusion equation

$$\mathbf{j} = ep\mu\mathbf{E} - eD\nabla p. \tag{1.8}$$

where the hole diffusion constant, D_h, is assumed to be given by Einstein relation $D_h = \frac{k_B T}{e}\mu$. Feeding the drift-diffusion equation into the continuity equation gives

$$\frac{\partial p}{\partial t} = \frac{-\Delta p}{\tau_p} - p\mu\frac{\partial E}{\partial x} - E\mu\frac{\partial p}{\partial x} + D_h\frac{\partial^2 p}{\partial x^2}. \tag{1.9}$$

Outside of the device channel, the electric field is zero,

$$\frac{\partial p}{\partial t} = E\mu\frac{\partial p}{\partial x} + D_h\frac{\partial^2 p}{\partial x^2}. \tag{1.10}$$

For scanning rates that are sufficiently slower than the relaxation time of the material (an experimental condition that is practically only not achieved when the device has extreme deep-level traps that artificially extend the lifetime), we have a steady state system such that $\frac{\partial p}{\partial t} = 0$. Looking outside the device channel, we have $\vec{E} = 0$. Additionally, because the dark region of the device have uniform carrier density, we can replace p with Δp to emphasize the change in carrier density. Enforcing these conditions produces

$$\frac{\partial p}{\partial t} = -\frac{\Delta p}{\tau} + D_h\frac{\partial^2 p}{\partial x^2} \tag{1.11}$$

In steady state $\frac{\partial p}{\partial t} = 0$, which implies

$$D_h\frac{\partial^2 p}{\partial x^2} - \frac{\Delta p}{\tau} = 0 \tag{1.12}$$

Solving this differential equation yields

$$\Delta p = \Delta p_0 e^{-\frac{x}{L_d}}, \tag{1.13}$$

which shows that excited minority carriers Δp follow exponential decay in 1D diffusion systems. As a corollary, this also identifies nonlocal transport outside of the device channel as a purely diffusive process. All MOSFET devices we fabricate have parallel electrodes so that any in-channel electric field will be strictly one-dimensional–and therefore easy to fit.

1.4.2 Previous SPCM Results on Bismuth Selenide

I summarize my predecessor Dr. Yasen Hou's results[52] below, which show a photocurrent with remarkable properties at liquid helium temperatures:

1. **Long diffusion length** (fig. 1.8A): the diffusion length at liquid helium temperatures approaches $L_D = 1$mm, which suggests that the carriers are highly delocalized;

2. **High efficiency** (fig. 1.8A): the internal quantum efficiency (the ratio of the number of electrons collected at an electrode to the number of photons absorbed) is greater than 60%, which is also suggestive that the carriers are highly delocalized;

3. **Bias independent photocurrent decay length** (fig. 1.8B): the photocurrent decay length (inside the device channel) is bias independent, which suggests that the carriers are charge neutral;

4. **Gate tunable diffusion length** (fig. 1.8C): while the diffusion length is unperturbed for most gate voltage values (although it is possible to tune the peak photocurrent), large negative values will rapidly localize the photocurrent. This localization occurs when the chemical potential is tuned below the charge neutrality point and hybridizes the surface states with bulk p-type states;

5. **Wavelength independent diffusion length** (fig. 1.8D): this otherwise uninteresting result rules out the possibility of surface plasmon polaritons, which have a wavelength-dependent diffusion length[63];

6. **Intensity-tunable diffusion length** (fig. 1.8E): the diffusion length tends to be suppressed as the excitation power increases (this does *not* require high intensities, appearing at powers as low as 8.6μW with a spot size of 3μm.

We have hypothesized that the delocalized photocurrent is caused by formation of superfluidic-like exciton condensate at low temperatures. The charge-neutral exciton picture is supported by electric field independent transport.

1.5 Exciton Condensation

An exciton is a quasiparticle that describes a bound state between an electron and hole. As a unity-spin quasiparticle, it obeys Bose-Einstein statistics and thus ignores the Pauli exclusion principle. As a result, they may condense into the ground state of the system's Hamiltonian below some critical temperature T_C, analogous to the formation of a superfluid state in He3 or Cooper pairs in conventional superconductors. The condensation of excitons has was predicted in the 1960s[64], and has been conclusively observed in quantum wells[65] and bilayer graphene[66,67]–where the physical separation of electron and hole (in different quantum wells, or in each sheet of graphene) dramatically increases the exciton lifetime. Finding a system with direct excitons that form a condensate has proven to be more challenging. The kicker with the excitonic flavor of condensation is that it involves quasiparticles with an *attractive* interaction, which increases the critical temperature. The general condition for exciton condensation is that Coulomb interactions must be very strong, so screening effects must be weak[68]. This is possible when the Coulomb interaction is large compared to the kinetic energy of the carriers. Materials with Dirac cones are identified as potential candidates for realizing high T_C exciton condensation[1]. In a Dirac material with

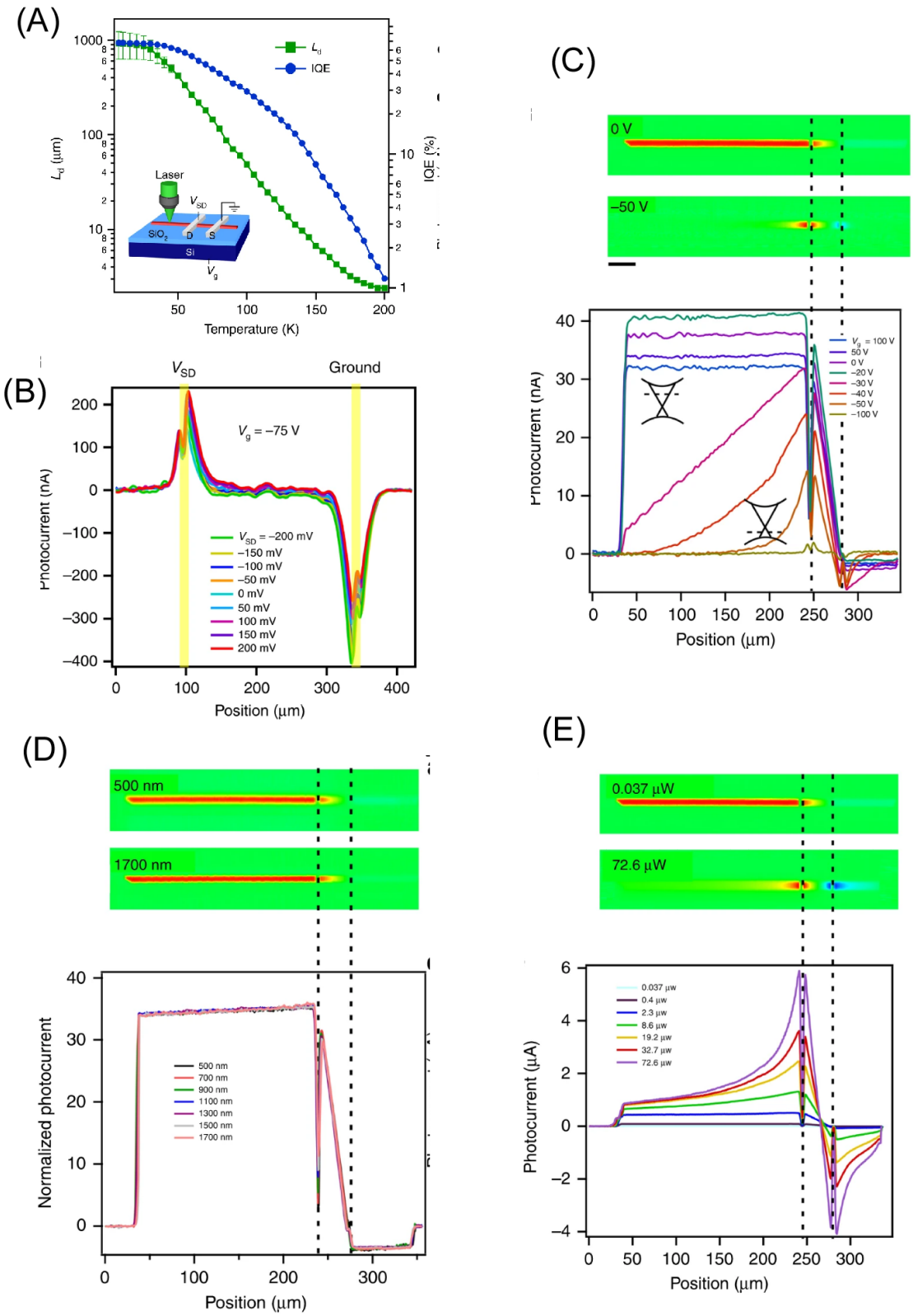

Figure 1.8: (A) Long diffusion length and high quantum efficiency, (B) bias independence of diffusion length, (C) gate driven suppression of diffusion length, (D) wavelength independence of diffusion length, (E) intensity-driven suppression of diffusion length. Figures sourced from [52].

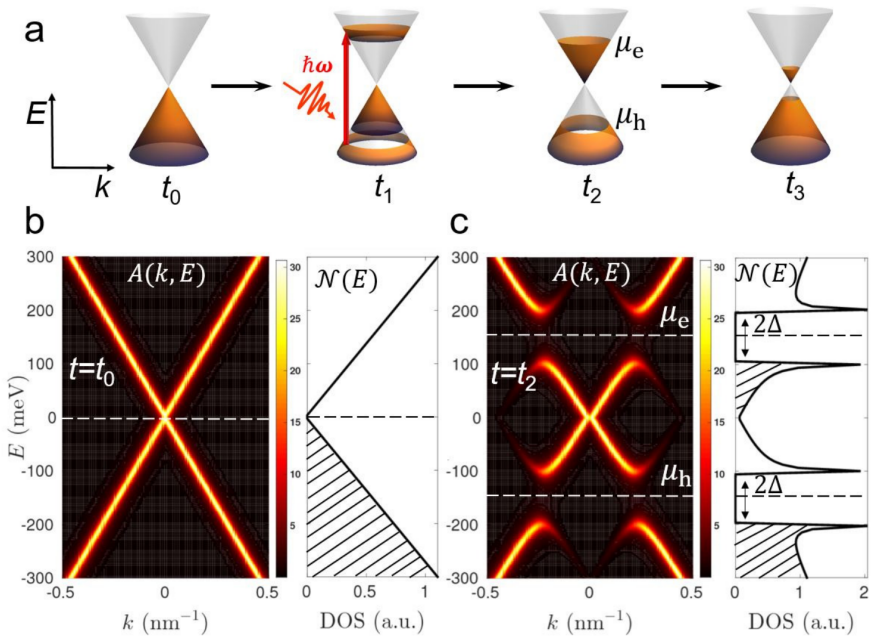

Figure 1.9: (a) Time evolution of optically pumped Dirac cone: t_0 shows occupied states in Dirac cone at equilibrium, t_1 shows occupied states shortly after photon absorption with excited states, t_2 shows formation of separate hole and electron populations with respective chemical potentials, t_3 shows near equilibrium after relaxation; spectral function A(k,E) and of and density of states N(E) before charge pumping (b), and after charge pumping (c), showing gapped spectrum in the latter. Figure sourced from [1].

linear dispersion, the ratio between these two energies can be found by :

$$\alpha = \frac{E_C}{E_K} = \frac{e^2}{\epsilon \hbar^2 v_F} \tag{1.14}$$

Calculations of the α parameter, and resulting chemical potential (μ), lifetime (τ), critical temperature (T_C) and binding energy (Δ) have been systematically performed and reveal 3D TIs to superior candidates [1] to valley degenerate graphene (table 1.1). Keeping the α parameter in mind, the edge from 3D TIs stems from the reduced Fermi velocity and relative permittivity at the surface of a TI compared to graphene. The case of valley selective optical pumping in graphene (which can be accomplished with helicity-dependent light [69]) is important because it illustrates how lifting Dirac cone degeneracies improves Coulomb interactions. Another consideration is the lifetime of excitations in graphene is remarkably

Material Class	α	μ(meV)	τ(ps)	T_C(K)	Δ(meV)
Graphene (Valley degenerate)	0.4-1.0	500	0.1	1.0	0.1
Graphene (Valley selective)	0.4-1.0	500	0.1	6-35	1-5
3D TI	0.1-1.0	100	1-10^6	0-30	0-3

Table 1.1: Calculated exciton condensation parameters for graphene and 3D TIs from [1].

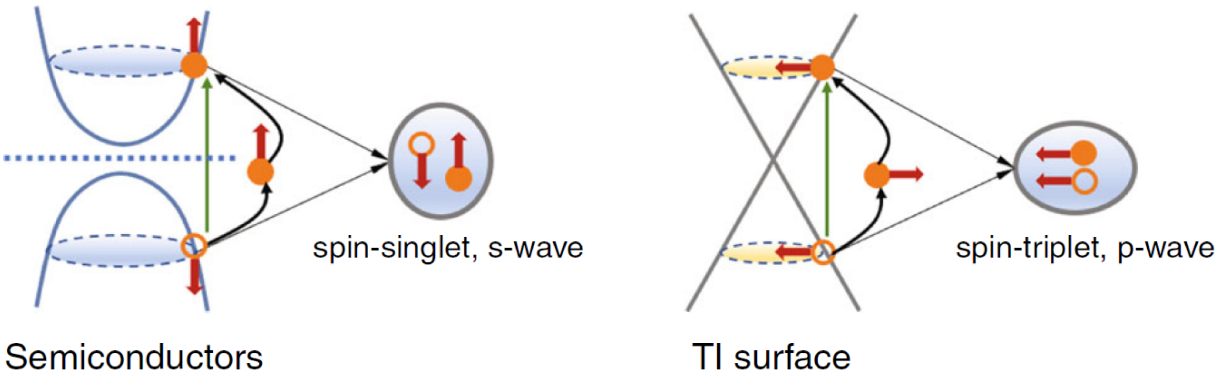

Figure 1.10: Left: topologically trivial exciton formation is dominated by s-wave spin singlet states. Right: exciton formation on the Dirac cone is comprised of p-wave spin triplets due to spin momentum locking. Figure sourced from [73].

short (in the several femtosecond range [70]), whereas in 3D TIs the lifetime can range from several picoseconds [71] (Sb_2Te_3) to several microseconds [72] (Bi_2Se_2Te).

Exciton condensates on the Dirac cone are special! In addition to their theoretically large critical temperature, the spin-momentum locking of the Dirac cone also has interesting consequences for the spin information of these excitons. In a topologically trivial semiconductor, optical excitations will be formed with carriers that have the same wavevector **k** but opposite spins–forming spin singlet states (fig 1.10). A topological insulator will form excitons that have aligned spins, which can induce a spontaneous net in-plane magnetization on the surface of the TI [73]. This can be observed through helicity-dependent measurements [74] or optical switching [75], but may be difficult to directly observe in bismuth selenide without sub-bandgap excitation sources [76]. Very recently, spin-polarized and long-lived excitons have been reported in Bi_2Te_3 by time-resolved angle-resolved photoemission spectroscopy (ARPES) [77].

Chapter 2

Ultrafast Photocurrent Measurements on Intrinsic Bismuth Selenide

The advent of ultrafast laser technology (lasers with pulse widths of $\approx$ 1ps or less) has enabled a new class of optical measurements with extreme temporal fidelity: ultrafast laser spectroscopy. Time resolution has become an optical experimental knob that enjoys the same level of importance as wavelength (energy), temperature, and chemical potential. Ultrafast optical methods have warped the landscape of condensed matter physics for several decades (even being recognized for two Nobel prizes in the span of 5 years![78–80]), and the depth and breadth of the scope of these experiments is far beyond the trivial concern of a single dissertation. In this chapter, we will discuss ultrafast spectroscopy as it applies to physics in intrinsic bismuth selenide: after a brief discussion of Ti:sapphire lasers, we will discuss our collaborator's work on transient reflectance measurements, and then launch into an extended discussion of how ultrafast lasers have impacted our photocurrent studies.

2.1 Introduction to Ultrafast Measurements

The platform for ultrafast optical experiments in this dissertation is the titanium sapphire laser (ti:sapph), which was originally investigated and developed in the 80s by

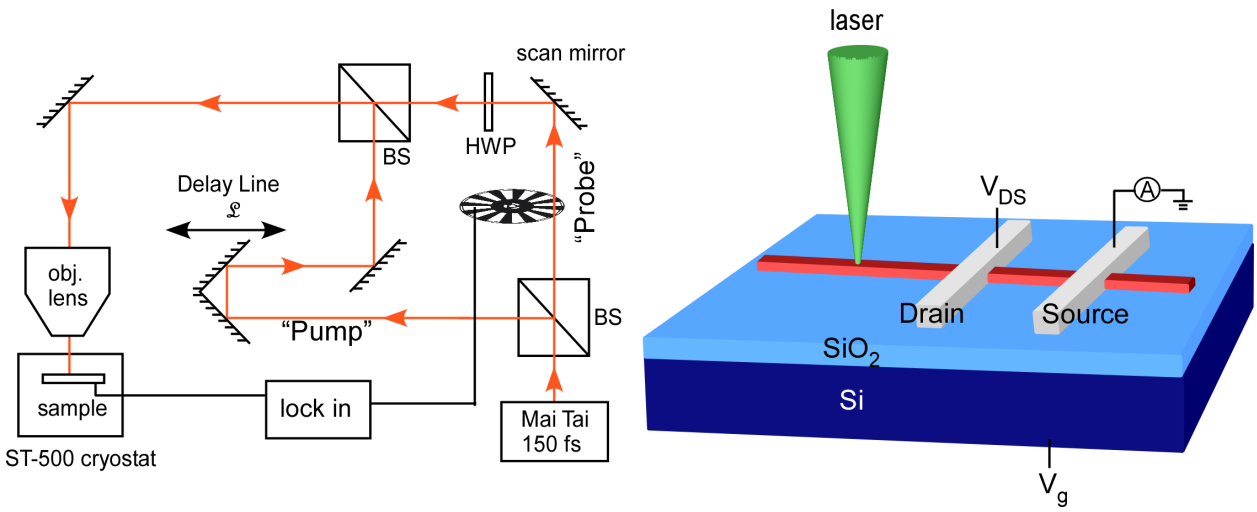

Figure 2.1: Left: Diagram of ultrafast photocurrent measurement setup, which is an example of an ultrafast optical experiment. Here, the probe signal refers exclusively to the chopped beam path. Chopping can be accomplished with an optical chopper, or a photoelastic modulator[81,82]. Beamline recombination via beamsplitter can be accomplished before the scan mirror (to perform SPCM concurrently) or after the scan mirror (to study the effects of spatially separating pump and probe). The signal is measured directly as a photovoltage with a lock-in amplifier. Right: Schematic diagram of the device with pump and probe laser pulses on the device.

Peter Moulton[83]. These systems generically consist of a Ti^{3+} doped sapphire crystal that is pumped by a green laser ($\lambda \approx 532$nm). The ti:sapph crystal serves as the laser's gain medium, which has a bandwidth of $\approx$ 130THz, which gives it a tuning range of roughly $300nm$. The pulses are created through mode-locking: the geometry of the crystal is chosen so that the pump laser will constructively interfere with itself to produce a wavepacket.

Figure 2.1 shows a simple schematic of how a ti:sapph laser can be used in a real UTP measurement. The first beamsplitter (BS) splits the pulses into two optical paths (a "pump" and a "probe", with the probe producing a measured signal). The keystone element is the delay line, which is a mechanical stage with a retroreflector that can modulate the path length of the beamline, $\mathcal{L}$. This path length can be tuned so that the pulse recombination can happen with a variable time difference (time delay, δt) at the second beamsplitter. Data is usually interpreted with the point where $\delta t = 0$ is labeled as the temporal reference, t_0.

2.1.0.1 Optical Autocorrelation

The pulses will recombine as oscillating fields with different phases:

$$\mathbf{E}_1(\mathbf{r}_1, t) = \mathbf{A}(t) \exp\left(\omega t - \mathbf{k} \cdot \mathbf{r}_1\right) \tag{2.1}$$

$$\mathbf{E}_2(\mathbf{r}_2, t) = \mathbf{A}(\mathbf{t} - \delta\mathbf{t})(t) \exp\left(\omega(t - \delta t) - \mathbf{k} \cdot \mathbf{r}_2\right) \tag{2.2}$$

where $\mathbf{A}(t)$ is the envelope of the pulse, and we specify separate position vectors due to the finite spot size of the laser. The intensity-intensity correlation of these two fields is given by the second degree of coherence, often known as $g^{(2)}$, which in its most general form is written as[84]:

$$g^{(2)}(\mathbf{r}, t_1; \mathbf{r}_2, t_2) = \frac{\langle E^*(\mathbf{r}_1, t_1) E^*(\mathbf{r}_2, t_2) E(\mathbf{r}_1, t_1) E(\mathbf{r}_2, t_2) \rangle}{\left\langle |E(\mathbf{r}_1, t_1)|^2 \right\rangle \left\langle |E(\mathbf{r}_2, t_2)|^2 \right\rangle}. \tag{2.3}$$

For plane waves at the same location, this expression can be written in terms of intensities of the two fields:

$$g^{(2)}(\delta t) = \frac{\langle I(t) I(t + \delta t) \rangle}{\langle I(t) \rangle^2}, \tag{2.4}$$

which has the very important property of being a symmetric quantity: $g^{(2)}(\delta t) = g^{(2)}(-\delta t)$. This means that the change in the probe photoresponse should be the same regardless of whether the pump is absorbed before or after the probe. In more simple terms, the labels of pump and probe are special and are only defined by what beamline is chopped. The optical autocorrelation has been used for confirming the anti-bunching statistics in single photon emitters[85].

2.1.0.2 Photocurrent Autocorrelation

The photocurrent autocorrelation, or time-resolved photocurrent (TRPC), is complementary to all-optical pump-probe techniques including transient absorption (TA), transient reflection (TR), and time-resolved photoluminescence (TRPL). TRPC senses both optical

and electronic characteristics of materials, as the conversion from light to electricity involves multiple physical processes, such as generation, transport, recombination, and collection of photogenerated charge carriers. Furthermore, to gain sufficient signal, TA and TR approaches often require that the device size must be larger than the laser spot size, while TRPC is not limited by these constraints. Recently, TRPC has gained popularity in investigating nanoscale and low dimensional materials [86,87].

The photocurrent autocorrelation method has similarities, but also significant differences from the aforementioned optical autocorrelation. In photocurrent autocorrelation measurements, the steady-state photocurrent is measured under excitation by two time-separated optical pulses with a controlled delay time. The two pulses are usually cross-polarized to avoid the optical interference. When the photocurrent is nonlinear with the fluence, the measured photocurrent depends on the pulse separation time δt. The signal can be thought of as the probe-induced photocurrent, modified by the pump-generated carriers. If the pump-created carriers persist when the probe arrives, a lower photocurrent will be generated because of the nonlinear photoresponse at higher fluence. Therefore, a dip in the photocurrent signal is expected with a characteristic time representing the carrier relaxation. The carrier relaxation process is complicated, involving multiple steps such electron-electron and electron-lattice interactions. We will first describe a two-temperature model describing hot carrier relaxation below.

2.1.0.3 Hot Carrier Thermalization and Recovery Time

The concept of a hot carrier–optically excited electrons and holes with excess kinetic energy moving at high velocities shortly after excitation[88]– can be modeled through the lens of the two-temperature model, which is a phenomenological model of the ultrafast optical

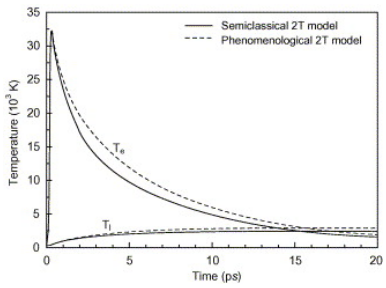

Figure 2.2: Simulation of two temperature model displaying convolution of two time scales. Figure sourced from [91].

response that tracks electronic and phonon temperature thermalization [89]:

$$C_e\left(T\right)\frac{\partial T_e}{\partial t} = \nabla \cdot \left[k_e(T_e)\nabla T_{el}\right] + G(T_e - T_\ell) + S(z,t) \tag{2.5}$$

$$C_\ell\left(T\right)\frac{\partial T_\ell}{\partial t} = G(T_e - T_\ell), \tag{2.6}$$

where T_e and T_ℓ are the electron and phonon temperatures respectively, G is the electron-phonon coupling, C_e is electronic heat capacity, k_e is electronic heat conductivity, S is a source term that represents heat generation from the laser. Values for G can be estimated via [90]:

$$G = \frac{\pi^2 m_0 n_e c^2}{6\tau_e T_e}. \tag{2.7}$$

Here, c^2 is the square of the speed of sound of the material given by the ratio of the bulk modulus and density. The two temperature model can be easily simulated with canned software like MATLAB or COMSOL, which makes it well suited to building an intuition regarding ultrafast time dynamics. The main qualitative feature here lies within the thermalization times of these two temperatures. This leads to three timescales: a very fast electron-electron thermalization process, a medium duration electron-phonon thermalization process, and a generally slow phonon-phonon thermalization process. If these three times are well separated in magnitude, then they can all be fit very reasonably!

The electronic heat capacity of a free electron gas for a parabolic band structure (the bulk states of Bi_2Se_3 are trivial semiconducting states and dominate optical transitions due

to their narrow band gap) is given by[92]

$$C_{el} = \gamma T = \frac{1}{3\hbar^2}\pi {k_B}^2 \left(3/\pi\right)^{1/3} m_0 \frac{A}{\rho}\frac{m^*}{m_0} n^{1/3} T, \tag{2.8}$$

where m_0 is the free electron mass, $m*$ is the effective electron mass, ρ is the mass density, and A the atomic weight. We can estimate the amount of photo-injected carriers by[93]

$$\Delta n = \frac{\mathcal{F}}{hf\delta}, \tag{2.9}$$

where $\mathcal{F}$ is the beam fluence and δ is the penetration depth of the beam. Intrinsic (properly antimony-doped) bismuth selenide samples will generally have a carrier concentration in the ballpark of $n \approx 10^{17}\mathrm{cm}^{-3}$ at low temperatures: this means that beam fluences above $\approx 1\mu\mathrm{J\,cm}^{-2}$ will excite a number of carriers similar to the dark carrier concentration and that it is reasonable to model our observations with hot phonon effects. As an example, plugging in a fluence of $\mathcal{F} = 200\mu\mathrm{J\,cm}^{-2}$ gives a change in the carrier concentration of $\Delta n = 8 \times 10^{19}\mathrm{cm}^{-3}$. If we use $m^* = 0.1m_0$, $A = 654.8\mathrm{g\,mol}^{-1}$, and $\rho = 6.82\mathrm{g\,cm}^{-3}$, then the free electron model predicts that the temperature of the hot electrons will reach a temperature greater than $T = 7500\mathrm{K}$, which is comparable to the temperature of the sun. This initial temperature relaxes to $\approx 400\mathrm{K}$ in the span of several picoseconds[94].

2.1.0.4 Energy Transfer and Recovery Time

Energy transfer through Peltier cooling can be important at metal-material interfaces[95]. The large difference in Seebeck coefficients at the junction will provide a cooling effect and can therefore influence the signal recovery time. The Peltier cooling is local to the junction (e.g. restricted to–at most–the edge of the depletion region), unlike optical phonons that cool the entire laser spot size.

2.2 Previous Ultrafast Transient Reflectance Results in Intrinsic Bismuth Selenide

Ultrafast transient reflectance (UTR) measurements are a popular tool used to probe carrier dynamics in materials. As a purely optical measurement, they are especially flexible as they do not require complex cleanroom processing to produce measurable devices (this simplifies sample preparation, and also reduces the fixed costs to run the experiment). UTR is usually interpreted through the lens of time-dependent changes in a sample's complex dielectric function[96]:

$$\frac{\Delta R}{R}(t) = \frac{\partial \ln R}{\partial \epsilon_1}\Delta\epsilon_1(t) + \frac{\partial \ln R}{\partial \epsilon_2}\Delta\epsilon_2(t), \tag{2.10}$$

which relates the change in the reflectance of the material to changes in the real (ϵ_1) and imaginary (ϵ_2) parts of the complex dielectric function. This is generally a very brief (several ps to perhaps a ns) small change (on the order of one part per thousand or smaller)!

Previous work by Gross et al.[43] performed fluence-dependent UTR measurements on intrinsic bismuth selenide grown by the Yu group showed that the measured lifetime tended to decrease when pump fluence was increased.

In the zero pump fluence limit, the lifetime was found to be $\tau = 2$ns, which is significantly larger than previously reported values. The lifetime suppression at higher fluences is attributed to bimolecular recombination–at higher intensities higher-order recombination mechanisms become relevant, which will generically shorten excitation lifetimes.

Many other interesting transient reflectance measurements have been done. Whilst Gross et al. found that large fluences tend to throttle the excitation lifetime, this is not always the case. Glinka et al.[97] found that in 20nm films (corresponding to 20 quintuple layers (QL), as one QL is very nearly 1nm), sufficiently large fluences can actually *increase* the excitation-lifetime, which they attribute to a carrier depletion-induced suppression of phonon modes.

2.3 Ultrafast Transient Photocurrent Measurements

Ultrafast transient photocurrent measurements produce results that are qualitatively different from transient reflectance measurements. Whereas the beauty of UTR is that it solely probes the change in reflectance of a material through changes in its dielectric function, UTP will produce a signal that reflects several experimental responses simultaneously. Photocurrent generation is a function of absorption $\mathcal{A}$, so we can expect to have some sort of UTR signal buried in our measurement. In the absence of transmission, the change in absorption has a very simple relationship to the change in reflection:

$$\Delta\mathcal{A}(t) = 1 - \Delta R(t), \tag{2.11}$$

again stressing that reflectance changes are very small quantities.As we will see, this makes contributions from UTR to a UTP signal functionally impossible to measure. Another major contributor to an UTP measurement is through the transport of photocarriers from the injection location to the measurement electrode. The decrease in photocurrent magnitude, $\Delta\mathcal{T}$ through spontaneous recombination of carriers during transport in time is spatially encoded by the carrier diffusion length:

$$\Delta\mathcal{T}(x) = A\exp\left(-\frac{x}{L_D}\right). \tag{2.12}$$

Note that a priori, we expect that the absorption modulation should be local and only depend on time, while transport should be time-independent. Lastly, the injected carriers can also modify the band bending of source-drain electrodes. This is all to say that UTP measurements can be difficult to fully untangle.

Our experimental setup (fig. 2.1) is similar to our DC photocurrent setup, but additionally consists of an ultrafast laser (Spectra Physics Mai Tai HP), a delay line (NewportDL 325), and a lock-in amplifier.

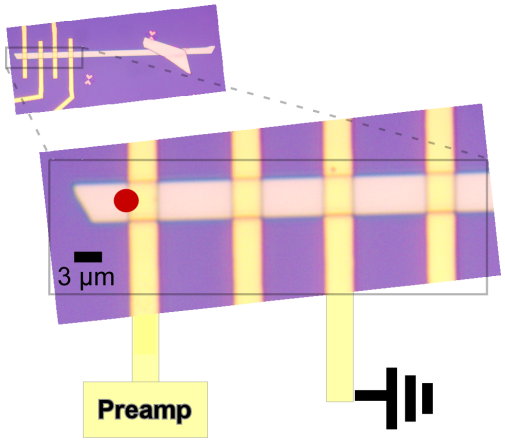

Figure 2.3: Room temperature measurement schematic for UTP. The laser is focused on the depletion region. One electrode is grounded, with a lock-in amplifier measuring voltage on another electrode. All other electrodes are floating. The spot size is 3μm.

2.3.1 Room Temperature Dependence

Temperature-dependent measurements are very important in ultrafast measurements of any kind. Practically, an experimenter can adjust a cryostat temperature via some combination of cryogens, a heating source, and a PID temperature controller. The cryostat temperature is identical to the lattice temperature in thermal equilibrium, which can strongly affect UTR and ultrafast transient photocurrent (UTP) measurements. As an example, experimenters have used temperature-independence to argue that their UTP measurements were hot carrier dominated [95]–the logic being that electron temperature is large compared to the lattice temperature at every experimentally accessible temperature. Our measurements demonstrate qualitatively different results at room temperature and at cryogenic temperatures, which respects the general trends of our steady-state photocurrent measurements intrinsic bismuth selenide.

2.3.1.1 Ultrafast Time-Resolved Photovoltage Results at 300K.

The photoresponse of intrinsic bismuth selenide is very local at room temperature, meaning that photovoltage is only non-zero when the laser is focused very close to the metal contact of the device (fig 2.3). This is because the laser-injected charge carriers can only diffuse in a short distance at room temperature before carrier recombination. The photocurrent is created when the photogenerated electrons and holes get separated under the strong

electric field in the depletion region, which is generally tens of nanometers wide[98]. The spot size is near the diffraction limit for our optics, which is nearly 3μm. Broadly speaking, our room temperature UTP results display a nearly symmetric photocurrent suppression near $\delta t = t_0$. At $\delta t = t_0$, this effect is maximized. For $\delta t > t_0$ the excited pump carriers will recombine and relax to the valence band with some characteristic relaxation time, which eventually causes the photovoltage to recover to some baseline value. For $\delta t < t_0$, the probe pulse is absorbed before the pump pulse. The signal is nearly symmetric, which is reasonable because the autocorrelation function that governs the intensity ($g^{(2)}$) is symmetric. We fit each branch of the response from t_0 with a simple exponential fitting:

$$V(\delta t) = V_0 + \Delta V \exp\left(-\frac{||\delta t||}{\tau}\right), \tag{2.13}$$

which allows us to extract the photovoltage at large time delay, V_0; the change in photovoltage, ΔV; and the characteristic time that it takes the photovoltage to recover, τ. There are two important features: first, increasing the pump fluence will increase the magnitude of the photovoltage suppression, with diminishing returns (fig. 2.4). The second feature is that even though the magnitude of the signal changes, the recovery time has no sensible fluence dependence (fig. 2.5). The recovery time τ was found from fitting to be about 20 to 30 ps (Fig. 2.5) A significant source of error in this measurement comes from beam shift– because a very small region of the device is photoactive (the depletion region), even small shifts in beam position (on the order of hundreds of nanometers) can dramatically change the effective intensity for each scan.

The room temperature results are likely dominated by photo-thermoeletric (PTE) effects, where the local laser heating creates a temperature gradient in the device which drives a current flow. The relatively weak photovoltage signal at room temperature is consistent with the estimation using the temperature increase and the Seebeck coefficient of the material. The photovoltage sign is also consistent with the n-type doping of our samples. In addi-

tion, we observed that the photovoltage became much stronger at low temperatures which indicated photovoltaic origin. The sign of the photovoltage at room temperature was also opposite to those at low temperatures, indicating the photovoltage generation was dominated by a different mechanism, likely PTE. The ultrafast photovoltage results are consistent with our previous room temperature steady-state photocurrent measurements[52]. The relatively uniform recovery time suggests that we are probing hot carriers at room temperature[95], but the recovery time is longer than previously reported hot carrier lifetimes[94].

The magnitude of the photovoltage suppression increases from 15% to 50% as the pump fluence increases (fig. 2.4). This suppression is much larger than that expected from the optical absorption change and indicates the mechanism of the suppression is not caused by absorption saturation. A similar suppression magnitude has been found in Cd3As2 nanowire devices (manuscript in preperation), which may also attributed to PTE.

The curves are well-fit by a single exponential, which suggests that the relaxation process is due to a single dominant mechanism; up to three exponentials can be fit to pump-probe experiments that have distinguishable timescales between electron-electron, electron-lattice, and lattice-lattice relaxation[99]. The fittings as a function of fluence (fig. 2.5) display two salient features: a slight asymmetry between fittings to the left and to the right of t_0 (corresponding to probe-before-pump and probe-after-pump absorption respectively), and a near constant fitting value across all fluences: the probe-before-pump side has a recovery time of $\tau = 21$ps and the probe-after-pump side has a recovery time of $\tau = 27$ps. The magnitude of the photovoltage suppression does increase with pump fluence, but slows down at higher fluences without appearing to saturate.

2.3.1.2 Ultrafast Time-Resolved Photovoltage at 79K.

We performed the same experiment (laser spot focused on close the contact and out-of-channel) at 79K. This produced a much larger photovoltage (roughly 2 decades larger in magnitude) for $||\delta t|| > t_0$, with a swapped polarity (from negative on the lock-in at 300K,

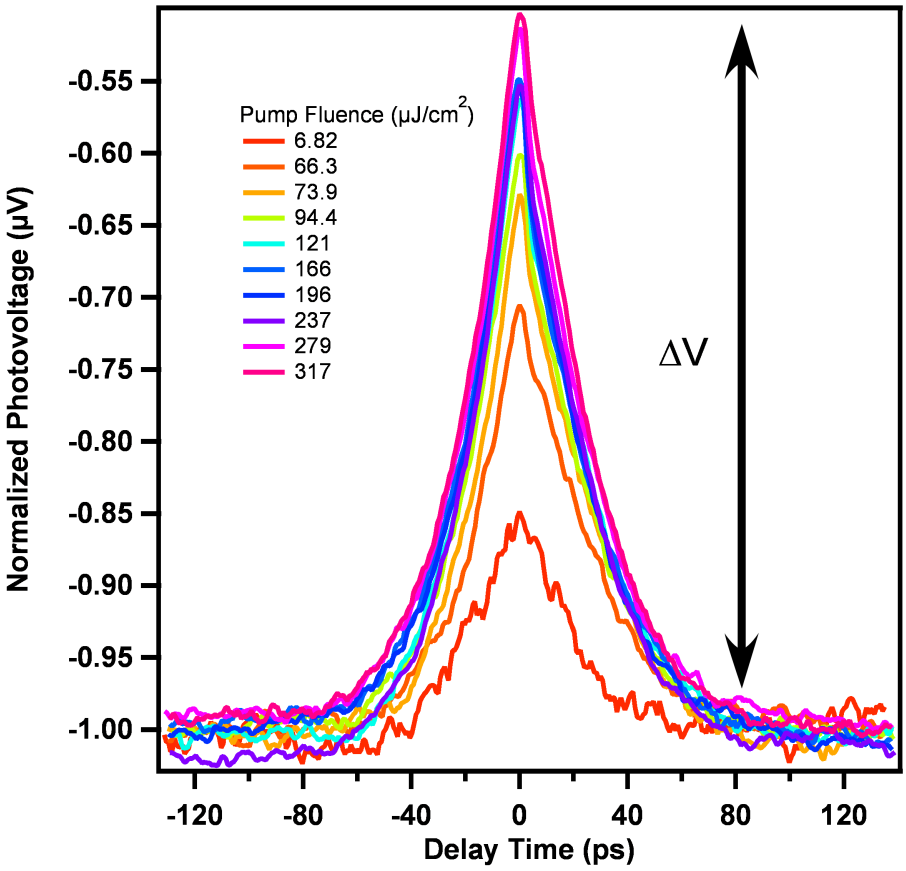

Figure 2.4: Room temperature photovoltage measurements. Each trace is normalized by the maximum photovoltage value. The probe fluence is $5\mu\text{J} \cdot \text{cm}^{-2}$.

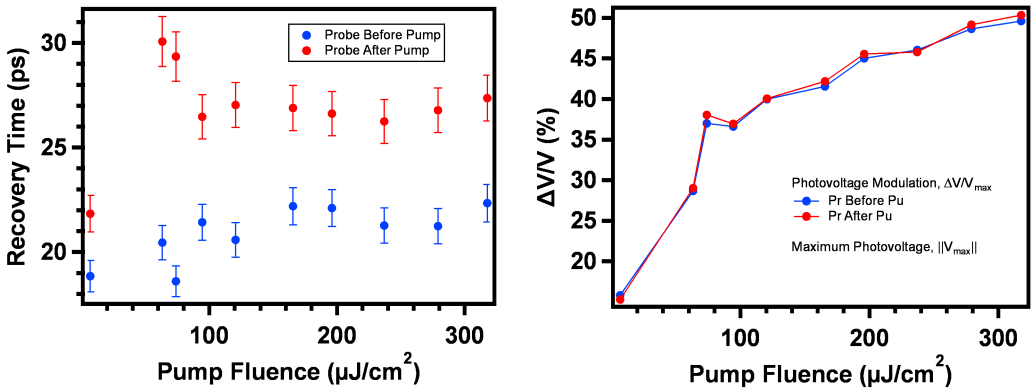

Figure 2.5: Extracted V, ΔV, and τ for the room-temperature fluence-dependent results. Error bars from fitting the recovery time fittings are calculated as a standard deviation from the fit coefficient values, and are barely larger than the circles that represent them. The probe after pump point for the $6.82\mu\text{J}/\text{cm}^2$ is anomalous and not reproducible (cryostat drift is one such explanation for this large difference).

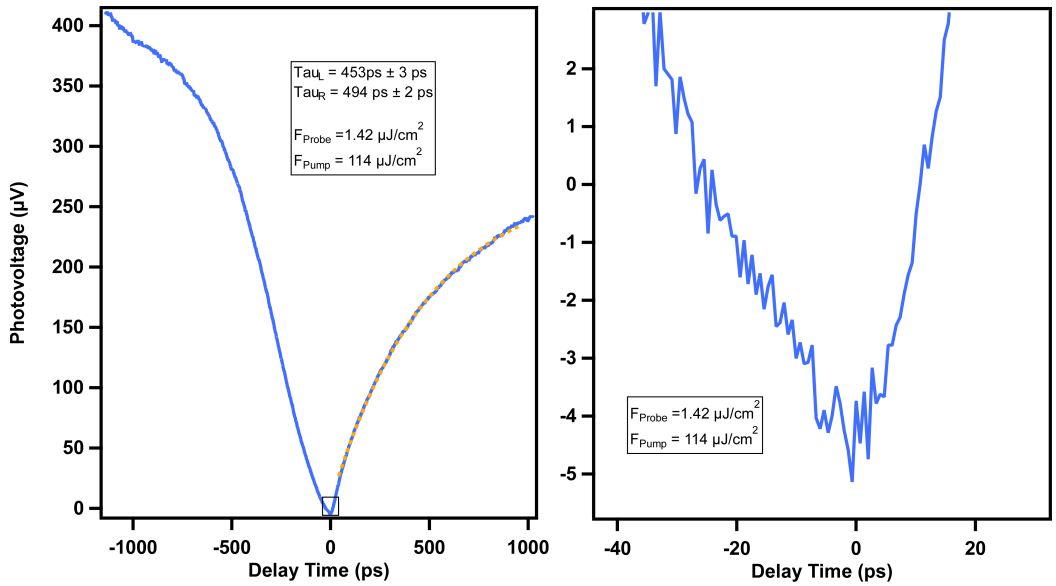

Figure 2.6: UTP measurements with the laser focused on the contact at 78K. Left: full delay time spectrum, showing enormous range of suppression, as well as asymmetry on either side of t_0. Right: Inset of region around t_0, showing that photovoltage flips sign.

to positive on the lock-in at 79K). This is consistent with the dramatically more efficient transport that we generally expect at cryogenic temperatures. In addition to the larger photovoltage reading, we also see a pronounced asymmetry of recovery time, as well as a flipping of photovoltage signal when $||\delta t|| \approx t_0$. The photovoltage flipping has a simple interpretation that can be agnostic about the specific mechanism that causes the photovoltage suppression: while the room temperature photoresponse is dominated by the photothermal effect, it is still present at any temperature. If the photovoltaic response can be suppressed, then we should see the photothermal effect! The negative photovoltage for $||\delta t|| \approx t_0$ is two decades smaller and the opposite sign, which are the signature characteristics of the room temperature (i.e. photothermal-dominated) response. Observing the crossover from photovoltaic to photothermal-dominated signals does require a high fluence on the order of $100\mu\text{Jcm}^{-2}$. The asymmetry of the probe-before-pump and probe-after-pump fittings is more puzzling, but we can get more clues about this feature (including if it is plausibly real, or an optical artifact) by a full temperature-dependent set of data.

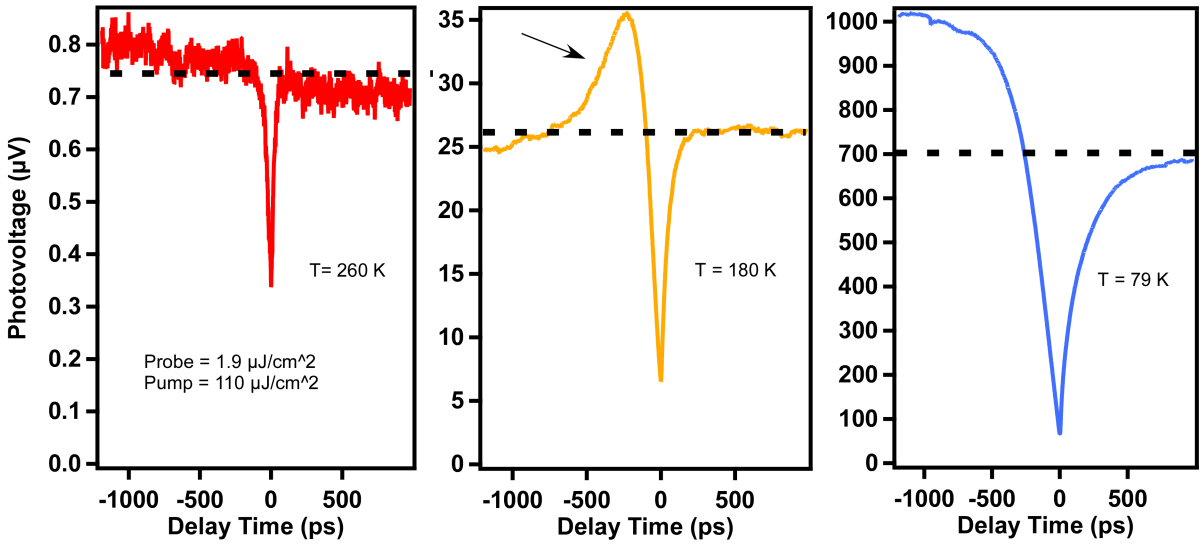

Figure 2.8: Sampled temperatures for temperature-dependent photovoltaic-dominated measurement. The dashed line indicates the baseline photovoltage, which is the probe induced photovoltage with a blocked pump. As the sample cools, the photovoltage becomes large, and an enhancement in the probe before pump side (negative delay time) emerges.

2.3.1.3 Temperature Dependence of the Photovoltaic signal

Moving the laser out of the depletion region (to avoid contributions from the photothermal effect) and into the middle out-of-channel region (fig. 2.7) allows us to study the photovoltaic signal on its own terms. This restricts us to a range of temperatures because the photoresponse will become highly localized (and therefore unresponsive) near room temperature. The photovoltaic UTP signal is clearly temperature dependent. Intervening temperatures between 79K and 300K show that the probe-before-pump asymmetry is an emergent enhancement feature (fig. 2.8). A full spectrum of temperatures (fig. 2.9) shows the photovoltage decrease over three decades as the cryostat is tuned from $T = 260$K to $T = 79$K! The enhancement peak grows as temperature decreases, and it quickly becomes clear that the effects of the pump persist beyond the temporal resolution of our delay stage.

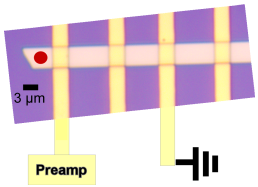

Figure 2.7: Photovoltaic measurement configuration

Fitting the full spectrum of temperature-dependent data from 300K to 78K shows that the recovery time increases at lower temperatures, and that the magnitude of the photo-

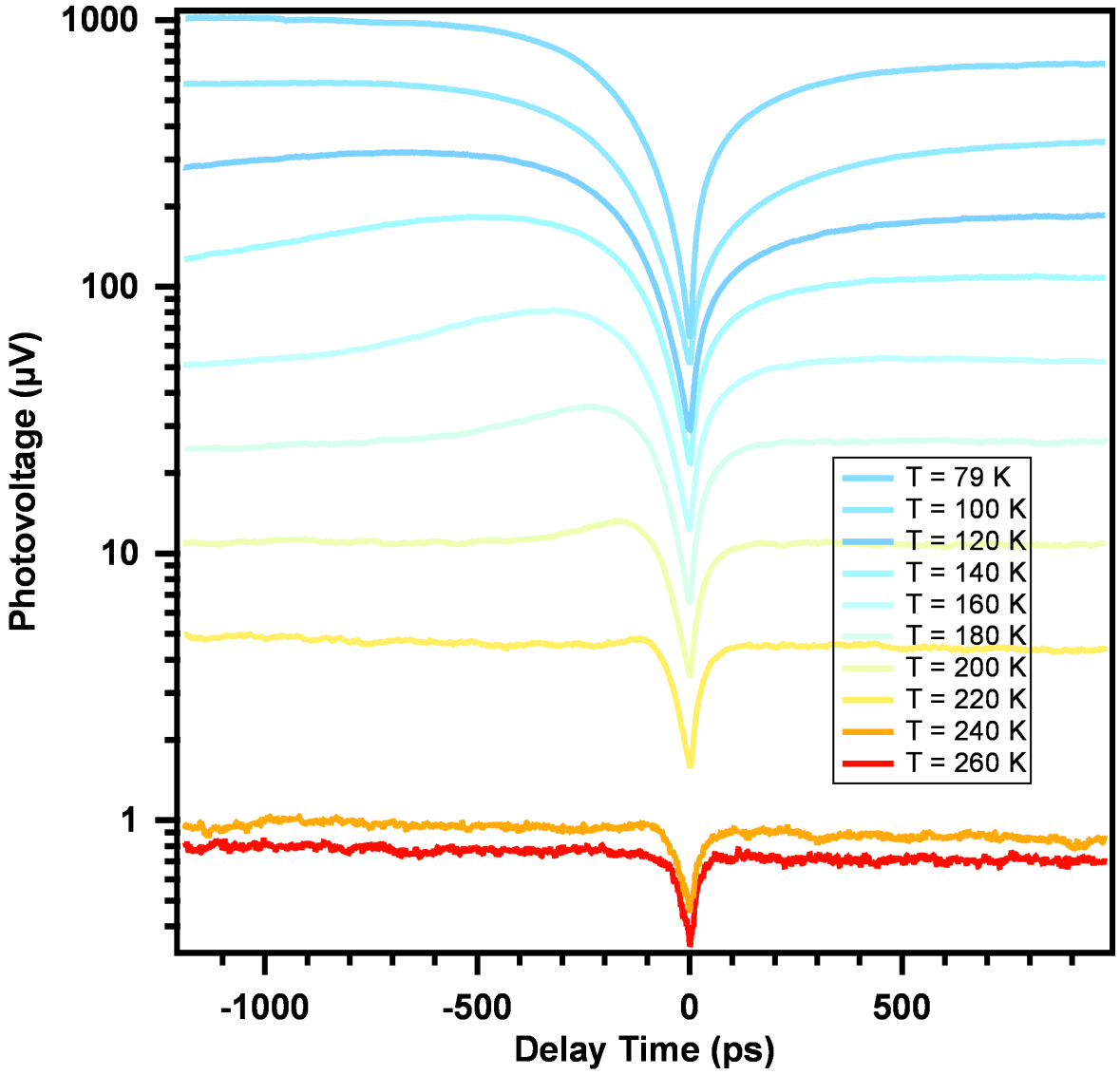

Figure 2.9: Full spectrum of temperatures that figure 2.8 is sourced from. The probe fluence is $\mathcal{F} = 1.8\mu\mathrm{J\,cm^{-2}}$, the pump fluence is $\mathcal{F} = 110\mu\mathrm{J\,cm^{-2}}$ and laser location is same as figure 2.7

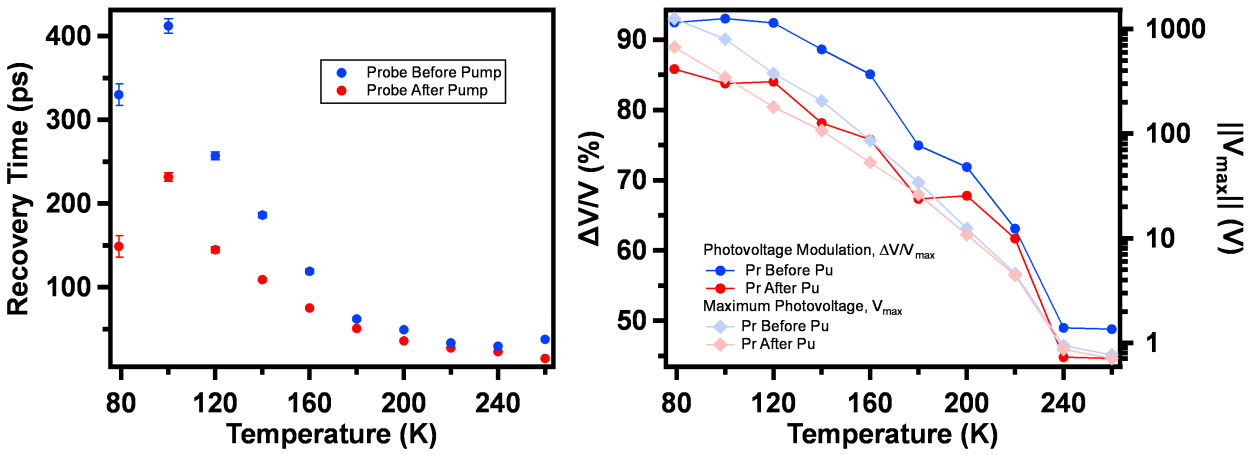

Figure 2.10: Fittings from temperature-dependent UTP measurements, derived from the data contained in figure 2.9.

voltage suppression ($\Delta V/V$) increases monotonically. The temperature-dependent recovery time is a function of both carrier recombination time τ_R, and carrier escape time τ_E such that the overall recovery time can be stated through Matthiessen's Rule:

$$\frac{1}{\tau} = \frac{1}{\tau_R} + \frac{1}{\tau_E}. \tag{2.14}$$

Recombination times are likely to be longer at cryogenic temperatures from freezing out phonon interactions, which is supported by previous ultrafast spectroscopy experiments on bismuth selenide[94]. How exactly the characteristic escape time, τ_E, depends on temperature is unclear. The escape time can be estimated from $\tau_E = l^2/D$ where l is the distance and D is the diffusion coefficient. The carriers directly generated within the absorption depth about 30 nm near the top surface can diffuse out of the illumination region either vertically downward or laterally out of the laser spot size of 3 μm. The vertical diffusion is through the bulk, while the lateral diffusion is through the surface which may have larger diffusion coefficient given the topologically protected surface states or formation of exciton condensate. Hot carriers immediately after pumping may also convolute the relaxation process. Further work is needed to clarify on the exact mechanism for understanding the relaxation time, including

both device modeling and experiments such as laser spot size and sample thickness-dependent TRPC.

The asymmetry in the photovoltage is striking. In the negative δt regime (where the probe pulse is absorbed before the pump pulse), the photovoltage increases above the baseline photovoltage (the photovoltage with pump completely blocked). Figure 2.8 shows this enhancement as an emergent feature that depends strongly on temperature. In the positive δt regime (where the probe pulse is absorbed after the pump pulse), there is no enhancement for all temperatures and the photovoltage always recovers towards the baseline photovoltage. What's happening here? Given the repetition rate of the Mai Tai (80MHz, which corresponds to a 12.5ns delay between pulse trains), one can view the negative δt regime as an addition time delay of several nanoseconds. Trap filling has been shown to generically enhance photovoltage[100–102], and filled traps can also act as a local gate that can modify the chemical potential[103,104] to an energy that is more favorable for exciton transport[105]. Trap filling can be both temperature dependent[106] and very slow (tens of nanoseconds)[107], suggesting that our observed photoenhancement can come from optical manipulation of trap states.

2.3.2 Gate Dependence

As initially mentioned, UTP measurements can be difficult to fully interpret because they involve a convolution of absorption, transport, and charge separation behaviors. However, the addition of source-drain electrodes does allow us to perform gate-dependent experiments. One of the primary benefits of the platform is the ability to tune the chemical potential via an applied gate voltage. Importantly for our experiment, our as-fabricated s are only capable of applying a global gating effect through the use of a solid back gate. Other configurations for UTP studies have exploited local top gate configurations to achieve efficient charge separation[95]; we can simply rely on efficient transport from the injection site

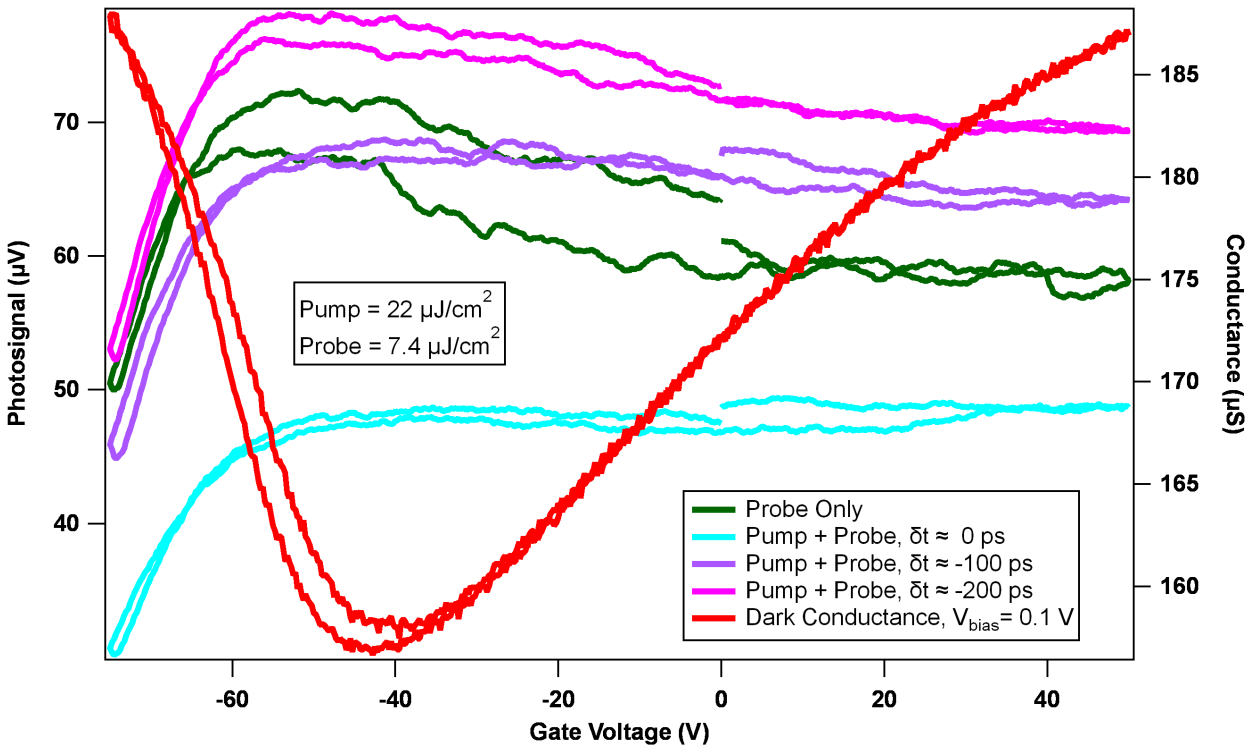

Figure 2.11: Open circuit gate dependent measurements at different time delay values. The pulsed laser suppresses the gate hysteresis. The dark conductance scan (red) shows that the charge neutrality point is near $V_G = -40$V.

to the electrodes, where the band bending between the electrode and the crystal is enough to separate excitons and produce a measurable signal.

Our DC measurements showed strongly gate-dependent behavior[52]: first, the peak photocurrent increases as the chemical potential approaches the charge neutrality point while the diffusion length remains constant; second, the peak photocurrent *and* the diffusion length are greatly suppressed as the chemical potential is tuned beyond the charge neutrality point to near the valence band.

2.3.2.1 Short Circuit Photocurrent Measurements

Short-circuit gate-dependent measurements (e.g. zero bias, fixed laser position out of channel but away from the depletion region, with varying gate) at different delay times show four interesting features (fig. 2.11):

First, that there is photocurrent enhancement in this device when the pump is added to beamline–the peak photovoltage increases between the pumpless and pumped photovoltage. This photovoltage enhancement is consistent with the emergent enhancement shoulder that is present in the temperature-dependent data. The origin of this feature is attributed to the charge trapping as discussed.

The second feature regards the solid gate efficiency: as $\delta t \longrightarrow 0$, we see that the gate modulation becomes less effective for gate values that are above the charge neutrality point. When $\delta t > t_0$, we still have some change in the photovoltage for positive gate voltages. However, when $\delta t \approx t_0$, the solid gate is almost completely incapable of modulating the photovoltage. The electron mobility estimated from the gated dependent dark conductance is

$$\mu \approx \frac{\frac{\Delta G}{\Delta V_G}}{\frac{\epsilon_0 \epsilon w}{hL}} = 61 \text{ cm}^2 \text{ V}^{-1} \text{ s}^{-1}, \tag{2.15}$$

where ϵ is the relative permittivity of the gate dielectric (silicon dioxide, $\epsilon = 3.9$), w and L are the channel width and length, and h is the gate dielectric thickness. The measured FET mobility is remarkably lower than what has been shown in our best devices, which are roughly an order of magnitude larger[52]. The change in conductance can be estimated from the linear regime of the gate scan of figure 2.11. The carrier concentration is

$$n = \frac{GL}{tWe\mu} = 8 \times 10^{18} \text{ cm}^{-3}, \tag{2.16}$$

where t is the thickness of the nanoribbon. The FET mobility changes the conductance by roughly 15%, where the pump injects carriers equal to[93]:

$$\Delta n = \frac{\mathcal{F}}{\hbar\omega\delta} = 4 \times 10^{19} \text{ cm}^{-3}, \tag{2.17}$$

where $\mathcal{F} = 22\ \mu J/cm^2$ is the fluence per area, $\hbar\omega = 1.8$ eV is the photon energy of 690 nm light and $\delta \approx 20$ nm[108] is the wavelength-dependent penetration depth. The gate voltage

cannot effectively tune the carrier concentration because the laser injects an amount of carriers that is significantly larger compared to the dark carrier concentration at $\delta t = 0$.

The third feature is that the photovoltage is rapidly suppressed as the gate voltage tunes the chemical potential below the charge neutrality point *for all values* of δt. This feature is consistent with our DC photocurrent measurements[52], where we attributed this feature due to hybridization with bulk states.

Fourth, the hysteresis present in the gate scan is reduced when $\delta t \approx t_0$. Intrinsic bismuth selenide devices are known to have trap states that can modify the electronic properties of behavior[105]. As δt approaches t_0, the enlarged local carrier concentration should fill these higher energy trap states that can cause gate hysteresis[109,110]. Even if these trap states are localized to the surface in contact with the oxide gate dielectric, as can happen with devices[111,112], these states can still be filled by the massive carrier modulation by the laser.

2.3.2.2 Gate Dependent UTP Measurements

Our gate-dependent UTP measurements were completed with a different device than discussed in the previous section. The complete spread of gate-dependent data (fig 2.12) is busy, but generally shows that the recovery time is inversely proportional to the gate voltage. When fit to a single exponential, a different story emerges. Figure 2.13 summarizes these fittings, as well as a dark gate scan that identifies the charge neutrality point at $V_G \approx -60$V. The recovery time has a clear dependence on gate voltage: it has a nearly linear inverse proportionality to gate voltage, doubling over the course of 100V. The recovery time does flatten out and begins to decrease past $V_G = -60$V, but it does not crash out like the trends with DC photocurrent studies show[52].

The maximum photovoltage shows a general decrease when the chemical potential is tuned past the charge neutrality point, but it does not decrease as rapidly as the DC

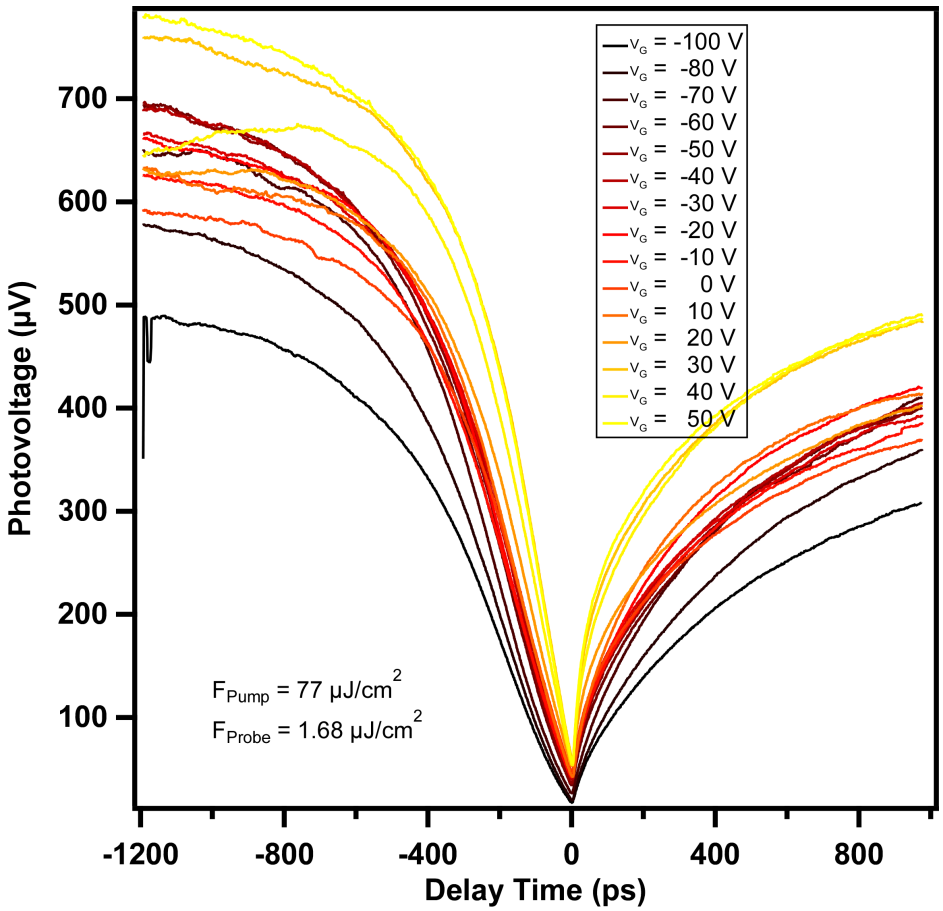

Figure 2.12: Gate dependence of photovoltage suppression. The peak photovoltage when $\delta t >> t_0$ tends to grow larger as the chemical potential is tuned *into* the conduction band, which is consistent with the steady-state SPCM results.

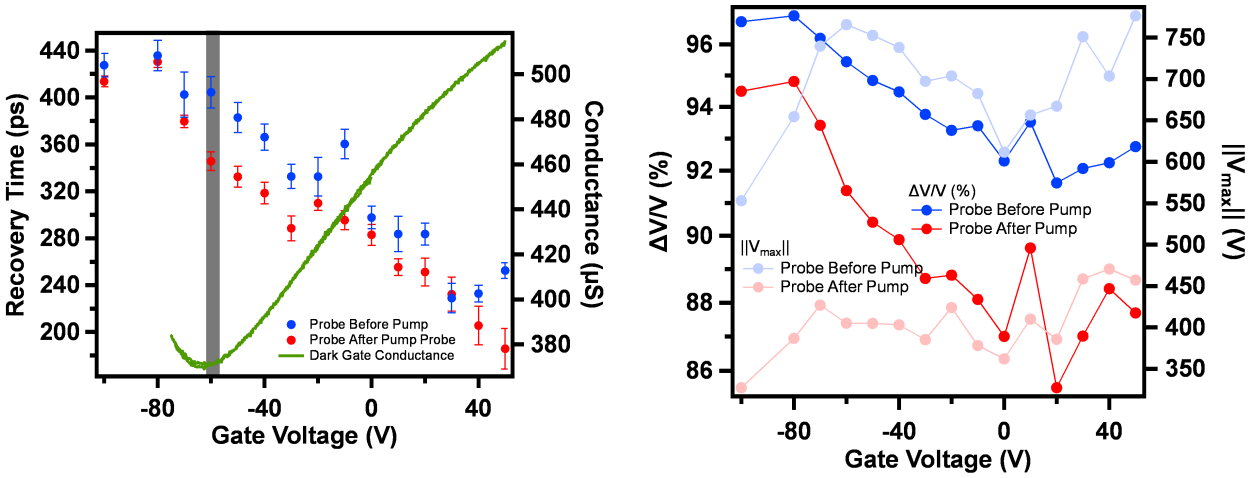

Figure 2.13: Experimental fittings of gate dependence. Left: recovery time fittings overlain with FET mobility scan.

photocurrent–the maximum photovoltage and the photovoltage suppression magnitude both share this trend.

2.3.2.3 Discussion

In our MOSFET device architecture, the gate voltage has a very well-defined role in tuning the chemical potential[113]. The gate scan in figure 2.13 show that the signal recovery time is longest when the device is more intrinsic. This picture agrees with the results of Gross et. al, which show that the signal recovery time (which, in the case of reflectance measurements, is commonly accepted to be a measurement of excitation lifetime) is largest when fluence is sufficiently low to avoid bimolecular recombination. The lower the fluence, the more intrinsic the device. This device shows

$$\mu = 250 \text{ cm}^2 \text{ V}^{-1} \text{ s}^{-1} \tag{2.18}$$

$$n_{intrinsic} = 2 \times 10^{18} \text{ cm}^{-3} \tag{2.19}$$

$$\Delta n = 1 \times 10^{20} \text{ cm}^{-3}. \tag{2.20}$$

The UTP measurement is performed with a much larger pump fluence ($77 \mu\text{J}/\text{cm}^2$, which corresponds to a carrier injection of $\Delta n \approx 10^{20} \text{cm}^{-3}$) than the open circuit measurement (and therefore the injected carrier quantity is *even larger*), and yet the gate voltage can still have a large influence on recovery time. The gate-dependent recovery time is consistent with the intuition that longer lifetimes should be observed in more intrinsic devices, but it is surprising that the gate can do anything at all considering that the pump dominates where the chemical potential lies. On the other hand, given the relatively long recovery time of hundreds of ps, the photogenerated carriers have sufficient time to recombine or escape out of the photoexcitation area. A quick estimation of carrier escaping time out of the $l = 1.5$ μm laser spot radius is $t_e = ql^2/(\mu k_B T) = 300$ ps, if using mobility of 1000 cm^2/Vs at 78 K.

In addition to changing carrier concentration, the gate voltage in MOSFET studies can affect band bending[114] or trap state filling[115]. We can discard band-bending effects due to the extremely local nature of the photovoltage suppression: this will be more thoroughly discussed in context with our ultrafast SPCM results. Trap states can be filled by changing the chemical potential, as can occur in systems with strong interfacial disorder like quantum dot superlattices[116]–we see longer recovery time as the chemical potential is tuned away from the conduction band towards charge neutral point, so this is not likely to be present in our measurement. Even though it is unlikely that we are passivating traps directly through the chemical potential, the short circuit photovoltage measurement (fig. 2.11) does show that the scan hysteresis reduces significantly.

2.3.3 Fluence Dependence

The fluence dependence of our experiment produces our most interesting and confounding results. For all fluence-dependent measurements, the probe fluence is fixed while the pump fluence is allowed to vary. Whereas Gross et al. observed a signal decay time that decreased at larger fluence[43], we observed a signal decay time that *increased* at larger fluences (fig. 2.14).

The fluence dependence of our signal contains a great deal of surprising information: First, photovoltage suppression. The suppression of measured photocurrent near t_0 is a common feature in all of our measurements. As the pump laser fluence increases, the suppression of our measured photocurrent becomes larger. The ratio between our normal signal and are signal at t_0 is very dramatic: 95%!

$\Delta V/V$ increases monotonically with fluence and saturates. Notably, the photovoltage remains positive for all values of pump fluence–even for fluences ten times larger than shown in figure 2.14.

Another important feature is the crossover from photovoltage suppression near t_0 to a pure enhancement across all values of δt. As the time delay δt flutters near t_0, the measured

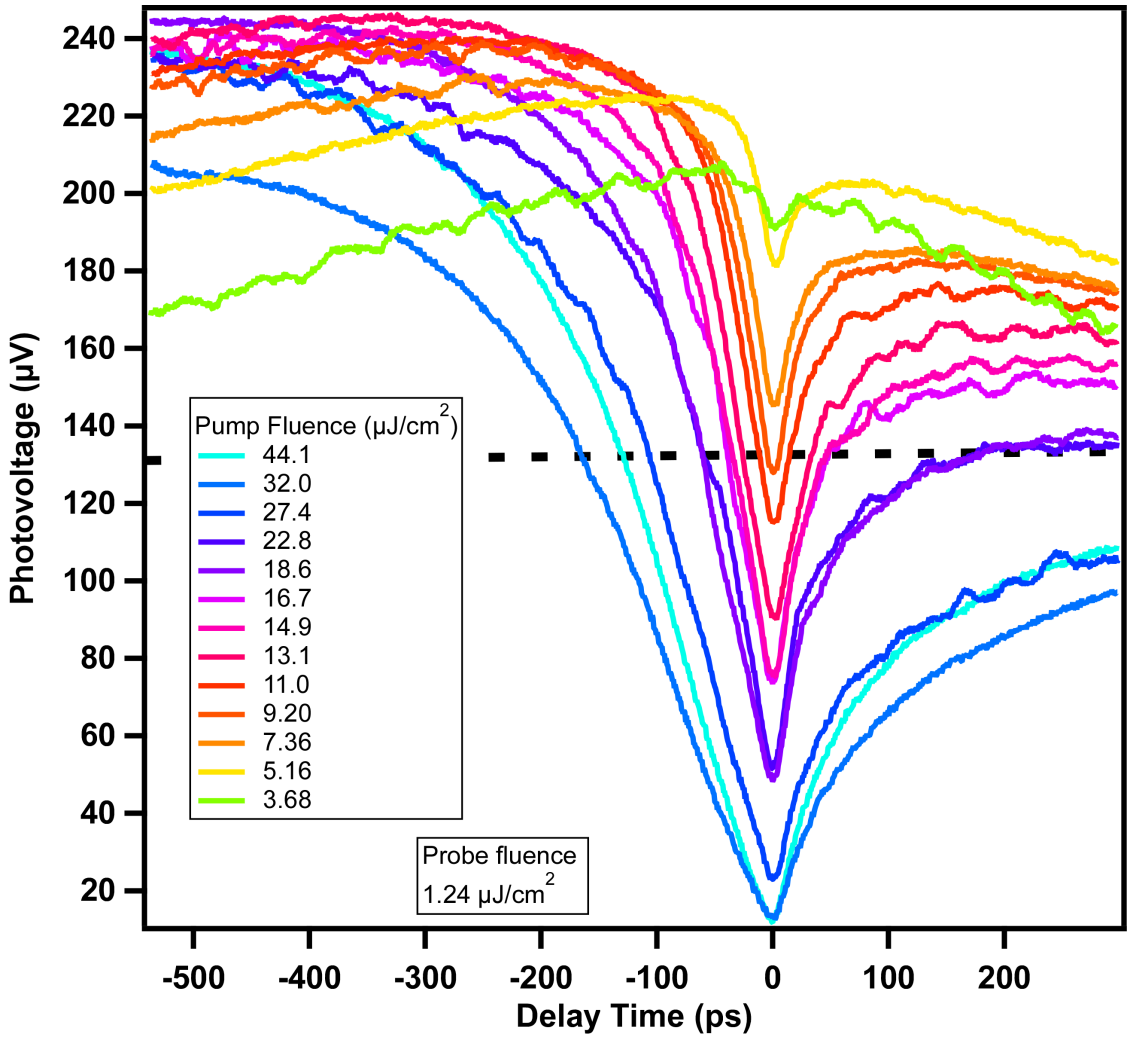

Figure 2.14: Fluence-dependent results for our ultrafast transient photocurrent measurements on intrinsic bismuth selenide. The dashed black line shows the baseline photovoltage (pump completely blocked).

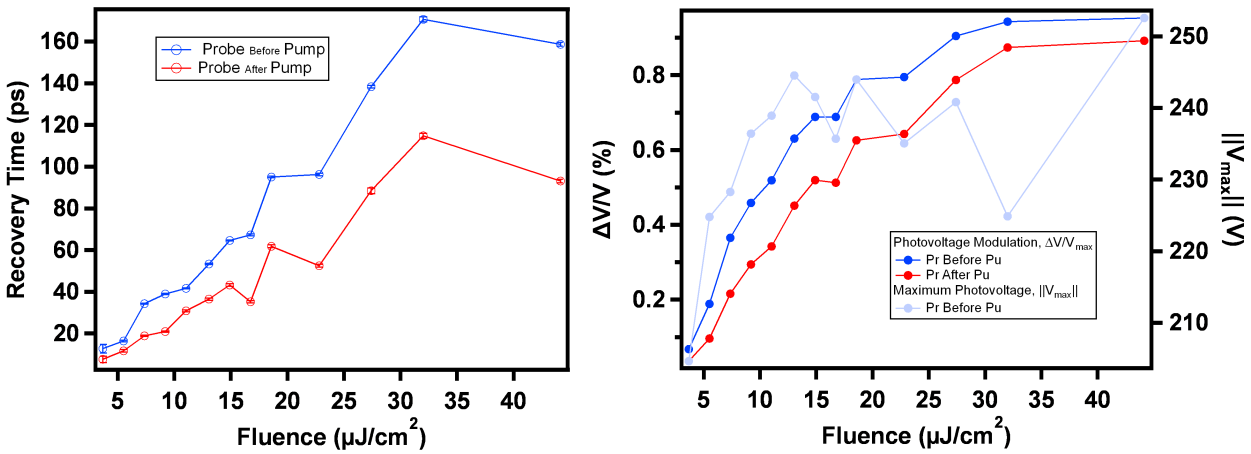

Figure 2.15: Fitting parameters from figure 2.14

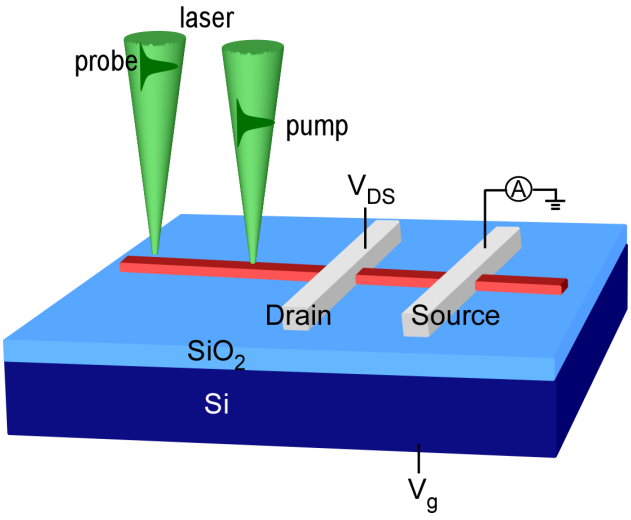

Figure 2.16: Diagram of ultrafast SPCM experiment with spatially separated pump and probe. The pump laser is focused and held stationary, while the probe laser is raster across the device.

photocurrent signal shows some indication of enhancement for certain pump fluences. We can estimate the amount of photo-injected carriers by [93]

$$\Delta n = \frac{\mathcal{F}}{\hbar\omega\delta}, \tag{2.21}$$

where $\mathcal{F}$ is the beam fluence and δ is the penetration depth of the beam. Recall that deeply intrinsic (e.g. optimally antimony-doped to minimize carrier concentration) Bi_2Se_3 samples generally have a carrier concentration in the ballpark of $n \approx 10^{17}\text{cm}^{-3}$: this means that pump fluences above $\approx 1\mu\text{J}\,\text{cm}^{-2}$ will excite a number of carriers similar to the device carrier concentration.

2.4 Ultrafast SPCM and Transit time

Ultrafast measurements can be generalized beyond single-spot reflectance and photocurrent studies. Measurements with spatially separated probe and pump have enabled experimentalists to directly image carrier transport [117,118] and charge recombination [119,120]. We can also expand our expertise with to create spatial maps of our UTP measurements.

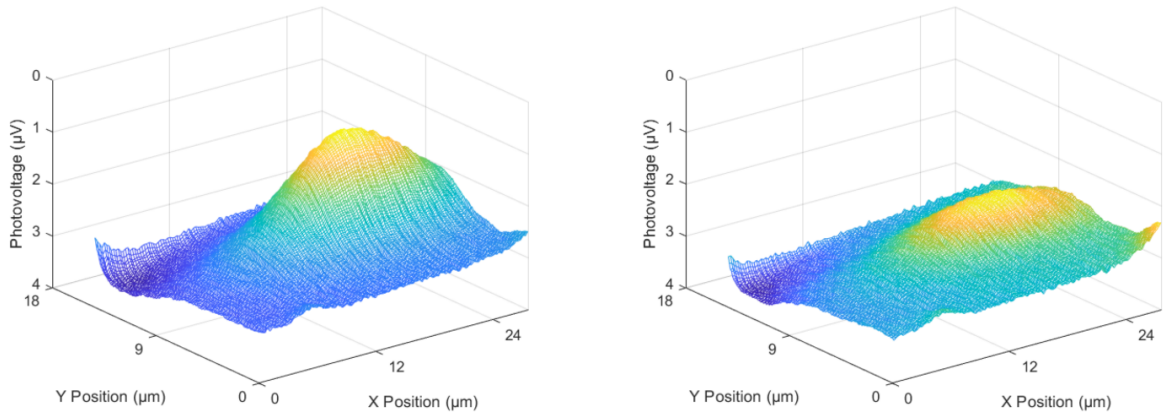

Figure 2.17: Both figures show an SPCM measurement performed by scanning the probe laser with a stationary pump laser; left shows a time delay of $\delta t \approx 100$ps, right shows a time delay of $\delta t \approx 0$ps. The photovoltage suppression is clearly shown to be a local feature.

2.4.1 Spatially resolved Ultrafast Photovoltage

The simplest experiment is to spatially scan the probe while holding the pump stationary. The delay time between the two pulses is fixed during the scanning. These measurements show that the photovoltage suppression is a local feature–as the probe moves away from the pump about 10 μm, the baseline photovoltage is recovered (fig. 2.17). The envelope of the signal suppression shows a Gaussian profile, but with a width that is larger than the laser spot size (3μm). In order to develop a more quantitative picture of the spatial dynamics of our UTP measurement, we can repeat the measurement used to generate figure 2.17 for many values of δt. Using a macro program, SPCM scans are sequentially captured while the delay stage moves between each completed scan with a small change in time delay. An automated Python script will take this data set–which generally consists of roughly 100 SPCM scans–and compile the magnitude of the photovoltage for every value of δt. These values can be arranged into a map, which allows us to extract a spatial map for the values of t_0. When the pump and probe are focused at the same location, t_0 has an obvious interpretation of being the moment where $\delta t = 0$. Equivalently, t_0 is the moment in time where the pump interacts most strongly with the probe, resulting in the largest photovoltage suppres-

sion. This is evidenced by the cross-over of the line scans at probe positions away from the pump position (figure 2.18). By the principle of locality, the separation of pump and probe requires the transit of information between injection sites–there cannot be spooky action at a distance[121]. As t_0 changes when the probe moves from the pump injection site, we can extract the time carriers need to travel to the probe site, and thereby deduce the velocity of the carriers. Figure 2.18 shows the various stages of the Python output to produce a t_0 map: the many different δt scans are tabulated on a pixel-by-pixel basis to produce a map, which can then be used to deduce a carrier velocity via[122]:

$$v = \frac{\Delta r}{\Delta t_0}. \tag{2.22}$$

From the plot in figure 2.18,

$$v_{right} = \frac{20\mu\text{m} - 12\mu\text{m}}{464\text{ps} - 424\text{ps}} = 2 \times 10^5 \text{m}\,\text{s}^{-1} = 0.4 v_F \tag{2.23}$$

$$v_{left} = \frac{||8\mu\text{m} - 12\mu\text{m}||}{464\text{ps} - 424\text{ps}} = 1 \times 10^5 \text{m}\,\text{s}^{-1} = 0.2 v_F. \tag{2.24}$$

where the Fermi velocity in bismuth selenide is $v_F = 5 \times 10^5 \text{m}\,\text{s}^{-1}$ [123]. This analysis assumes that the equivalence between equations 2.3 and 2.4 is still valid when the two pulses are spatially separated.

The measurement took place $\approx 10\mu$m away from the preamp electrode, out of the device channel (similar to the configuration in figure 2.6, but further away from the electrode). The asymmetry between the two sides of the t_0 map is repeatable.

2.5 Models for Ultrafast Photocurrent Studies

2.5.1 Analysis on the Ultrafast Results

The photocurrent suppression at zero delay time can be understood by the nonlinear photocurrent dependence on fluence. Previously we have observed a rapid decrease in

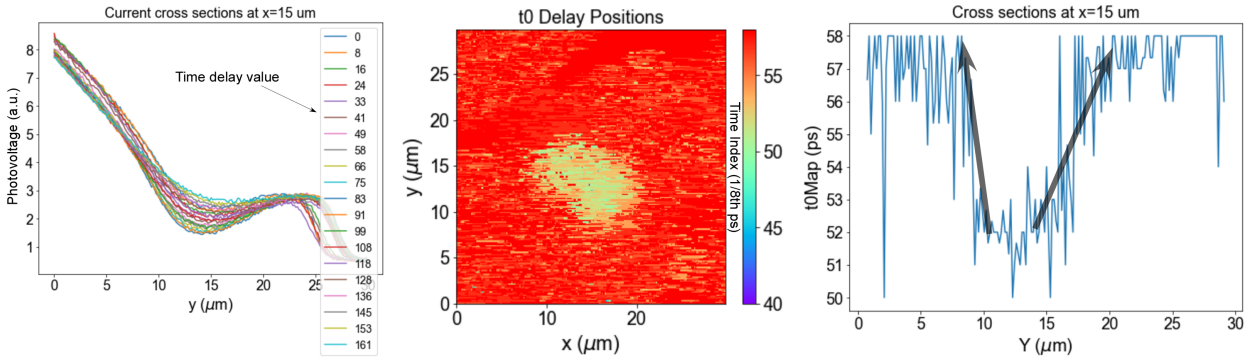

Figure 2.18: Carrier velocity measurement via ultrafast SPCM at 78 K. Left: overlain line cuts of an SPCM profile for different value of t_0, illustrating change in photovoltage in the pump injection site. Center: spatial map of t_0, which is produced by finding t_0 at every pixel. Right: line cut of t_0 map showing a shift in t_0 as a function of position. The arrows show the range over positions used to deduce the carrier velocity. The probe fluence is $\mathcal{F} = 0.64\mu\text{J/cm}^2$ and the pump fluence is $\mathcal{F} = 44\mu\text{J/cm}^2$. The measurement is taken outside of the device channel to eliminate drift fields, and is far away from the depletion region.

photocurrent decay length and magnitude as we increase the CW laser intensity[52]. The ultrafast study here is consistent with this previous work. However, the time resolution provides a deeper understanding of the mechanism accounting for the suppression.

To generate photocurrent, the locally excited carriers must travel to the metal contact. Since the out-of-channel nanoribbon is free of electric field, the dominating mechanism of carrier migration is by diffusion, rather than drift. The diffusion length of the photogenerated carriers is given by $L_D = \sqrt{D\tau}$, where D is the diffusion coefficient and τ is the carrier lifetime. The shorter L_D at high intensity can then be attributed to two possible factors: (1) faster carrier recombination, and (2) reduced diffusion coefficient. The steady state SPCM cannot determine which of these two factors play a major role, while the time-resolved photocurrent study provides key insight in that the carrier recombination time is unlikely reduced at higher fluence. As shown in fig. 2.14, the recovery time actually increases at higher pump fluence. Though the recovery time is not a direct measure of carrier recombination time because of the convolution of carrier escaping the photoexcitation area, it at least provides a lower limit for the carrier recombination, i.e., $\tau < \tau_R$ according to Eq. 2.14. On the other hand, the transient reflectance measurements over a similar fluence range[43]

showed an opposite trend in that the recombination lifetime is reduced at higher fluence. The reason for such contradictory results is unclear and deserves further studies such as by measuring time-resolved photocurrent and reflectance in the same device.

If the carrier recombination lifetime is confirmed not to be the reason for diffusion length reduction, the diffusion coefficient must be the culprit. The diffusion coefficient is related to the carrier mobility, $D = \mu k_B T/q$. The carrier mobility may be influenced by the high fluence. For example, the high fluence may increase the crystal temperature, which cause stronger phonon scattering and mobility reduction. However, we do not think this can account for the up to 95% photocurrent suppression at high fluence (fig. 2.14). This is because the estimated temperature increase at the highest fluence is only 5 K, using

$$\Delta T = \frac{Pt}{\kappa A} \tag{2.25}$$

where P = 125 μW is the time-averaged laser power, $\kappa = 1$ W/mK is the thermal conductivity of the SiO_2, $t = 300$ nm is the SiO_2 thickness, and $A = \pi(1.5\mu m)^2$ is the laser spot area.

Instead, the most likely mechanism for the mobility reduction is by the laser induced dissociation of excitons at high fluence. As introduced in Chapter 1 and detailed in our early work[52], the highly nonlocal photocurrent indicates superfluidic-like exciton condensate in TIs. The dense electrons and holes injected by laser can effectively screen the electric field and reduce the exciton binding energy, forbidding the exciton formation. If dissociated at high fluence, the unbound carriers become fermions and suffer from scattering with greatly reduced mobility. This explains the large observed photocurrent suppression. Below we discuss possible Mott transition from excitons to electron-hole plasma at high carrier density.

2.5.2 Exciton Mott Transition

A candidate theory for these observations is the exciton Mott transition (named for Neville Mott[124]), which is a special case of a metal-insulator transition. In this picture the change in carrier density (which is approximately proportional to the fluence of the

laser) induces screening that reduces the Coulomb energy of the system, thus inhibiting the formation of excitons and restricting the carrier type to an electronic plasma[125]. In our UTP experiment, we directly tune the carrier concentration via choice of pump fluence. This can lead to exciton dissociation into an electronic plasma, which is expected to have much slower transport properties[126].

The germinal concept for the Mott transition lies in the consideration of the conditions for bound states in screened Coulomb potentials. The Thomas-Fermi screening picture gives a Coulomb potential that is modified by the Thomas-Fermi screening length[127],

$$U(r) = -\left(\frac{e^2}{r}\right) e^{-k_s r}. \tag{2.26}$$

where ${k_s}^2 = 4(3\pi n)^{1/3}/a_0$ and a_0 is the Bohr radius. This function is known to have bound states when $k_s < 1.19 a_0$[128]. This can be expressed in a famous form as the Mott criterion:

$$n^{-\frac{1}{3}} = 2.27 a_0. \tag{2.27}$$

If bound states do not exist, then the states under consideration will be delocalized and therefore metallic; if bound states are present, then the states under consideration will describe an insulator. Mott's description of a metal-insulator transition is the result of electron-electron correlations, and there exist other important metal-insulator transition mechanisms: the Peierls transition, which is driven by electron-phonon interactions[129]; and Anderson localization, in which sufficiently high levels of disorder in a lattice will localize wavefunctions enough to suppress diffusion[130]. These metal-insulator transitions can be described with some sense of universality with dynamical mean field theory[131].

This concept becomes interesting when we consider a reversible crossover between insulating and metallic states by tuning the carrier concentration. The Mott transition can be accomplished optically with a simple tuning of free carriers so that eq. 2.26 will have generically unbound states[133–135]. The excitonic flavor of the Mott transition comes in when

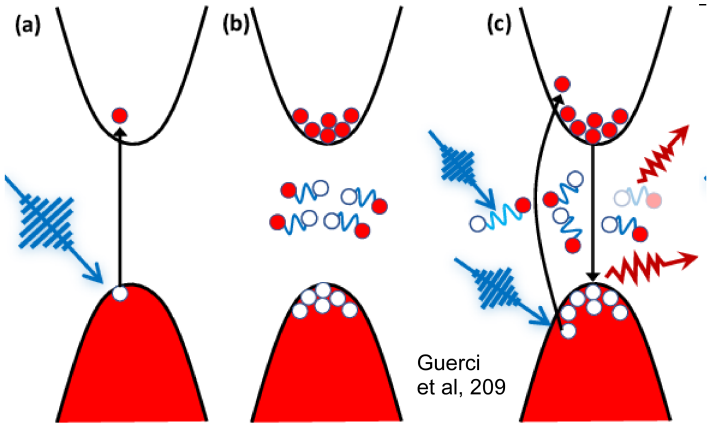

Figure 2.19: Schematic of excitonic Mott transition. (a) Semiconductor in equilibrium absorbs a photon, exciting an electron into the conduction band. (b) Quasistatic formation of excitons in the bandgap, with holes and electrons in the conduction and valence band respectively. This process can occur on the Dirac cone[1]. (c) As the population of electrons and holes reaches a critical density, the Coulomb energy decreases and the formation of excitonic bound states is prohibited. Figure sourced from[132].

one considers the criterion for the formation of excitons: $\alpha = E_C/E_K$[1], which is the ratio between Coulomb and kinetic energy. If this ratio is of unity or larger, then excitons may be formed. If the system experiences an insulator-metal transition then the Coulomb energy will become very small as screening becomes very efficient (summarized in fig. 2.19), which results in our aforementioned excitonic Mott transition[136]. Exciton Mott transitions have been observed in pure silicon[137], quantum wells[138], and metal oxides[133]. Zinc oxide is particularly well studied, and estimates for the critical carrier density such that the Thomas-Fermi screening length $1/k_s$ produces metallic states for this system range from $1.5 \times 10^{18}\text{cm}^{-3}$ to $6 \times 10^{18}\text{cm}^{-3}$[126,133,139].

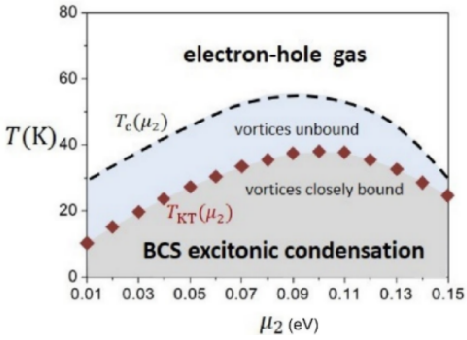

Figure 2.20: Relationship between chemical potential and condensation temperature, indicating an optimal carrier density regime. Figure sourced from[73].

Mott transitions in topological insulators have been a delightful source of discussion for theorists[140–144], but have thus far failed to appear in a real experimental measurement.

The exciton Mott picture is very immediately appealing: it provides a mechanism for a local suppression of photocurrent that requires a finite fluence to activate and increases with magnitude with fluence.

For our intrinsic bismuth selenide samples, the exciton Bohr radius at the surface is estimated as $a_0 = 110\text{nm}$[52]. Given the Mott criterion (2.27), this gives a critical density that should be in the ballpark of $n \approx 10^{14}\text{cm}^{-3}$.

2.5.3 Mahan Exciton Formation

Even when Bi_2Se_3 is at its most intrinsic, it's still–formally speaking from the perspective of a 3D Mott transition–a bad metal[145]! If there's a single saving grace for theoretical physicists, it's that they're quite excellent at finding ways to circumvent the laws of nature. In 1966, Gerald Mahan published a paper that describes how excitons can still form in semiconductors above the Mott criterion[146]. These metastable[147] excitons have an approximate form for their binding energy (E_B) that is small when the screening wavevector (k_s) is large:

$$E_B = \left(\frac{2{p_F}^2}{\mu_m}\right) \exp\left(-1/\Delta\right) \tag{2.28}$$

$$\Delta = \frac{1}{2\pi p_F a_B} \ln\left(1 + \frac{4{p_F}^2}{{k_s}^2}\right), \tag{2.29}$$

where μ_m is the electron-hole reduced mass. A key feature of this model is that it relates the binding energy of the exciton (which according to[1,52] should be larger at lower temperatures) to screening length (which generally decreases as the density becomes larger, which is easy to modulate via gate voltage or pump fluence).

2.6 Outlook for Future Work

The outlook for UTP experiments in intrinsic bismuth selenide is bright. We have demonstrated a great degree of control over the photoresponsivity of intrinsic bismuth selenide. Further work is necessary to better understand the exciting but puzzling results.

1. **Doping dependence:** We want to measure bismuth selenide without Sb doping for comparison. The sample without Sb is much more n-doped with fermi level in the conduction band. The photocurrent is such examples tends to be much weaker and local even at low temperatures. We expect the high doping will shorten the carrier recombination lifetime and the stronger screening will forbids the exciton formation. Comparison of time-resolved photocurrent results will help better understand the doping effect on the exciton formation and transport.

2. **Lower temperatures:** So far, most work is done with liquid nitrogen. Our group has recently set up the helium recycling system, which allows more efficient usage of liquid helium. The lower temperature about 7 K can be reached in the optical cryostat when using liquid helium. At this temperature, we expect stronger photocurrent signal as a result of more robust exciton formation, which can improve the signal to noise ratio of our data. This is particularly helpful to our ultrafast SPCM measurements used to determined the exciton velocity. We can carefully obtain the distance to transit time relation, to understand whether it is diffusive or ballistic.

3. **Transient reflectance:** In addition to photocurrent, we plan to also measure the transient reflectance (TR) in the same device. Though TR has been measured previously in our samples[43], obtaining both TRPC and TR in the same device can mitigate the device-to-device variation issue and provide more concrete comparison between these two methods. We have attempted to measure TR in our devices. One difficulty is to block the pump beam in the normal incidence configuration. Cross-polarization does not seem to completely filter out the pump beam. We plan to try double the frequency of the pump beam and then use a long pass filter to only collect the probe beam reflectance.

4. **Photon energy dependence:** We have performed TRPC with photon wavelength in the range of 690-1040 nm. There seems to be no signficant behavior change in this

range. We plan to use BBO to double the frequency of the ultrafast laser to the shorter wavelength range. It has been reported the second Dirac cone about 1.6 eV above the first Dirac cone may have high impacts on the carrier relaxation dynamics[148].

5. **Device modeling:** To better understand the temperature, gate, and fluence dependent photocurrent response in TIs, we plan to carry out device modeling. Finite element methods using COMSOL or home-made programs will be used to solve time-dependent drift-diffusion equations. A few candidate mechanisms, including photo-Dember effect, charge trapping, and exciton-plasma Mott transition, can be considered in the modeling. The simulation results will be compared to the experimental observations to identify the key mechanism.

6. **Helicity dependence:** We also want to carry out the photon helicity dependent photocurrent in ultrafast setup. The spin-momentum locking of the topological surface states dictates formation of spin-triplet excitons as predicted from theory[73]. As a result, the travel direction of the excitons is coupled to the photon-helicity (see more details in Chapter 4). Time resolution would be useful to measure the spin relaxation time. The spatiotemporal photocurrent technique is expected to generate rich information of spin polarization and diffusion process.

Chapter 3

Magnetic Field Dependent Photocurrent in Intrinsic Bismuth Selenide

The remarkable surface states in Bi_2Se_3 and other TIs are protected by time-reversal symmetry. This statement immediately makes the breaking of time-reversal symmetry– and therefore the topological protection of the surface states–immediately appealing. The simplest way to remove time-reversal symmetry in a system is through the application of a magnetic field, of which there are three major approaches:

1. **Magnetic Doping**: the inclusion of magnetic dopants like chromium[149], cobalt[150], or iron[151] during the growth process s is an effective way of breaking time-reversal symmetry. In addition to the permanence of these dopants, they generically require significant modifications to the synthesis procedures. This route has enabled observations of the Kondo effect[151,152] and the quantum anomalous Hall effect[150] to be observed in Bi_2Se_3.

2. **Magnetic Interface Engineering**: arguably a subset of magnetic doping, magnetic interface engineering is a more niche method of straining time-reversal symmetry. Magnetic materials that also superconduct like niobium can induce exotic pairing between the superconductor and surface states in Bi_2Se_3[153], and the selection of magnetic materials with Curie temperatures accessible by cryogenic systems (e.g. europium sulfide, $T_C = 16\text{K}$) can make magnetic tuning reversible[154]–although the nature of the coupling between europium sulfide and Bi_2Se_3 has been controversial[155].

3. **Application of External Magnetic Field**: taking a chunk of some material, throwing it in a cryostat, and applying a magnetic field is the most time-honored method of studying s under magnetic duress. External magnetic fields also have the advantage of being fully reversible and tunable. This is classic meat-and-potatoes condensed matter physics.

Magnetic doping and magnetic interface engineering are powerful techniques, but their biggest limitation is that they are not fully reversible. External magnetic fields are appealing because they allow experimentalists to play with time-reversal symmetry in a continuous and reversible manner.

3.1 Classical Magnetotransport

Magnetotransport-at-large can be identified from the Lorentz force:

$$\mathbf{F} = q(\mathbf{E} + \mathbf{v} \times \mathbf{B}). \tag{3.1}$$

Carriers moving at a constant velocity in a uniform external magnetic field will experience a force perpendicular to their motion, which via Newton's second law is equal to centripetal

acceleration:

$$\frac{mv^2}{r} = qvB, \tag{3.2}$$

which in turn defines the cyclotron frequency $\omega = \frac{v}{r} = \frac{qB}{m}$. For a carrier in a solid, the mass is renormalized by the effective mass of a carrier in a solid, m^*, but this picture is only valid for very short time scales because the carrier will scatter off of the solid's lattice after the carrier's mean free time τ.

For a macroscopic amount of carriers under an external voltage bias, we can define the drift velocity, $\mathbf{v}$, as the average velocity that the carriers achieve between scattering events with the lattice. The drift velocity is proportional to the applied bias, which allows us to define the mobility, μ, via the relationship $\mathbf{v} = \mu\mathbf{E}$. We can then express the Lorentz force law in terms of the velocity of a carrier that interacts with a lattice as:

$$\mathbf{v} = \frac{\mu}{1 + (\mu B)^2} \left(\mathbf{E} + \mu \mathbf{E} \times \mathbf{B} + \mu^2 (\mathbf{B} \cdot \mathbf{E}) \mathbf{B} \right) \tag{3.3}$$

$$= \frac{\mu}{1 + (\mu B)^2} \left(\mathbf{E}_\perp + \mu \mathbf{E} \times \mathbf{B} \right) + \mu \mathbf{E}_\parallel. \tag{3.4}$$

This shows that the velocity of a current will tend to decrease (i.e. resistance will increase) by increasing the strength of the magnetic field.

3.2 Quantum Flavors of Magnetotransport

We've seen that the origin of the existence of magnetoresistance can be understood classically and through the Drude model. However, many of the interesting experimental signatures in Bi_2Se_3 are fundamentally quantum mechanical in nature: These studies include many flavors of magnetoresistance studies, including those that have demonstrated weak antilocalization (that show both straightforward weak antilocalization[156], as well as a regime crossover between weak antilocalization and Shubnikov-de Haas oscillations[157]),

linear magnetoresistance[158–160], negative magnetoresistance[61,161]. Extensions of these experiments have achieved the demonstration of the inverse spin hall effect through purely transport measurements[162] by abusing the strong spin-orbit coupling of bulk and surface states[163], as well as the Aharanov-Bohm effect[164] (fig. 3.3). In the author's opinion, the demonstration of the Aharanov-Bohm effect in Bi_2Se_3 is especially neat. Let's describe two quantum magnetotransport features that have been important for bismuth selenide: weak antilocalization and the Aharanov-Bohm effect.

3.2.1 Weak (Anti)Localization

Weak localization (antilocalization) is the observation of a decrease (increase) in conductivity at cryogenic temperatures in disordered systems. The origin of weak localization comes from a special case of diffusive transport: quantum diffusive transport, where the mean free path ℓ is much smaller than the device dimension L but smaller than the phase coherence length ℓ_ϕ so that carriers can scatter many times while still preserving their phase information. In this regime, it is possible that carriers will scatter off impurity sites in such a way that their trajectories overlap–ballistic and semiclassical diffusive transport cannot exhibit weak localization[165] (fig. 3.1). If phase information is preserved through this process then constructive interference will occur for every clockwise and anticlockwise loop, thus localizing the carrier wavepacket, causing the net conductivity to decrease. Of course, this effect relies on carriers forming loops so lower dimensional systems tend to show stronger weak localization conductivity corrections. The weak antilocalization flavor occurs in systems with strong spin-orbit coupling (e.g. bismuth selenide). The carrier spin will precess as it completes a quantum diffusive loop, and a carrier that travels through the opposite trajectory will be guaranteed to have the opposite sign. This causes destructive interference, which delocalizes the carrier wavepacket and therefore increases the net conductivity. Applying a magnetic field to a system will kill time-reversal symmetry and cause the carriers to dephase over shorter distances, which will progressively eliminate the conductivity correction.

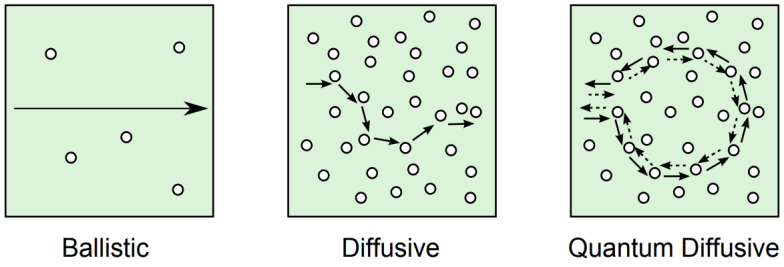

Figure 3.1: Left: carriers will not interact with a lattice in purely ballistic transport. Center: diffusive transport. Right: quantum diffusive transport, which serves as the origin of weak (anti)localization. Simultaneous clockwise and anticlockwise transport through this loop is essential. Figure sourced from [165].

Thus, the most famous experimental signature of weak (anti)localization is a conductivity (peak) dip at zero field. Because phase information is generically more durable at lower temperatures, there is additionally a logarithmic correction to conductivity as temperature decreases [166] (fig. 3.2).

Generically speaking, weak antilocalization measurements are powerful characterization tools for bismuth selenide because the mean free path is short ($\ell \approx 10$nm), while the phase coherence length can range from $\ell_\phi \approx 100$nm to $\ell_\phi \approx 1000$nm [167]. Weak antilocalization behavoir dominates in bismuth selenide due to the strong spin-orbit coupling present in the material, but there have been observations of a crossover between weak localization and weak antilocalization by opening a gap in the Dirac cone: this has been accomplished by magnetic doping [168,169] and magnetic interface engineering [170], but also by studying films that are thin enough to open a gap [171,172] via TSS hybridization that occurs from a non-zero overlap integral [45].

The simplest way to quantitatively describe weak localization behavior (assuming two dimensional transport with strong spin-orbit coupling) is to use the Hikami-Larkin-Nagaoka equation [173]:

$$\sigma(B) - \sigma(0) = \alpha \frac{e^2}{2\pi^2 \hbar} \left[\ln\left(\frac{B_\phi}{B}\right) - \psi\left(\frac{1}{2} + \frac{B_\phi}{B}\right) \right], \tag{3.5}$$

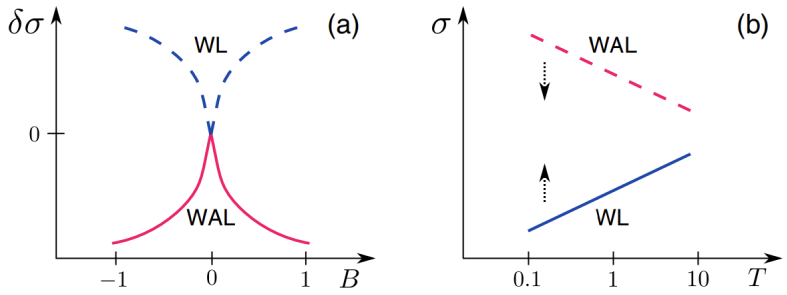

Figure 3.2: Left: conductivity correction from weak (anti)localization that manifests itself as a suppression (enhancement) that disappears as an applied magnetic field causes destructive dephasing. Right: logarithmic correction that suppresses (enhances) conductivity for weak (anti)localization. Figure sourced from [166].

where ψ is the digamma function and B_ϕ is related to the phase coherence length, ℓ_ϕ: $B_\phi = \hbar/4e{\ell_\phi}^2$.

The phase coherence length is a parameter that describes how far carriers can travel in a magnetic field before they lose their phase information–a large phase coherence length should only be present in samples that have very small amounts of scattering sites. The strongest constraint on the coherence length magnitude in bismuth selenide are electron-electron interactions [167] and coupling of surface states to electronic puddles in the bulk [174]. The α factor at the beginning of the HLN equation is a fitting parameter that is usually interpreted as the number of available transport channels where each band contributes a factor of $1/2$ [175], and is positive (negative) for modeling weak (anti)localization. The HLN equation is usually only fit over a very small field range, as even moderate fields will cause carriers to sufficiently dephase to cause the weak antilocalization contribution to vanish.

3.2.2 Aharanov-Bohm Effect

The Aharanov-Bohm effect, which describes how the modulation of the phase information of a wavefunction can cause oscillation interference behavior, is one of the great triumphs of modern physics: its existence transparently confirms that physical potentials are *real* objects, and not just mathematical structures.

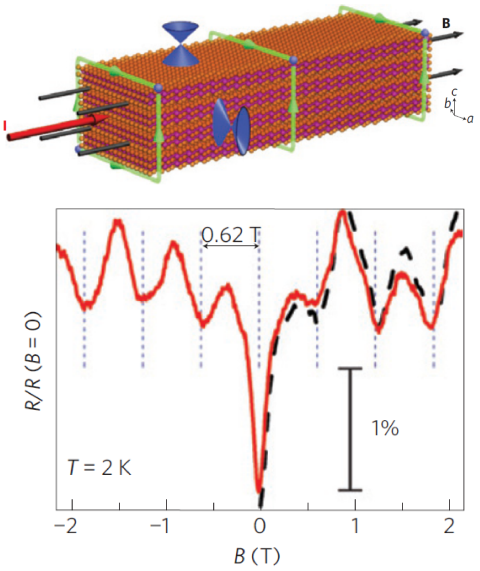

Figure 3.3: Top: schematic of an Aharanov-Bohm effect in Bi_2Se_3, showing parallel magnetic field (B), transverse current (I), and Dirac cones on surface of device (blue cones), and phase accumulating carriers (green lines). Bottom: Conductivity data produced from Top, showing periodic oscillations indicative of Aharanov-Bohm effect. Figure sourced from [164].

The magnetic flux through the center of the device provides an Aharonov-Bohm phase:

$$\Delta\phi = 2n\,(2\pi)\,\frac{\phi}{\phi_0}, \tag{3.6}$$

where n is the winding number [176–178] associated with the carrier loop. For topologically trivial systems $n = 0$, so no interference patterns are observable. For $n \neq 0$, interference patterns will emerge with a $\phi_0/2$ dependence [33]. Intuitively, 3D systems with bulk states will not garner a winding number as they cannot have a large number of loops that contain a narrow range of magnetic flux, but the Aharonov-Bohm effect can be observed in non-topological systems like carbon nanotubes [179], GaAs/AlGaAs quantum wells [180], metal rings [181], and even charge density waves [182].

3.3 Viable Magnetotransport Experiments with Intrinsic Bismuth Selenide

As discussed in the introduction, we believe that our observations of extended photocurrent in Bi_2Se_3 are necessarily tied to the topological surface states of the material. It should be immediately appealing to any researcher to attempt to modify this photoresponse

by attacking the time-reversal symmetry via the application of an external magnetic field. There is some historical context for studying excitonic transport under an applied magnetic field: namely in the probing of an excitonic insulator phase in $TmSe_{0.45}Te_{0.55}$ [183] or a zero-gap InAs-GaSb bilayer quantum well [184]. There are three reasonable experiments to study:

3.3.1 Suppression of nonlocal photocurrent by strong magnetic field (fig. 3.4).

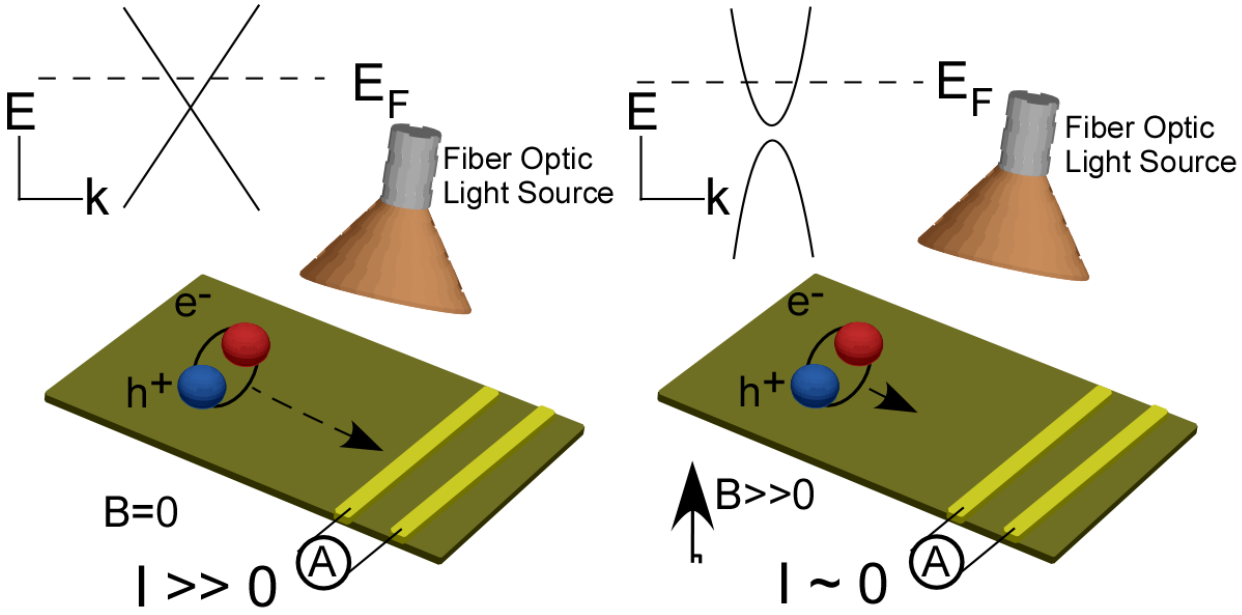

Figure 3.4: Experiments for illuminated magnetotransport studies on intrinsic Bi_2Se_3. Left: under zero applied magnetic field, the Dirac cone is intact on the surface of the Bi_2Se_3 device. Upon global illumination via an optical fiber coupled to a laser, the total photoresponse (measure photocurrent or photovoltage) integrated over an entire device with asymmetric contacts will yield a non-zero value for photoresponse. Right: The application of a strong magnetic field destroys time-reversal symmetry in the device and opens a large gap in the Dirac cone. Exciton formation is disrupted, and the photoresponse becomes more localized to the contact. This causes the total integrated photoresponse to become nearly zero (asymmetry in band bending will always make one contact more efficient).

Exciton condensation occurs at a relatively high temperature, with a T_c of roughly 40 K [52]. The high T_c is related to the vanishing electronic effective mass of the TI surface state [1]. It logically follows that Bi_2Se_3 has robust gapless transport properties as long as time

reversal symmetry is respected. If time reversal symmetry is broken by an external magnetic field, then a gap will open in the surface state spectrum, which is expected to suppress the formation of exciton condensation (fig 3.4). Therefore, studying the photocurrent response as a function of applied magnetic field can shed light on the precise mechanism for the formation of excitons on the surface of these devices. Standard superconducting magnet systems top out between 5T and 10T–if a stronger magnetic field is required to break the gapless state, one can coat the TI surface with a thin layer of magnetic material to significantly increase the local magnetic field at the surface. Candidates for this interface are EuS[185] and MnSe[186,187], which–beyond their excellent magnetization properties and optimal Curie temperatures (18K for EuS[188] and 42.3K for MnSe[189])–they both have reasonable lattice matching to insure that minimal interfacial strain is applied to the TI surface[187,190].

3.3.2 Suppression of magnetoresistance under weak to medium magnetic field (fig. 3.5).

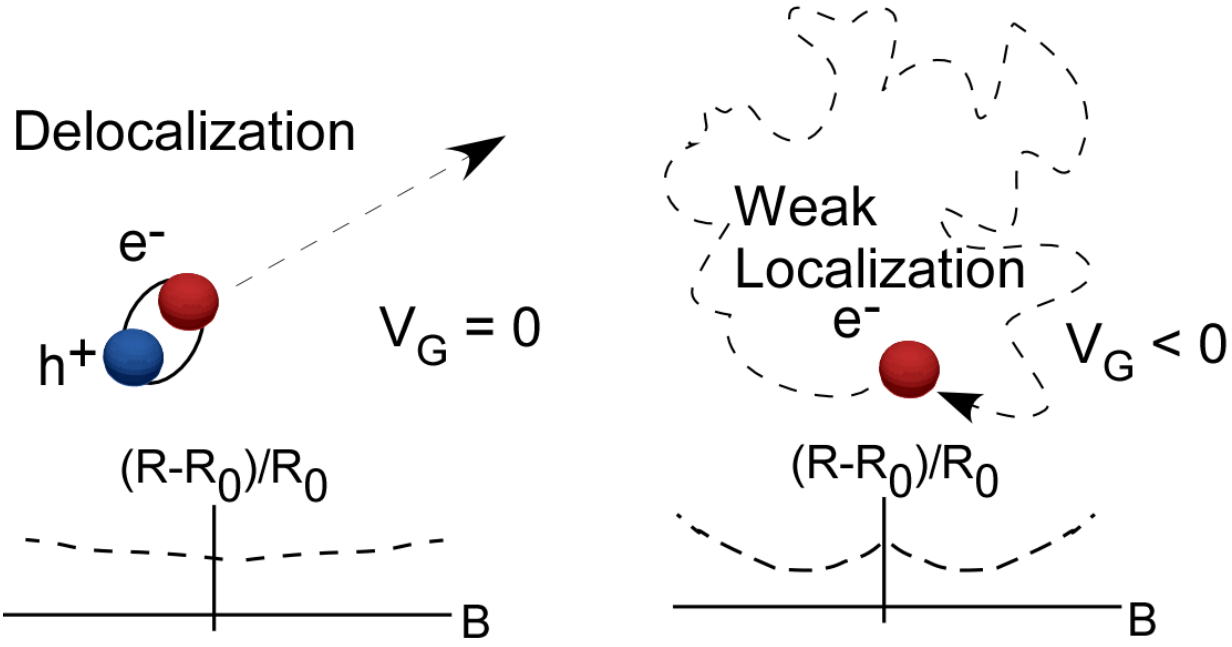

Figure 3.5: Left: highly delocalized excitons cannot form interfering loops, resulting in a vanishingly small contribution to weak antilocalization (WAL). Right: free carriers at the surface of a TI readily form intersecting loops that contribute to WAL.

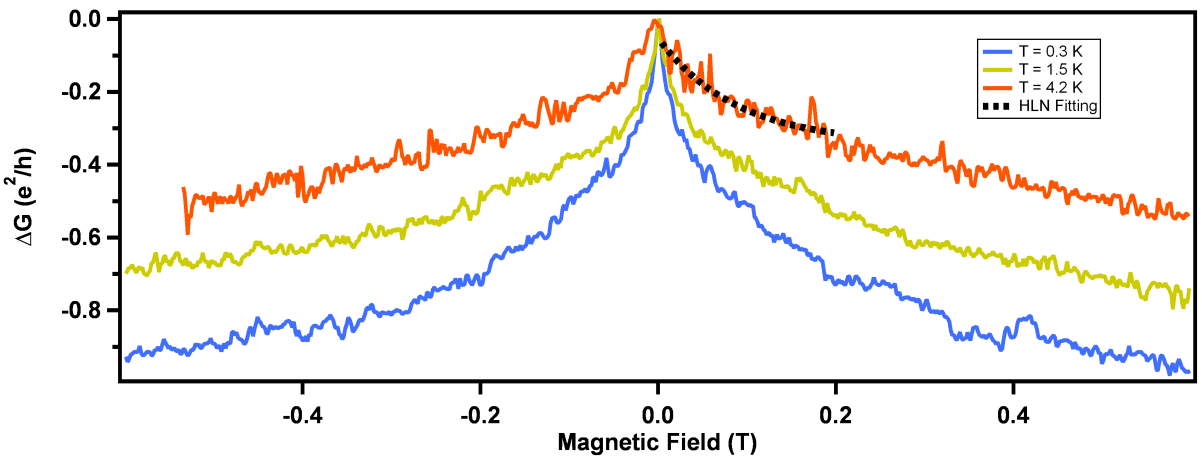

Figure 3.6: Dark magnetoresistance data on an intrinsic bismuth selenide MOSFET, showing sharper weak antilocalization peak at lower temperature.

Under relatively low magnetic fields up to a few Tesla, photo-modulated MR can be used to provide key evidence of exciton formation and delocalization. Bi_2Se_3 has long been observed to display weak (anti)localization signatures (fig 3.5(right)) in magnetotransport, namely a dip in resistance values for small magnetic fields. Under illumination, exciton-dominated magnetotransport should not show this dip, as the wavefunctions will be completely delocalized across the surface of the device (fig 3.5(left)). As the Fermi level is tuned into the valance band via gate voltage, we expect to impede exciton formation and recover the weak localization signature. Similar behaviors of vanishing MR have been demonstrated for InAs/GaSb bilayer by Dr. Pan[184].

3.3.3 Exciton induced phase shift in Aharanov-Bohm oscillations. (fig. 3.7).

Because the charge transport occurs at the TI surface, a magnetic flux parallel to the length of the nanoribbon can cause periodic resistance oscillations through the Aharanov-Bohm effect.This concept is supported by work with our international collaborators, who have measured quantum oscillations in a device channel with a length up to $70m$, thanks to the superior sample quality[191]. The nature of our carriers, excitonic or free, will have profound impacts on the interference effects that we will observe. Because of their non-zero

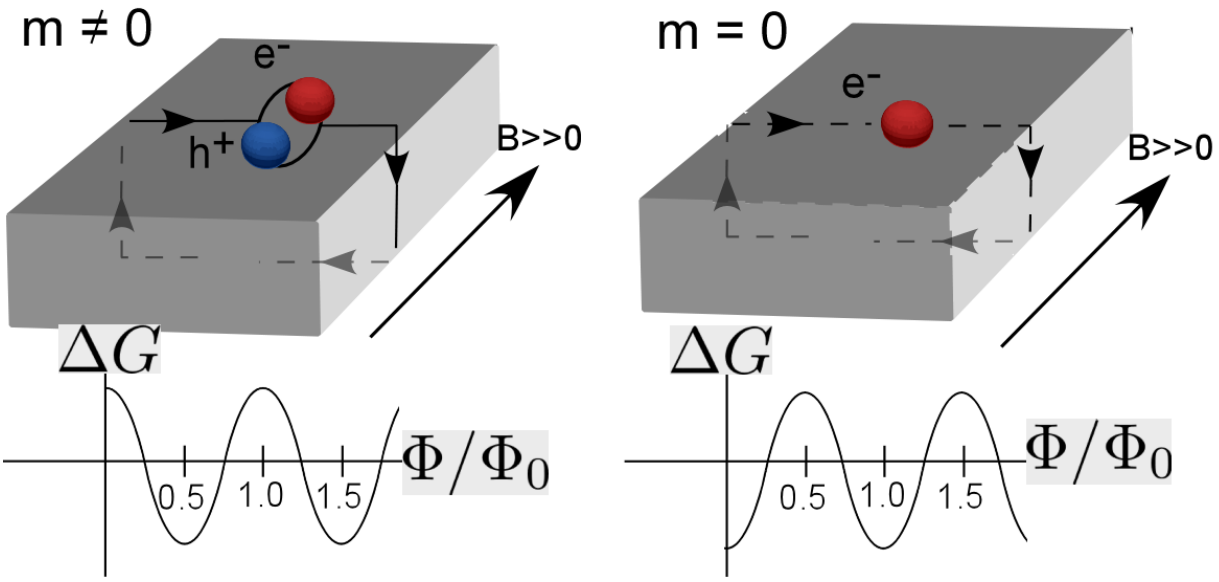

Figure 3.7: Aharanov-Bohm effects should have a π phase shift between excitons and free carriers in a TI (left) from a topologically trivial loop (right) because the formation of excitons opens a many-body gap in the Dirac state.

Berry curvature, the AB effect in topological materials shows a π offset[192] in interference patterns. However, if excitons are formed, such a phase difference should vanish because exciton formation should open a gap in the topological surface states (fig 3.7). Despite being chargeless, there are still mechanisms for excitons to accumulate a wavefunction phase difference in a magnetic field[193].

Aharanov-Bohm experiments in bismuth selenide depend sensitively on the orientation of the magnetic field[194]–in-plane components will progressively dephase carriers and rapidly suppress oscillatory behavior.

3.4 Results and Discussion For Weak Antilocalization Studies

Collaborating with Dr. Wei Pan, a distinguished member of the technical staff at Sandia National Laboratory at their Livermore site, we devised an experiment to test the hypothesis of fig. 3.5. Using a Helium-3 cryostat (with a minimum temperature of $T = 0.3$K achievable with a sorption pump) with superconducting magnets (maximum field $B = 5$T), we first performed measurements to compare the coherence length and FET mobility of a

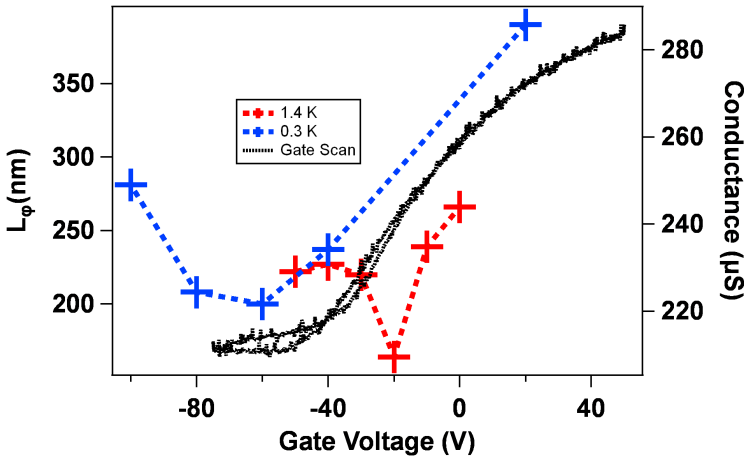

Figure 3.8: Plot of coherence length as a function of both temperature and gate voltage extracted from figure 3.6. The coherence length at $T = 0.3$K follows the FET mobility data very closely.

prototypical device (fig. 3.8). In the device presented in figure 3.8, we see that the gate scan shows the usual signatures of an n-type device with a charge neutrality point near $V_G = -60$V. What is slightly more surprising is that the fit coherence length follows the gate scan data very closely (the $T = 0.3$K data fits much more closely than the $T = 1.4$K data, which has a likely bad data point).

We used a simple mechanical structure to couple an optical fiber to our bismuth selenide MOSFET. A laser was launched via pigtail fiber coupler to produce an illumination intensity of roughly 1mW with a 1cm spot size with a wavelength of 450 nm. Though the large spot size does not allow spatially resolved photocurrent measurements, we can still obtain information on nonlocal photocurrent under uniform illumination using asymmetric devices. The device measured was intentionally fabricated with a long segment of the nanoribbon on one side of the device channel as shown in fig. 3.4. Since most optical absorption will occur in the out-of-channel long segment, photoexcitation in this long segment will dominate the photocurrent generation if the photocurrent is nonlocal. A shorter photocurrent decay length, induced by gate or magnetic field, will then result a reduction of the overall photocurrent significantly.

We performed magnetotransport measurements with and without illumination in such an asymmetric device (fig. 3.9) and performed the same fitting to the HLN equation. The data are relatively noisy mainly due to the low light intensity of about 1 mW/cm^2. Better

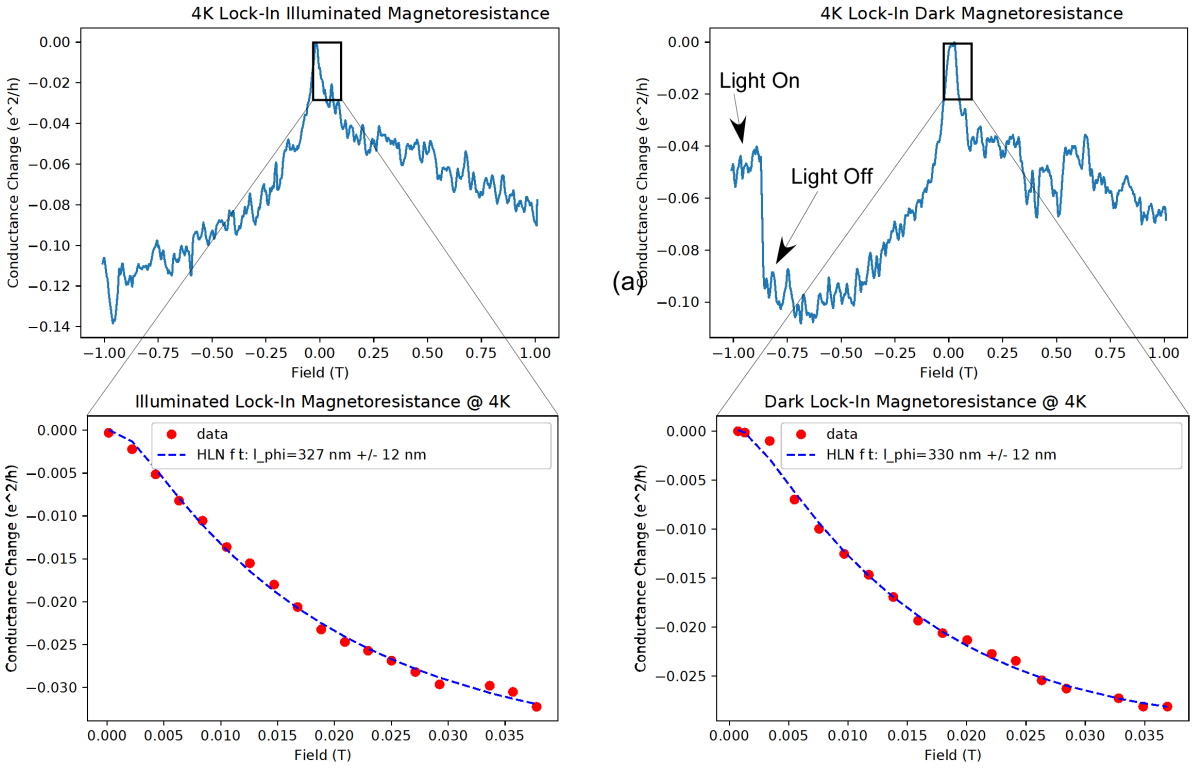

Figure 3.9: Illuminated weak localization data. Both sides show wide field scan magnetotransport data on top, with an inset of the HLN fitting of the data to a small field region on bottom. The left side is illuminated data, while the right side is dark data.

fiber alignment and laser focusing on the device should greatly improve the signal-to-noise ratio in the future. Conductance is reduced under a magnetic field both in the dark and under illumination, indicating WAL. The overall conductance experiences an offset when illuminated, but the HLN fittings are indistinguishable between illuminated and dark. Both give a coherence length about 330 nm at 4 K.

3.4.1 Discussion

The magnitude of the measured coherence length is comparable to previous reports in other bismuth selenide samples with values between 100nm and 500nm[195]. Interestingly, the comparison between gate scan and coherence length immediately shows that the coherence length is small when the chemical potential is near the charge neutrality point–i.e. that coherence length scales inversely with carrier concentration. This does go against conventional wisdom, in which shorter coherence lengths are associated with larger carrier concentration[196]. This unusual behavior may be caused by gate-induced switching from WAL to WL as we observed previously[61]. When the negative gate voltage tunes the Fermi level towards the charge neutrality point, we have observed that the MR changes sign from positive to negative in certain samples. As discussed earlier, WL (WAL) results in negative (positive) MR. In the n-type regime, the device shows WAL behavior under small B, which switches to WL at higher B, because the magnetic phase coherence time becomes shorter than the phase coherence time. In the intrinsic regime, the device stays WAL because the condition for switching cannot be met. The convolution of the WAL to WL switching in the n-type regime may cause a broadened magneto-conductance peak at zero magnetic field, leading to an apparent coherence length increase when extracting from the HLN fitting. Further work is necessary to clarify this interesting behavior.

Under the fiber optic illumination, the overall conductance shifts up by an offset as seen in figure 3.9. By subtracting the dark conductance, we obtained magnetic field-dependent photoconductance, i.e., $\Delta G(B) = G(B)–G_0(B)$, where $G(B)$ is the conductance

under light and $G_0(B)$ is conductance in the dark. As seen in Fig. 3.9left, interestingly, the photoconductance follows the same B dependence as the dark conductance, with a similar coherence length. Photogenerated carriers in the long segment move to the contact and create an electromotive force (EMF) because of charge separation by the contact band bending. The photoconductance is determined by the photogenerated EMF and the resistance of the channel,

$$\Delta G(B) = \frac{\mathcal{E}(B)}{R(B)V_{SD}} \tag{3.7}$$

where $\varepsilon(B)$ is the EMF created by photoexcitation, $R(B)$ is the channel resistance, and V_{SD} is the source-drain bias. As the channel resistance follows the WAL behavior, the photogenerated EMF appears to be independent of B. If the photogenerated carriers also follow WAL behavior, the EMF would increase under a magnetic field since carriers are more delocalized under B and can more easily reach contact and contribute to the EMF. However, if the photogenerated carriers form superfluid-like excitons, their dissipationless transport do not follow WAL. Some degree of delocalization is necessary to observe weak antilocalization in bismuth selenide, but ballistic transport cannot show conductivity corrections via weak antilocalization[165]. Therefore, this result supports the exciton condensate mechanism. However, we caution that the data is relatively noisy and cleaner results are needed to provide stronger evidence for B-independent EMF.

The conductance offset provided by the fiber optic illumination is a measurement of the electromotive force (EMF) generated by the light absorption. The device measured here has a long out-of-channel segment which dominates the photocurrent generation because of the highly nonlocal photocurrent (fig. 3.4). Photogenerated carriers in the long segment move to the contact and create an EMF because of charge separation by the contact field. Critically, illumination does not change the weak antilocalization fitting parameter for each peak, which suggests that this EMF is independent of magnetic field. Some degree of delocalization is necessary to observe weak antilocalization in bismuth selenide, but ballistic transport cannot show conductivity corrections via weak antilocalization[165].

3.5 Outlook for Future Work

We have obtained magnetoresistance results clearly indicating WAL and the coherence length is gate tunable. Under illumination the conductance is shifted by an offset independent of the magnetic field, suggesting the EMF generated by photogenerated carriers in the long nanoribbon segments is not influenced by WAL. These results are encouraging, but more work is needed to confirm this result.

First, we want to improve the laser intensity by better optical alignment of the fiber and better focusing of the laser onto the device. This should lead to less noisy data to better support the B-independent EMF. In addition, instead of measuring photoconductance which is convoluted by the change of the channel resistance by the magnetic field, we plan to directly measure the open circuit voltage which is equivalent to EMF. A magnetic cryostat may allow us to study more subtle spatial variations in our signal.

Second, we want to apply a stronger magnetic field to open the gap at the TI surface (section 3.3.1) and study the potential phase shift of the Aharanov-Bohm effect (section 3.3.5).

Chapter 4

Spin Physics, Photon Polarization, and Bismuth Selenide

Spin-dependent physics–marketed as spintronics in the industrial world[197]–provides a potentially achievable platform to enhance semiconductor device performance through the magnetic moment of the electron. Spintronics is appealing due to the addition of increased degrees of freedom (spin and charge) compared to standard electronics (charge), and have been proposed as platforms for quantum[198] and neuromorphic computing[199]. Bismuth selenide provides an interesting playground for spin physics on the basis of two facts: first, spin-orbit coupling provides a relatively efficient way of converting charge to spin current[200]; second, the spin texture (where the spin polarization is specified by the wavevector $\mathbf{k}$ of a carrier[201]) of the Dirac cone provide in optical selection rules that can directly probe spin-orbit degrees of freedom[202]. These features open a door to a broad class of helicity-dependent optical measurements to study spin physics in bismuth selenide, which is special because these measurements on standard MOSFET architectures[203] are understood as direct evidence that the surface states carry photocurrent[204,205].

In this chapter we will first discuss some basic features of spintronics and the methods used to probe them, then we'll discuss some simulation work on a particular spin-based effect

that may be observable in bismuth selenide, and then we'll conclude the chapter with a discussion of optical probes as used to study the extended photocurrent profiles of bismuth selenide.

4.1 Spin Physics

The physics of spin is extremely rich. We'll take a focused tour of spin-orbit coupling, the (inverse) spin Hall effect, and the vast menagerie of different spin-based photogalvanic effects.

4.1.1 The Central Concept: Spin-Orbit Coupling

The origin of spin-orbit coupling is manifestly relativistic in nature. When a carrier with momentum $\mathbf{p}$ moves in a magnetic field $\mathbf{B}$, it experiences the Lorentz force:

$$\mathbf{F} = q\left(\mathbf{E} + \mathbf{v} \times \mathbf{B}\right), \tag{4.1}$$

and possesses a Zeeman energy

$$\hat{H} = \mu_B \boldsymbol{\sigma} \cdot \mathbf{B}, \tag{4.2}$$

where μ_B is the Bohr magnetron and σ are the Pauli matrices. If a carrier moves in an electric field, it will experience an effective magnetic field in its rest frame

$$\mathbf{B}_{eff} \approx \frac{1}{mc^2}\mathbf{E} \times \mathbf{p}. \tag{4.3}$$

where $\mathbf{p}$ is the momentum of the electron and m is the effective mass of the electron. This field is the origin of the spin-orbit coupling, as it has an associated Zeeman energy that depends on momentum:

$$\hat{H}_{SO} \approx \frac{\mu_B}{mc^2}\boldsymbol{\sigma} \cdot \left(\mathbf{E} \times \mathbf{p}\right). \tag{4.4}$$

In crystals, the electric field is formed by a potential gradient ($\mathbf{E} = -\nabla V$), so the expression for the spin-orbit field is written as

$$\mathbf{w}(\mathbf{p}) = -\frac{\mu_B}{mc^2}(\nabla V \times \mathbf{p}). \tag{4.5}$$

Because spin-orbit coupling respects time-reversal symmetry, it follows that 4.5 must be antisymmetric in $\mathbf{p}$. This is only possible in systems without inversion symmetry, which is the first example of spin physics being a probe of crystal symmetry. The most famous example of this field is given by the Rashba Hamiltonian[206], which is generated by an interfacial electric field $\mathbf{E} = E_z\hat{\mathbf{z}}$:

$$\hat{H}_R = \frac{\alpha_R}{\hbar}(\hat{\mathbf{z}} \times \mathbf{p}) \cdot \boldsymbol{\sigma}, \tag{4.6}$$

which has the feature of locking spin perpendicular to momentum–an emblematic feature of topological insulators! Though the Rashba term is only a small correction in normal semiconductors, the TI surface state Hamiltonian is a Dirac term with $\frac{\alpha_R}{\hbar}$ being replaced by the fermi velocity v_F, indicating much stronger spin-orbit coupling[207].

4.1.2 Consequences of Spin-Orbit Coupling

Spin-orbit coupling (and the corresponding Rashba field) are what allow for the rich interplay between spin and charge current[208].

4.1.2.1 Spin Precession and Spin Relaxation

If a spin is not parallel to the Rashba field, then the spin will precess. In the diffusive limit, this precession is responsible for one type of spin relaxation: the Dyakonov-Pearl effect[209] (the other major spin relaxation mechanism, the Elliott-Yafet mechanism[210,211], is caused by interactions with phonons and impurities in the presence of spin-orbit induced band mixing). The precession rate can be tuned by a gate voltage, since a gate voltage affects

the interfacial potential[212]. The control of precession (and therefore the information stored in the spin) via a gate voltage is a fundamental plausibility argument for the development of spintronics as a field. The Dyakonov-Perel mechanism will generally have a spin relaxation time that is inversely proportional to the momentum relaxation time ($\tau_s \propto \tau_p^{-1}$)[213], while the Eliot-Yafet mechanism–being analogous to scattering in the Drude model–has a nearly proportionality between spin and momentum scattering time[214]. The unwanted relaxation of spin information in carriers is a fundamental obstacle. It has been predicted[215] and experimentally confirmed[216] that under certain artificial conditions, where the Rashba field is offset by another spin-orbit effect, the spin relaxation mechanisms are suppressed to produce persistent spin currents.

4.1.2.2 Spin Hall and Inverse Spin Hall Effects

The spin Hall effect is a relatively recent[217] riff on the anomalous Hall effect (where a magnetized material will produce a Hall voltage with zero applied magnetic field[218]), and describes the conversion of an electrical current into a pure spin current (or vice-versa, for the inverse spin Hall effect), and can be achieved through two mechanisms. The extrinsic spin Hall effect comes from spin-orbit coupled impurities[219] and the intrinsic spin Hall effect arises from the interaction of spin-orbit coupling and the carriers[220,221]: the Rashba field adjusts the group velocity by a quantity known as the anomalous velocity[222]:

$$\mathbf{v}_a = \frac{\partial \hat{H}_R}{\partial p} = -\frac{\alpha_R}{\hbar}\mathbf{z} \times \boldsymbol{\sigma}. \tag{4.7}$$

This quantity is antisymmetric with the spin polarization, so carriers with opposite spins will be deflected in opposite directions. This is the spin Hall effect! Of course, there also exists an inverse Hall effect, where a spin current produces an electrical current[223].

This is also where there exists a deep connection between the physics of the Rashba field and the physics of the Dirac cone: the anomalous velocity correction (eq. 4.7) is

produced by the Berry curvature, which is a quantity that solely depends on the material's band structure[224]:

$$\Omega(\mathbf{p}) = \alpha_R \nabla \times (\boldsymbol{\sigma} \times \mathbf{p}). \tag{4.8}$$

Although the origin of the anomalous velocity in spin Hall insulators (Rashba field) is separate from the mechanism in topological insulators (Chern number), both systems can give identical experimental observations. Because of this connection, it follows that spin Hall effects do not necessarily require a Rashba field and therefore do not necessarily require broken inversion symmetry.

The spin Hall effect was first observed in semiconducting wells in 2004[225] via Kerr rotation measurements. The inverse spin Hall effect was observed much earlier: it was predicted to be measurable via optical spin orientation (to be discussed later in this chapter) by Averkiev and Dyakonov in 1983[226], and then experimentally verified a year later[227]. Most recent studies have focused on searching for materials with a large spin Hall angle, which is a dimensionless parameter used to quantify the efficiency of the charge-spin current conversion[228]:

$$\theta_{SH} = \frac{||J_s||}{||J_e||}. \tag{4.9}$$

Measurements of spin Hall angles are far from standard: platinum, a prototypical simple material with a relatively large spin Hall angle, has had measured values that range from $\theta_{SH} = 0.37^\circ$ [223] to $\theta_{SH} = 37.8^\circ$ [229].

Along with other topological materials, bismuth selenide has proven to be a fruitful medium for spin Hall experiments through both transport[162,163,230,231] and optical methods[232–236].

4.2 Optical Methods for Probing Spin Physics in Intrinsic Bismuth Selenide

Optical methods are a convenient way of preparing a population of polarized spins for studying the inverse spin Hall effect, but optical methods in general can be very ambigu-

ous. While DC photocurrent measurements can have their issues with providing ambiguous information (discerning between thermoelectric effect versus photovoltaic effect generated photocurrent is notoriously tricky[237]), attributing helicity-dependent results to a single mechanism is far more difficult and relies on symmetry analysis.

4.2.1 The Optical Zoo

The most general microscopic description of photocurrent density takes the form of a sum of contributions[238]:

$$j = \sum_n j_n \tag{4.10}$$

$$= -\frac{e}{\hbar} \sum_n \int_0^{k_{BZ}} \left[\rho_n(+k) - \rho_n(-k)\right] \frac{\partial \mathcal{E}_n}{\partial k} dk, \tag{4.11}$$

where the electron density ($\rho(\pm k)$) is integrated over the entire Brillouin zone. Material dependent selection rules will forbid certain transitions, which allows for an enormous variety of named photoresponses. These named photoresponses are probes of symmetry and symmetry breaking: group theory is extremely successful at describing and categorizing them[239], and a wide variety of orthogonal control measurements are required to differentiate them[240]. Different flavors of photoresponse in topological materials include:

1. The **thermoelectric effect** and **photovoltaic effect** are both present in our intrinsic bismuth selenide samples at room and cryogenic temperatures respectively[52]

2. **Linear photogalvanic effect (LPGE)**: second-order nonlinear process in which charge transport from excitation of valence to conduction band from linearly polarized light[241]

3. **Circular photogalvanic effect (CPGE)**: second-order nonlinear process in which asymmetric distribution of charge carriers in momentum-space from circularly polarized light; can be spatially dispersive[242], or even quantized[243]

4. **Photon drag effect**: linear process in which momentum transfer from incident photons to electrons near surface [244]

5. **Photodember effect**: linear process in which difference in electron and hole mobilities cause charge separation and lead to Dember field that generates drift-diffusion photocurrent [245]

6. **Ballistic current**: bulk photovoltaic (third order) process in which an asymmetry in band populations, $f_{n,\mathbf{k}} \neq f_{n,-\mathbf{k}}$ (where f_n is the momentum distribution in the nth band) causes a net photocurrent from off-diagonal elements in the electron distribution matrix [246,247].

7. **Shift current**: bulk photovoltaic (third order) process that is related to off-diagonal elements in the electron distribution matrix, but has the added complication that optical transitions have a momentum shift in the unit cell based on the Berry connection of the crystal (and therefore requires inversion symmetry) [239,247]

8. **Jerk current**: bulk photovoltaic (third order) process which is related to both hydrodynamic carrier acceleration and intensity-modified injection rates. It may be surprising to learn that jerk current was only first predicted in 2018 [248], and does not have a consensus of the microscopic origin [249].

Fundamental research in identifying photocurrent-generating mechanisms is still a vibrant research field, and the above list is *only* a subset of these photocurrent contributors [240]! We'll restrict our discussion to helicity-dependent measurements for the rest of the chapter.

4.2.2 The Case for Helicity Dependence and Spin Physics

Some materials may exhibit a helicity dependence on their photocurrent response. This is usually referred to as a circular photogalvanic effect, which we can separate a priori

from photogalvanic effects due to linearly or randomly polarized light: following Hosur's approach[250], the photocurrent response to an applied electric field, $\vec{E}$, is given by

$$j_\alpha = \eta_{\alpha\beta\gamma} E_\beta E_\gamma^*. \tag{4.12}$$

which says that the measured current density is given by the square of the incident electric field, up to a third rank tensor that only has nonzero entries for non-centrosymmetric systems. The tensor can be factored into a symmetric tensor and antisymmetric psuedotensor, $S_{\alpha\beta\gamma}$ and $A_{\alpha\mu}$, to rewrite the current density as

$$j_\alpha = \left(\frac{E_\beta(\omega) E_\gamma^*(\omega) + E_\beta^*(\omega) E_\gamma(\omega)}{2} \right) + i A_{\alpha\mu} \left(\vec{E} \times \vec{E}^* \right)_\mu, \tag{4.13}$$

Because circularly polarized light is antisymmetric under mirror reflections, the term attached to S vanishes and so we observe a current density that only depends on A. Therefore, circularly polarized light probes the circular photogalvanic response in a material. It is important to recognize that this only applies in systems with broken reflection symmetry–these can be normal incidence measurements with an external magnetic field or applied uniaxial strain, or for simply oblique angle systems.

The antisymmetric tensor abstractly parameterizes helicity dependant photocurrent responses, which generally come from three contributions in Bi_2Se_3: the inverse spin Hall effect (ISHE), which is generated via bulk state excitations; Rashba splitting in the trivial 2-dimensional electron gas (2-DEG); and spin-momentum locked topological surface states[251]– thus drawing a deep connection between helical radiation and spin physics.

4.2.3 Experimental Probes of Helicity Dependence in Intrinsic Bismuth Selenide

Theoretical work supports the concept that excitons formed at the Dirac cone should be spin-polarized triplet states[73]. We can extend the SPCM set-up (schematically depicted

in fig) to include controls for polarization dependence, by the inclusion of quarter waveplate (QWP) or photoelastic modulator (PEM); and angle dependence, by tilting the cryostat within the beam path. Since circularly polarized photons carry angular momenta, it is possible to generate a spin-polarized population of charge carriers via optical excitation.

4.2.4 Spin Generation and Diffusion

Topological materials present both an immense challenge and special opportunity in applications for spintronic devices since they are gapped and spin degenerate in the bulk, but gapless and spin-polarized on the TSSs[252]. Unlike graphene, which has a similar Hamiltonian, TIs have very large spin-orbit coupling. This means that while spin diffusion lengths are usually short in topological materials, they are fantastic spin generators and detectors[207]. Optical methods are convenient for studying spin physics because they do not rely on complex magnetic contacts for spin injection, which are difficult to implement[253,254].

Previous optical orientation experiments on stoichiometric Bismuth Selenide have produced results consistent with spin-momentum locking at low temperatures[205], but our efforts to study spin-polarized excitonic transport are novel may confirm the spontaneous in-plane magnetization predicted by Wang et al.[73].

4.2.5 Optical Orientation and Photocurrent Response Phenomenology

In our experiment, we use a combination of a linear polarizer and either a QWP or PEM to dynamically regulate the polarization of light incident on the MOSFET device (fig. 2b). As the QWP rotates, it modulates the polarization of light between p, s, and left and right circular polarizations of light; this depends on the angle α between the linear polarizer and the fast axis of the QWP. Since circular polarizations of light carry angular momenta, we can generate spin-polarized carriers in our device via optical orientation[213]. This measurement schematic is shown in figure 4.1. Due to spin-momentum locking in the TSSs, we see a change in the photocurrent as a function of polarization. There are other mechanisms

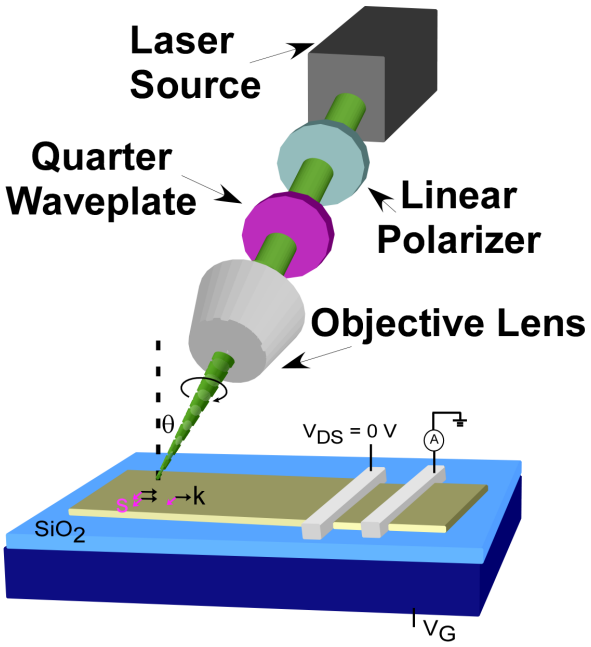

Figure 4.1: Schematic showing set up for production of helical radiation and study of helicity-dependent photoresponse. The linear polarizer ensures a well-defined reference angle with regard to the fast axis of the QWP. The rotation of the QWP determines the polarization of the radiation, and is rotated with a servo motor.

at play, and the helicity-dependant photocurrent in an oblique angle measurement can be phenomenologically described by

$$j(\alpha) = C \sin 2\alpha + L_1 \sin 4\alpha + L_2 \cos 4\alpha + D, \tag{4.14}$$

where the C term describes contributions from the circular photogalvanic effect, L_1 from the linear photogalvanic effect, L_2 from the trivial absorption modulation arising from the Fresnel equations, and D from polarization independent photocurrent effects (which be thermoeletric or photovoltaic in nature). It's worth discussing each of these terms, and how they fit into our studies:

The L_2 is the result of absorption modulation that is predicted by the Fresnel equations. As we rotate the QWP, we modulate the polarization of the laser between both linear polarizations–this corresponds to switching between s and p polarizations of the laser. The modulation of the magnitude of photocurrent in the s and p polarizations is in good agreement with the Fresnel equations, which makes this modulation trivial.

The D term corresponds to a constant background photocurrent. Canonically, previous studies on stoichiometric bismuth selenide did not observe appreciable photocurrents

when the laser is focused in the middle of the channel[205], and so they only attribute thermoelectric effects to contributions to D. Intrinsic bismuth selenide produces a large photocurrent, which means that our background is considerably larger than previous studies.

The L_1 term is ascribed to the linear photogalvanic response. While this photocurrent mechanism is expected to be topological in nature[53], in which states can be excited from the unoccupied to occupied parts of the Dirac cone. The photon drag effect, which describes a current generated by momentum transfer from photons to free carriers, may sometimes contribute to this term. Neither the linear photogalvanic effect nor photon drag require spin orientation[255].

The C describes the circular photogalvanic response term, which follows from the principle of spin momentum locking present in the Hamiltonian that governs the TSSs. Our nonlocal circular photogalvanic response is generally smaller than the other terms in our experiments, following other experiments on local photocurrents[256].

The lack of a polarization dependence at normal incidence in our previous studies is consistent with both the Fresnel equations (which predict vanishing photocurrent modulation at normal incidence) and principals of optical orientation in the TSSs (which require an in plane component of angular momentum).

4.2.5.1 Oblique Angle Photocurrent Results

A major accomplishment of our research group is our ability to extract the helicity-dependent photo response of a material from a series of DC photocurrent scans. A normal DC photocurrent scan results in a 200x200 pixel image, where each pixel contains information about the magnitude of the photocurrent (fig. 1.d shows a typical DC photocurrent response). By collecting a sequence of scans where we rotate a QWP relative to a linear polarizer, we can extract a line graph that shows how the total photocurrent response changes as a function of QWP angle *at every single point*. We can then politely ask our computer to fit our truncated Fourier series to this plot, extract the value of the C term, and then

plot this C term in a 2D plot to obtain a map of the CPGE response in any device. This computer-aided fitting is robust and can be applied to a wide range of materials.

The results for Bi_2Se_3 are discouraging for all experimentally available wavelengths (which range from 500 nm to 1700 nm). The fitting for C is 0.003% of the steady-state photocurrent, and the uncertainty in fitting is *ten times* larger than the value itself. The optical transitions that produce this signal are dominated by bulk-to-bulk transitions that eventually relax to the Dirac cone. The spin lifetimes are dramatically shorter in the bulk (1 ps[162]) compared to the Dirac cone (1 ns[236]): the overwhelming majority of carriers that are collected at an electrode have random spin information and thus are not constrained by modulation via spin-momentum locking.

4.2.6 Challenges with Helicity Dependent Measurements

Helicity-dependent measurements are very challenging. Some of these challenges are present in all helicity-dependent experiments, but some are endemic to intrinsic Bi_2Se_3.

4.2.6.1 Generic Challenges

Helicity-dependent measurements on a nano-scale device are generically made difficult by beam precession. QWPs are, obviously, real experimental objects. Achromatic and super achromatic quarter waveplates (which are convenient because they allow for wavelength-dependent studies) are manufactured by gluing together two half waveplates with air space in between[257], and thus will generally feature a small wedge angle–ThorLabs generally cites a beam deviation of fewer than 10 arcseconds to be acceptable for sale. As the QWP rotates, the beam will then precess with a radius equal to the beam deviation. A beam path of 20 mm (for an unrealistically compact set-up) will deviate the beam by nearly 1μm, which is a huge problem in devices that are several microns wide. This can be mitigated somewhat by defocusing the beam, which reduces the power fluctuation. Using single-wavelength zero-order QWPs can reduce the precession as well, because this element is comprised of a single

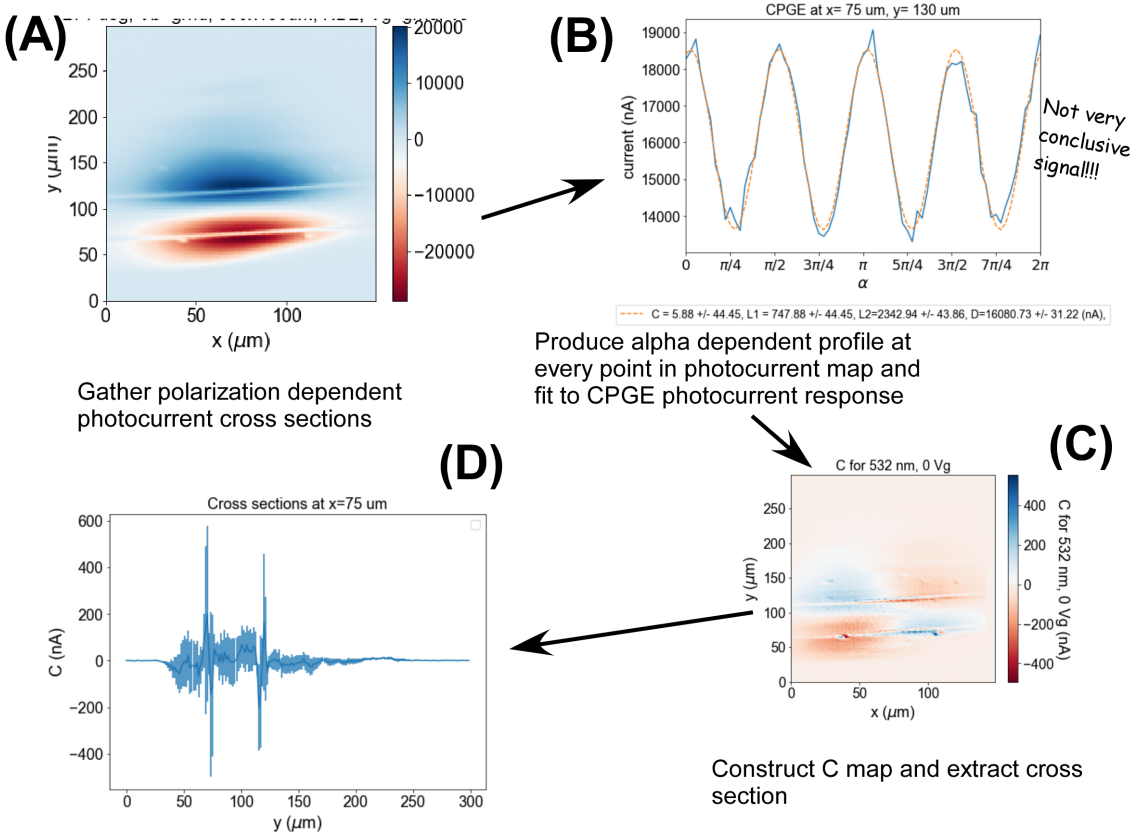

Figure 4.2: Experimental algorithm for producing a helicity-dependent photocurrent map. (A) a standard SPCM map is produced for many different values QWP rotation angle. (B) After correcting for cryostat drift, the magnitude of the photoresponse is tabulated at every point and plotted as a function of QWP angle. (C) Each helicity plot is then fit with equation 4.14, which extracts the helical and steady-state components of the signal. The fitting information at each pixel can then be used to produce a map of C, or any other parameter. (D) Cross-sections of C can be taken to determine spin diffusion length.

optical element and thus tends to have smaller wedge angles. Optical alignment is also critical to suppress the beam precession.

4.2.6.2 Large Helicity-independent Photocurrent Background

As briefly discussed, another challenges comes from the large helicity-independent photocurrent background (D) originated from the nonlocal photocurrent in our intrinsic devices. Large D means large L_2 (Fresnel modulation of the photocurrent). If C is much smaller than L_2, it is practically difficult to clearly extract C. One way to mitigate is to reduce L_2 by choosing wavelength and incident angle, which we discuss below.

The Fresnel equations, whose contribution is present in equation 4.14, capture the steady-state's contribution. Assuming the photocurrent is linear with the transmitted light, the ratio of L_2 and D can be found to be,

$$\frac{L_2}{D} = \frac{t_s^2 - t_p^2}{3t_s + t_p},$$

where

$$t_s = \frac{2\cos\theta_i}{\cos\theta_i + n_s\cos\theta_t} \tag{4.15}$$

$$t_p = \frac{2\cos\theta_i}{n_s\cos\theta_i + \cos\theta_t}. \tag{4.16}$$

Here, n_s is the (wavelength-dependent) index of refraction of the material, and θ_i (θ_t) is the angle of incidence (transmission or refraction) of the radiation. This relationship monotonically increases when θ_i increases and n_s decreases. Larger incident angles will provide a larger in-plane momentum component, so this relationship has a very intuitive geometric picture. The relationship with the index of refraction is less obvious and bears caution, since this result is purely classical and ignores potential band corrections.

Another possible way to mitigate the effect is to focus the laser in the middle of the channel where the D is close to zero. Such a method has been used before in ref.[205].

However, this method limits the HDPC study of the nonlocal photocurrent, as we would like to study other locations, especially outside the channel. One can also play with the gate and laser intensity to reduce the nonlocal photocurrent background. Mid-IR laser may help reduce the background and increase the HDPC signal because it suppresses the optical transition between bulk states.

4.3 Modeling the Inverse Spin Hall Effect

The modeling work presented in this section was mainly carried out by Kuen Wai (Edward) Tang reported in ref[258], which I co-authored. I made contributions by providing experimental comparisons and participating in discussions.

To help understand the helicity-dependent photocurrent mapping results, we performed finite element simulations with COMSOL[259] to study the photoinduced spin Hall effect (PISHE) at normal incidence in a MOSFET. This simulation is based on the continuity equation for electrons and holes:

$$\frac{dn_\lambda}{dt} = G_\lambda - b\left(n_\lambda p - \frac{n_i^2}{2}\right) - \frac{n_\lambda - n_{-\lambda}}{2\tau_s} - \nabla \cdot \mathbf{J}_{n_\lambda}, \tag{4.17}$$

where λ parameterizes spin polarization ($\lambda = 1$ for spin up, $\lambda = -1$ for spin down), τ_s is spin relaxation time, b is the parameter for Shockley-Reade-Hall recombination, G is the photogeneration rate, and n_i is the intrinsic carrier concentration. It is assumed that hole recombination is sufficiently fast to be ignorable. Left circularly polarized light will generate spin-up carriers, and right circularly polarized light will generate spin-down carriers. In the steady state, which is the condition under which most PISHE experiments are performed, all quantities will be time-independent, and the left-hand side of eq. 4.17 will vanish. The number current density is comprised of the usual drift-diffusion terms, as well as an inverse spin Hall term:

$$\mathbf{J}_{n_\lambda} = -\mu_n n_\lambda \mathbf{E} - D_n \nabla_n n_\lambda + \mathbf{J}_{n_\lambda}^{ISHE}, \tag{4.18}$$

where the mobility μ_n and diffusion constant D_n are assumed to be spin independent. The number current density is related to the charge current density by $\mathbf{J}_\lambda = q\mathbf{J}_{n_\lambda}$. The explicit form for the inverse spin Hall current contribution is

$$\mathbf{J}_{n_\lambda}^{ISHE} = \lambda\gamma\left(\mu_n n_\lambda \mathbf{E} + D_n \nabla n_\lambda\right) \times \hat{\mathbf{z}}, \tag{4.19}$$

wher γ is a number that parameterizes the spin-orbit strength and $\hat{\mathbf{z}}$ is the unit vector normal to the surface of the material. The simulation results (summarized in fig. 4.3) show a 2D device with metal contacts where recombination and spin relaxation are assumed to be instantaneous. Additionally, the temperature is fixed at $T = 300$K, a barrier potential (which gives band bending) at the contacts is set to Φ_B, and the applied bias is set to $V = 0$ for all simulations.

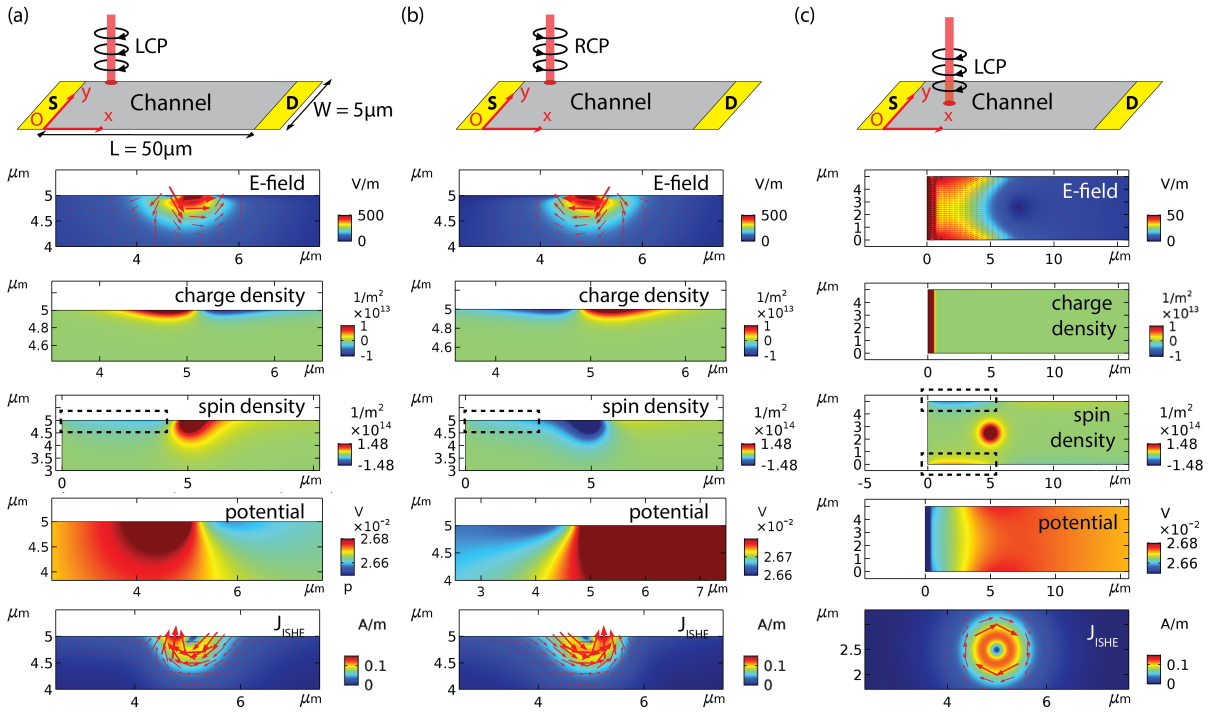

Figure 4.3: The first row shows different configurations for a : (a) and (b) are performed at the edge of the device, and (c) is performed at the middle of the channel. (a) and (c) are LCP, and (b) is RCP. S and D are source and drain electrodes. Red arrows show vector directions. Dashed boxes show spin accumulation. The rows below show simulated electric field, charge density, spin density, electric potential, and ISHE current respectively.

4.3.1 Features of Electric Field, Charge, and Spin Distributions

If a circularly polarized laser is focused near the edge, an electric field with curl develops (red arrows on fig. 4.3). Charges of opposite sign will form on either side of this curl, which generate an in-channel emf and thus will drive a current. This current switches direction when circular polarization is switched, so this is helicity-dependent photocurrent (HDPC)! This current is much weaker when $\gamma = 0$, highlighting the essential nature of spin-orbit coupling for PISHE. If the light is moved inside the channel, then there exists no edge to break the symmetry of the induced electric field and so no dipole will form. Without a dipole (e.g. the laser is focused away from an edge), there can be no induced local electromagnetic force and no current will flow: this has been previously observed[260]. The boxes in figure 4.3 show long-range accumulation of spin–this is PISHE independent, since spin up (down) carriers accumulate at the top (bottom) of the device, regardless of photon polarization; it is consistent with spin accumulation from a transverse spin current via the spin Hall effect. This spin quantity is much smaller than the spin population injected by the laser, and is probably an ignorable contribution in a real experiment.

4.3.2 Impact on Photocurrent Mapping

We define $I_{HDPC} = I_{\uparrow} - I_{\downarrow}$ and $I_{sum} = I_{\uparrow} + I_{\downarrow}$. Generating photocurrent maps with this simulation package shows that I_{sum} decreases when the laser approaches the edge of the sample, as the laser spot size incrementally moves off the sample (fig. 4.4a). However, this is where I_{HDPC} is largest since it relies on the dipole formation that only occurs at the material edge, and flips sign when moved from one edge to another (fig. 4.4b). If the laser is moved away from a contact (fig. 4.4c), I_{sum} decreases (on a length scale consistent with its minority carrier diffusion length), while I_{HDPC} is constant (because in-channel emf is position independent).

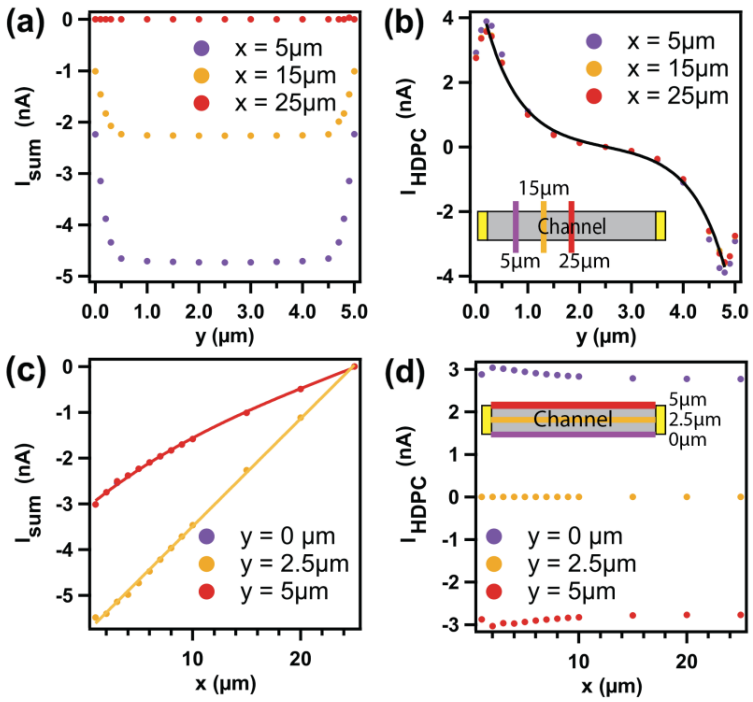

Figure 4.4: Photocurrent profiles. (a) I_{sum} as function of vertical position, showing rapid decay near edges; (b) I_{HDPC} as a function of vertical position, showing maximum magnitude near edge and sign flip; (c) I_{sum} as a function of horizontal position, showing decay profile; (d) I_{HDPC} as a function of horizontal position, showing relatively constant magnitude.

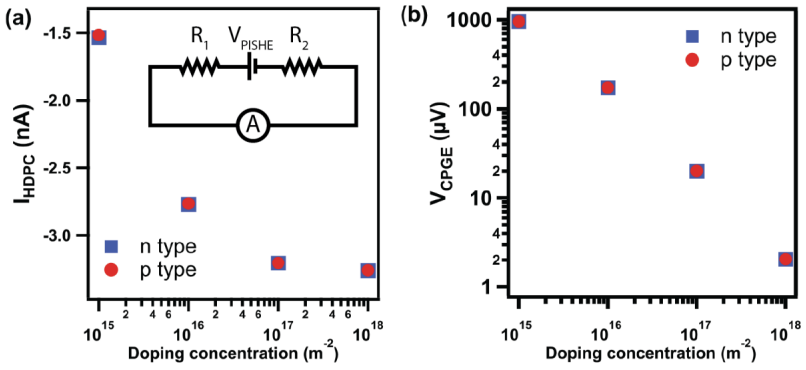

Figure 4.5: Doping effects on HDPC. Doping effects remain uniform for n or p type devices. (a) increasing the doping concentration causes the magnitude of HDPC to increase up to a saturation value. (b) increasing the doping concentration causes the emf driven by PISHE to increase nearly linearly.

4.3.3 Doping Effects

To study doping dependence, the barrier height is changed so that band bending is flat at the contact and τ_s is held constant. Varying the doping concentration by three decades (fig. 4.5) shows that the helicity-dependent photocurrent only changes by roughly a factor of 3 and is ignorant of carrier type. This current can be modeled as an emf that drives a current through the channel with resistance $R_{total} = R_1 + R_2$ (fig. 4.5 inset) where $V_{PISHE} = I_{PISHE}R_{total}$: V_{PISHE} is inversely proportional to doping, also ignorant of carrier type. Previous studies have observed weaker PISHE at higher doping which was attributed to a decreased τ_s.

4.3.4 Band Bending Effects

Band bending will occur at metal-semiconductor junctions, which is especially a challenge with magnetic contacts[261]. If Φ_B is increased, the total measured current will increase because of more efficient charge separation (fig. 4.6a); the magnitude of I_{HDPC} will decrease from the increased contact resistance (fig. 4.6b and c), which can be estimated as the low

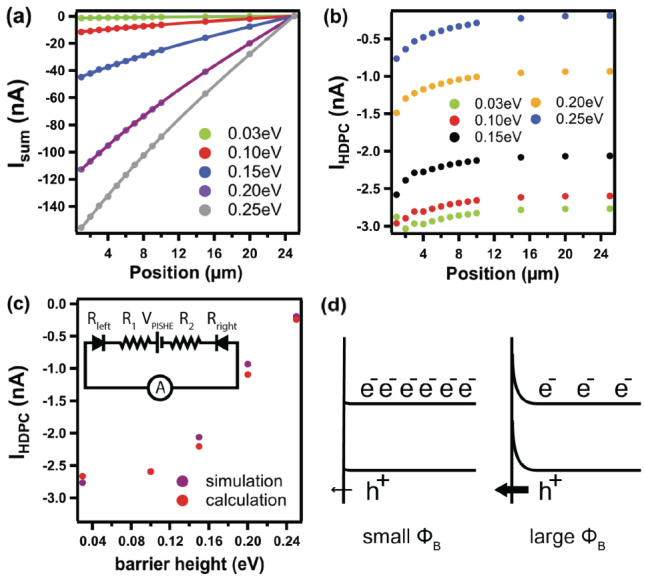

Figure 4.6: Band bending effects on PISHE. (a) and (b) show I_{sum} and I_{HDPC} respectively for various energy barriers. (d) larger band bending causes more efficient charge separation and reduces charge buildup near the contact.

bias limit for a diode[262]:

$$R_{contact} = 2\frac{k_B T}{qWA_{2D}T^{3/2}} \exp \frac{q\Phi_B}{k_B T}, \tag{4.20}$$

where A_{2D} is the 2D Richardson constant for thermionic emission[263], and the prefactor of 2 accounts for the fact that there are two contacts contributing to contact resistance.

4.3.5 Spin Relaxation Effects

The spin lifetime was varied between $\tau_s = 0.1$ns to $\tau_s = 100$ns. The magnitude of I_{HDPC} increases and saturates around 10ns (fig. 4.7b): the increased spin density enhances the dipole charge accumulation, but when τ_s approaches the Shockley-Read-Hall recombination lifetime, the carrier recombination will being to bottleneck the spin density. The magnitude of I_{HDPC} quickly decreases near the contact when τ_s is large–because spin relaxation is assumed to be instantaneous inside the contact, the contact will act like a spin sink that falls off like the spin diffusion length. The astute committee member will notice that

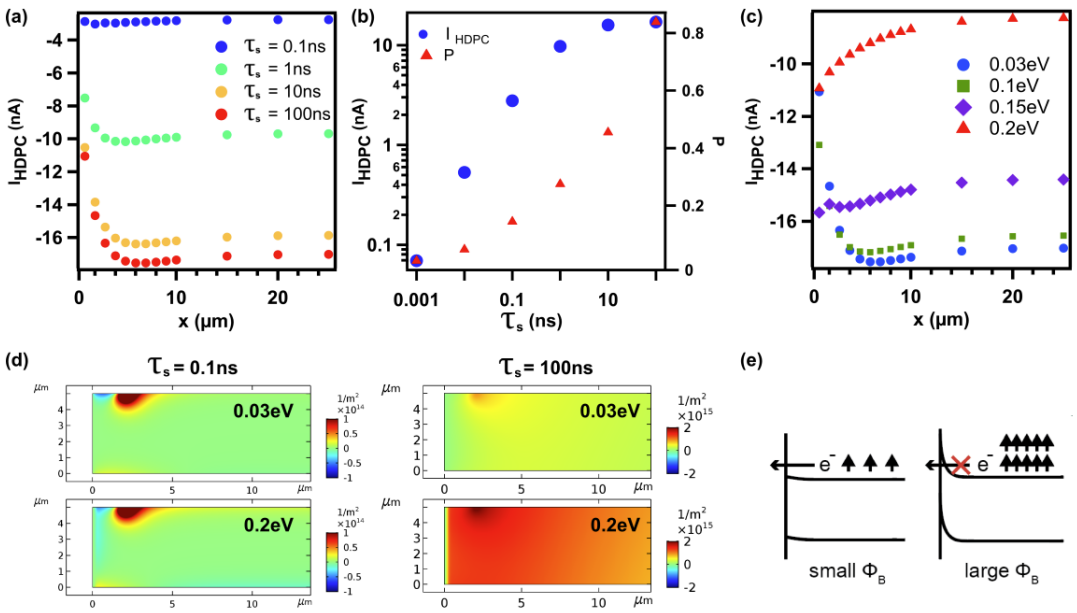

Figure 4.7: Spin relaxation effects on PISHE. (a) I_{HDPC} as a function of position and spin lifetime, (b) spin lifetime, and (c) position and band bending. (d) Spin density as a function of position and band bending, with diagram (e) showing spin accumulation due to electron blocking of higher barrier–conceptually different from figure 4.6e.

I_{HDPC} *increases* near the contact in figure 4.7a, but *decreases* near the contact in figure 4.6b! This paradox is resolved by considering the dueling mechanisms that are important near the contact: increased carrier recombination (which reduces carrier density and increases HDPC) and increased spin relaxation (which reduces spin density and reduces HDPC).

4.4 Outlook for Future Work

The Yu lab has mastered helicity-dependent photocurrent studies, producing interesting results for cadmium arsenide[264]. The primary issue at hand is that the DC photocurrent response is enormous for intrinsic Bi_2Se_3. The experimental fact that made the steady-state measurement so successful, is a terrible pain for helicity-dependent signals. Mid-IR excitation sources could potentially alleviate this steady-state saturation and also shed light on the surface states.

Chapter 5

Concluding Remarks and Hints for the Future

The work in this dissertation is compiled from a body of work that includes several publications:

1. Wang, Bob Minyu, Yuqing Zhu, Henry Clark Travaglini, Renzhi Sun, Sergey Y. Savrasov, William Hahn, Klaus van Benthem, and Dong Yu. "Spatially dispersive helicity-dependent photocurrent in Dirac semimetal Cd 3 As 2 nanobelts." Physical Review B 108, no. 16 (2023): 165405.

2. McClintock, Luke, Ziyi Song, H. Clark Travaglini, R. Tugrul Senger, Vigneshwaran Chandrasekaran, Han Htoon, Dmitry Yarotski, and Dong Yu. "Highly mobile excitons in single crystal methylammonium lead tribromide perovskite microribbons." The Journal of Physical Chemistry Letters 13, no. 16 (2022): 3698-3705.

3. Tang, Kuen Wai, Bob Minyu Wang, Henry Clark Travaglini, and Dong Yu. "Modeling of the photocurrent induced by inverse spin Hall effect under local circularly polarized photoexcitation." Physical Review B 104, no. 20 (2021): 205413.

4. McClintock, Luke, Rui Xiao, Yasen Hou, Clinton Gibson, Henry Clark Travaglini, David Abramovitch, Liang Z. Tan et al. "Temperature and gate dependence of carrier diffusion in single crystal methylammonium lead iodide perovskite microstructures." The Journal of Physical Chemistry Letters 11, no. 3 (2020): 1000-1006.

5. Hou, Yasen, Rui Wang, Rui Xiao, Luke McClintock, Henry Clark Travaglini, John Paulus Francia, Harry Fetsch et al. "Millimetre-long transport of photogenerated carriers in topological insulators." Nature communications 10, no. 1 (2019): 5723.

6. Cadden-Zimansky, Paul, M. Shinn, G. T. Myers, Y. Chu, M. J. Dalrymple, and H. C. Travaglini. "Formation of the n= 0 Landau level in hybrid graphene." Journal of Physics Communications 2, no. 5 (2018): 051001.

7. Peng, Xingyue, Yiming Yang, Yasen Hou, Henry C. Travaglini, Luke Hellwig, Sahar Hihath, Klaus van Benthem, Kathleen Lee, Weifeng Liu, and Dong Yu. "Efficient and hysteresis-free field effect modulation of ambipolarly doped vanadium dioxide nanowires." Physical Review Applied 5, no. 5 (2016): 054008.

Which demonstrates a broad range of experience in semiconductor characterization techniques. In addition to the focus on TIs, I am also proud of my contributions to fabrication technology and device architecture that has been important for other aspects of the Yu lab research program. I have also done interesting work on other materials such as WTe_2 (which, in a twist of fate, was scooped by another group[265]) and colloidal quantum dot superlattice MOSFETs (which, in a not-entirely-different-feeling twist of fate, belongs to the field that was awarded the 2023 Nobel prize in chemistry[266]).

Intrinsic bismuth selenide is a material that, under certain mercurial conditions, can show transport qualities that are both obviously dramatic and intellectually interesting. We have presented novel studies of intrinsic bismuth selenide through methods beyond the

steady-state photocurrent measurement. Ultrafast optical measurements have shown that the extremely efficient transport can be locally suppressed via carrier injection with a pulsed laser and that the associated recovery time is *longer* for larger fluences. Magnetotransport measurements have suggested that injected carriers do not contribute to weak antilocalization properties. Helicity-dependent photocurrent measurements are likely to only be feasible with a mid-infrared laser, although simulation work suggests that the strong spin-orbit coupling should produce an observable signal. In addition to the helicity-dependent experiment, a mid-infrared laser could provide great insights into the steady state and ultrafast regimes.

Technological development, from the flint axe to the Josephson junction, is an important part of human progress. But it is also volatile. Many challenges remain before intrinsic bismuth selenide can be fully understood, which fall under both practical and theoretical considerations: why are VLSCVD methods more successful than MBE for growing antimony-compensated bismuth selenide crystals? Why haven't other research groups already reported this behavior? Can these delocalized carriers be directly dissociated with a split gate MOSFET geometry? If so, then why doesn't the depletion region on a floating electrode destroy them?

Bismuth selenide is a small leaf on the branch of quantum materials, which is in turn a small component of the tree of nature. If this dissertation should contain useful information for future travelers, it is because it was built on the shoulders of giants and mortals alike.

References

[1] Christopher Triola, Anna Pertsova, Robert S Markiewicz, and Alexander V Balatsky. Excitonic gap formation in pumped dirac materials. *Physical Review B*, 95(20):205410, 2017.

[2] Chris A Mack. Fifty years of moore's law. *IEEE Transactions on semiconductor manufacturing*, 24(2):202–207, 2011.

[3] Frederik Hetsch, Ni Zhao, Stephen V Kershaw, and Andrey L Rogach. Quantum dot field effect transistors. *Materials Today*, 16(9):312–325, 2013.

[4] Lei Zhuang, Lingjie Guo, and Stephen Y Chou. Silicon single-electron quantum-dot transistor switch operating at room temperature. *Applied Physics Letters*, 72(10):1205–1207, 1998.

[5] Effendi Leobandung, Lingjie Guo, Yun Wang, and Stephen Y Chou. Observation of quantum effects and coulomb blockade in silicon quantum-dot transistors at temperatures over 100 k. *Applied physics letters*, 67(7):938–940, 1995.

[6] Anindya Das, Simone Pisana, Biswanath Chakraborty, Stefano Piscanec, Srijan K Saha, Umesh V Waghmare, Konstantin S Novoselov, Hulikal R Krishnamurthy, Andre K Geim, Andrea C Ferrari, et al. Monitoring dopants by raman scattering in an electrochemically top-gated graphene transistor. *Nature nanotechnology*, 3(4):210–215, 2008.

[7] Roman Sordan, Floriano Traversi, and Valeria Russo. Logic gates with a single graphene transistor. *Applied Physics Letters*, 94(7):51, 2009.

[8] Fengnian Xia, Thomas Mueller, Roksana Golizadeh-Mojarad, Marcus Freitag, Yu-ming Lin, James Tsang, Vasili Perebeinos, and Phaedon Avouris. Photocurrent imaging and efficient photon detection in a graphene transistor. *Nano letters*, 9(3):1039–1044, 2009.

[9] Sungjae Cho, Nicholas P Butch, Johnpierre Paglione, and Michael S Fuhrer. Insulating behavior in ultrathin bismuth selenide field effect transistors. *Nano letters*, 11(5):1925–1927, 2011.

[10] Supriyo Datta and Biswajit Das. Electronic analog of the electro-optic modulator. *Applied Physics Letters*, 56(7):665–667, 1990.

[11] SA Wolf, DD Awschalom, RA Buhrman, JM Daughton, von S von Molnár, ML Roukes, A Yu Chtchelkanova, and DM Treger. Spintronics: a spin-based electronics vision for the future. *science*, 294(5546):1488–1495, 2001.

[12] Motohiko Ezawa. Spin valleytronics in silicene: Quantum spin hall–quantum anomalous hall insulators and single-valley semimetals. *Physical Review B*, 87(15):155415, 2013.

[13] John R Schaibley, Hongyi Yu, Genevieve Clark, Pasqual Rivera, Jason S Ross, Kyle L Seyler, Wang Yao, and Xiaodong Xu. Valleytronics in 2d materials. *Nature Reviews Materials*, 1(11):1–15, 2016.

[14] Ady Stern and Netanel H Lindner. Topological quantum computation—from basic concepts to first experiments. *Science*, 339(6124):1179–1184, 2013.

[15] Al Y Cho and JR Arthur. Molecular beam epitaxy. *Progress in solid state chemistry*, 10:157–191, 1975.

[16] Xi Chen, Xu-Cun Ma, Ke He, Jin-Feng Jia, and Qi-Kun Xue. Molecular beam epitaxial growth of topological insulators. *Advanced Materials*, 23(9):1162–1165, 2011.

[17] Yoshikazu Homma, Yoshiro Kobayashi, Toshio Ogino, Daisuke Takagi, Roichi Ito, Yung Joon Jung, and Pulickel M Ajayan. Role of transition metal catalysts in single-walled carbon nanotube growth in chemical vapor deposition. *The Journal of Physical Chemistry B*, 107(44):12161–12164, 2003.

[18] Yub Raj Sapkota and Dipanjan Mazumdar. Bulk transport properties of bismuth selenide thin films grown by magnetron sputtering approaching the two-dimensional limit. *Journal of Applied Physics*, 124(10), 2018.

[19] Gerd Binnig, Heinrich Rohrer, Ch Gerber, and Edmund Weibel. Surface studies by scanning tunneling microscopy. *Physical review letters*, 49(1):57, 1982.

[20] Zhanybek Alpichshev, JG Analytis, J-H Chu, Ian R Fisher, YL Chen, Zhi-Xun Shen, Alan Fang, and Aharon Kapitulnik. Stm imaging of electronic waves on the surface of bi 2 te 3: topologically protected surface states and hexagonal warping effects. *Physical review letters*, 104(1):016401, 2010.

[21] Jixia Dai, Damien West, Xueyun Wang, Yazhong Wang, Daniel Kwok, S-W Cheong, SB Zhang, and Weida Wu. Toward the intrinsic limit of the topological insulator bi 2 se 3. *Physical review letters*, 117(10):106401, 2016.

[22] IA Nechaev, RC Hatch, Marco Bianchi, D Guan, C Friedrich, I Aguilera, JL Mi, BB Iversen, S Blügel, Ph Hofmann, et al. Evidence for a direct band gap in the topological insulator bi 2 se 3 from theory and experiment. *Physical Review B*, 87(12):121111, 2013.

[23] David V Lang and Charles H Henry. Scanning photocurrent microscopy: A new technique to study inhomogeneously distributed recombination centers in semiconductors. *Solid-State Electronics*, 21(11-12):1519–1524, 1978.

[24] Rion Graham and Dong Yu. Scanning photocurrent microscopy in semiconductor nanostructures. *Modern Physics Letters B*, 27(25):1330018, 2013.

[25] Marc Lachieze-Rey and Jean-Pierre Luminet. Cosmic topology. *Physics Reports*, 254(3):135–214, 1995.

[26] Patrick Popescu-Pampu and Patrick Popescu-Pampu. The genus and the arithmetic of curves. *What is the Genus?*, pages 71–72, 2016.

[27] Edwin H Hall et al. On a new action of the magnet on electric currents. *American Journal of Mathematics*, 2(3):287–292, 1879.

[28] Robert Green. Hall effect measurements in materials characterization. *White paper*, 3111, 2011.

[29] RS Popović. Hall-effect devices. *Sensors and Actuators*, 17(1-2):39–53, 1989.

[30] Wikipedia. Hall effect — Wikipedia, the free encyclopedia. `http://en.wikipedia.org/w/index.php?title=Hall%20effect&oldid=1171156288`, 2023. [Online; accessed 31-August-2023].

[31] K v Klitzing, Gerhard Dorda, and Michael Pepper. New method for high-accuracy determination of the fine-structure constant based on quantized hall resistance. *Physical review letters*, 45(6):494, 1980.

[32] Horst Ludwig Stormer. Two-dimensional electron correlation in high magnetic fields. *Physica B: Condensed Matter*, 177(1-4):401–408, 1992.

[33] Steven M Girvin and Kun Yang. *Modern condensed matter physics*. Cambridge University Press, 2019.

[34] Daniel C Tsui, Horst L Stormer, and Arthur C Gossard. Two-dimensional magnetotransport in the extreme quantum limit. *Physical Review Letters*, 48(22):1559, 1982.

[35] Matthias Tarnowski, F Nur Ünal, Nick Fläschner, Benno S Rem, André Eckardt, Klaus Sengstock, and Christof Weitenberg. Measuring topology from dynamics by obtaining the chern number from a linking number. *Nature communications*, 10(1):1728, 2019.

[36] Emil Prodan. Robustness of the spin-chern number. *Physical Review B*, 80(12):125327, 2009.

[37] Liang Fu and Charles L Kane. Topological insulators with inversion symmetry. *Physical Review B*, 76(4):045302, 2007.

[38] Alexey A Soluyanov and David Vanderbilt. Computing topological invariants without inversion symmetry. *Physical Review B*, 83(23):235401, 2011.

[39] Ying-Ming Xie, Benjamin T Zhou, and Kam Tuen Law. Spin-orbit-parity-coupled superconductivity in topological monolayer wte 2. *Physical Review Letters*, 125(10):107001, 2020.

[40] M Jurczyszyn, M Sikora, M Chrobak, and L Jurczyszyn. Studies of surface states in bi2se3 induced by the bise substitution in the crystal subsurface structure. *Applied Surface Science*, 528:146978, 2020.

[41] Yuqi Xia, Dong Qian, David Hsieh, L Wray, Arijeet Pal, Hsin Lin, Arun Bansil, DHYS Grauer, Yew San Hor, Robert Joseph Cava, et al. Observation of a large-gap topological-insulator class with a single dirac cone on the surface. *Nature physics*, 5(6):398–402, 2009.

[42] Charles L Kane and Eugene J Mele. Quantum spin hall effect in graphene. *Physical review letters*, 95(22):226801, 2005.

[43] Adam L Gross, Yasen Hou, Antonio Rossi, Dong Yu, and Inna M Vishik. Nanosecond dynamics in intrinsic topological insulator bi 2- x sb x se 3 revealed by time-resolved optical reflectivity. *Physical Review B*, 103(2):L020301, 2021.

[44] Anthony Vargas, Susmita Basak, Fangze Liu, Baokai Wang, Eugen Panaitescu, Hsin Lin, Robert Markiewicz, Arun Bansil, and Swastik Kar. The changing colors of a quantum-confined topological insulator. *Acs Nano*, 8(2):1222–1230, 2014.

[45] Yi Zhang, Ke He, Cui-Zu Chang, Can-Li Song, Li-Li Wang, Xi Chen, Jin-Feng Jia, Zhong Fang, Xi Dai, Wen-Yu Shan, et al. Crossover of the three-dimensional topological insulator bi2se3 to the two-dimensional limit. *Nature Physics*, 6(8):584–588, 2010.

[46] Desheng Kong, Yulin Chen, Judy J Cha, Qianfan Zhang, James G Analytis, Keji Lai, Zhongkai Liu, Seung Sae Hong, Kristie J Koski, Sung-Kwan Mo, et al. Ambipolar field effect in the ternary topological insulator (bi x sb 1–x) 2 te 3 by composition tuning. *Nature nanotechnology*, 6(11):705–709, 2011.

[47] T Arakane, T Sato, S Souma, K Kosaka, K Nakayama, M Komatsu, T Takahashi, Zhi Ren, Kouji Segawa, and Yoichi Ando. Tunable dirac cone in the topological insulator bi 2-x sb x te 3-y se y. *Nature communications*, 3(1):1–5, 2012.

[48] Haijun Zhang, Chao-Xing Liu, Xiao-Liang Qi, Xi Dai, Zhong Fang, and Shou-Cheng Zhang. Topological insulators in bi2se3, bi2te3 and sb2te3 with a single dirac cone on the surface. *Nature physics*, 5(6):438–442, 2009.

[49] Yulin Chen, Desheng Kong, Judy Cha, Qianfan Zhang, James Analytis, Keji Lai, Zhongkai Liu, Seung-Sae Hong, Kristie Koski, Sung-Kwan Mo, et al. Ambipolar field effect in the ternary topological insulator (bi x sb 1-x) 2 te 3 by composition tuning. In *APS March Meeting Abstracts*, volume 2012, pages J31–012, 2012.

[50] Chee Huei Lee, Rui He, ZhenHua Wang, Richard LJ Qiu, Ajay Kumar, Conor Delaney, Ben Beck, TE Kidd, CC Chancey, R Mohan Sankaran, et al. Metal–insulator transition in variably doped (bi 1- x sb x) 2 se 3 nanosheets. *Nanoscale*, 5(10):4337–4343, 2013.

[51] Cheng Zhang, Xiang Yuan, Kai Wang, Zhi-Gang Chen, Baobao Cao, Weiyi Wang, Yanwen Liu, Jin Zou, and Faxian Xiu. Observations of a metal–insulator transition and strong surface states in bi2–xsbxse3 thin films. *Advanced materials*, 26(41):7110–7115, 2014.

[52] Yasen Hou, Rui Wang, Rui Xiao, Luke McClintock, Henry Clark Travaglini, John Paulus Francia, Harry Fetsch, Onur Erten, Sergey Y Savrasov, Baigeng Wang, et al. Millimetre-long transport of photogenerated carriers in topological insulators. *Nature communications*, 10(1):1–7, 2019.

[53] Ch Kastl, T Guan, XY He, KH Wu, YQ Li, and AW Holleitner. Local photocurrent generation in thin films of the topological insulator bi 2 se 3. *Applied Physics Letters*, 101(25):251110, 2012.

[54] Dong-Xia Qu, Xiaoyu Che, Xufeng Kou, Lei Pan, Jonathan Crowhurst, Michael R Armstrong, Jonathan Dubois, Kang L Wang, and George F Chapline. Anomalous helicity-dependent photocurrent in the topological insulator (bi 0.5 sb 0.5) 2 te 3 on a gaas substrate. *Physical Review B*, 97(4):045308, 2018.

[55] Luke McClintock, Ziyi Song, H Clark Travaglini, R Tugrul Senger, Vigneshwaran Chandrasekaran, Han Htoon, Dmitry Yarotski, and Dong Yu. Highly mobile excitons in single crystal methylammonium lead tribromide perovskite microribbons. *The Journal of Physical Chemistry Letters*, 13(16):3698–3705, 2022.

[56] Luke McClintock, Rui Xiao, Yasen Hou, Clinton Gibson, Henry Clark Travaglini, David Abramovitch, Liang Z Tan, Ramazan Tugrul Senger, Yongping Fu, Song Jin, et al. Temperature and gate dependence of carrier diffusion in single crystal methylammonium lead iodide perovskite microstructures. *The Journal of Physical Chemistry Letters*, 11(3):1000–1006, 2020.

[57] Xingyue Peng, Yiming Yang, Yasen Hou, Henry C Travaglini, Luke Hellwig, Sahar Hihath, Klaus van Benthem, Kathleen Lee, Weifeng Liu, and Dong Yu. Efficient and hysteresis-free field effect modulation of ambipolarly doped vanadium dioxide nanowires. *Physical Review Applied*, 5(5):054008, 2016.

[58] Sahng-Kyoon Jerng, Kisu Joo, Youngwook Kim, Sang-Moon Yoon, Jae Hong Lee, Miyoung Kim, Jun Sung Kim, Euijoon Yoon, Seung-Hyun Chun, and Yong Seung Kim.

Ordered growth of topological insulator bi 2 se 3 thin films on dielectric amorphous sio 2 by mbe. *Nanoscale*, 5(21):10618–10622, 2013.

[59] Zheng Ju, Yasen Hou, Andrew Bernard, Valentin Taufour, Dong Yu, and Susan M Kauzlarich. Ambipolar topological insulator and high carrier mobility in solution grown ultrathin nanoplates of sb-doped bi2se3. *ACS Applied Electronic Materials*, 1(9):1917–1923, 2019.

[60] Protyush Sahu, Jun-Yang Chen, Jason C Myers, and Jian-Ping Wang. Weak antilocalization and low-temperature characterization of sputtered polycrystalline bismuth selenide. *Applied Physics Letters*, 112(12), 2018.

[61] Xingyue Peng. *Charge-spin Transport in Surface-disordered Three-dimensional Topological Insulators*. University of California, Davis, 2016.

[62] Yasen Hou. *Study of Ion, Exciton, and Trapped Charge Transport in Nanostructures Via Photocurrent Mapping*. University of California, Davis, 2020.

[63] Jun Yin, Harish NS Krishnamoorthy, Giorgio Adamo, Alexander M Dubrovkin, Yidong Chong, Nikolay I Zheludev, and Cesare Soci. Plasmonics of topological insulators at optical frequencies. *NPG Asia Materials*, 9(8):e425–e425, 2017.

[64] John M Blatt, KW Böer, and Werner Brandt. Bose-einstein condensation of excitons. *Physical Review*, 126(5):1691, 1962.

[65] D Snoke, S Denev, Y Liu, L Pfeiffer, and K West. Long-range transport in excitonic dark states in coupled quantum wells. *Nature*, 418(6899):754–757, 2002.

[66] Hongki Min, Rafi Bistritzer, Jung-Jung Su, and AH MacDonald. Room-temperature superfluidity in graphene bilayers. *Physical Review B*, 78(12):121401, 2008.

[67] JIA Li, T Taniguchi, K Watanabe, J Hone, and CR Dean. Excitonic superfluid phase in double bilayer graphene. *Nature Physics*, 13(8):751–755, 2017.

[68] P Nozieres and C Comte. Exciton bose condensation: the ground state of an electron-hole gas-ii. spin states, screening and band structure effects. *Journal de Physique*, 43(7):1083–1098, 1982.

[69] Wang Yao, Di Xiao, and Qian Niu. Valley-dependent optoelectronics from inversion symmetry breaking. *Physical Review B*, 77(23):235406, 2008.

[70] Jens Christian Johannsen, Søren Ulstrup, Federico Cilento, Alberto Crepaldi, Michele Zacchigna, Cephise Cacho, IC Edmond Turcu, Emma Springate, Felix Fromm, Christian Raidel, et al. Direct view of hot carrier dynamics in graphene. *Physical Review Letters*, 111(2):027403, 2013.

[71] Siyuan Zhu, Yukiaki Ishida, Kenta Kuroda, Kazuki Sumida, Mao Ye, Jiajia Wang, Hong Pan, Masaki Taniguchi, Shan Qiao, Shik Shin, et al. Ultrafast electron dynamics at the dirac node of the topological insulator sb2te3. *Scientific reports*, 5(1):13213, 2015.

[72] Madhab Neupane, Su-Yang Xu, Yukiaki Ishida, Shuang Jia, Benjamin M Fregoso, Chang Liu, Ilya Belopolski, Guang Bian, Nasser Alidoust, Tomasz Durakiewicz, et al. Gigantic surface lifetime of an intrinsic topological insulator. *Physical review letters*, 115(11):116801, 2015.

[73] Rui Wang, Onur Erten, Baigeng Wang, and DY Xing. Prediction of a topological p+ ip excitonic insulator with parity anomaly. *Nature communications*, 10(1):1–9, 2019.

[74] Rong Rong, Ying Liu, Xuchen Nie, Wei Zhang, Zhuhua Zhang, Yanpeng Liu, and Wanlin Guo. The interaction of 2d materials with circularly polarized light. *Advanced Science*, 10(10):2206191, 2023.

[75] Longlong Zhang and Yuying Hao. Helicity-dependent all-optical switching based on the self-trapped triplet excitons. *Applied Physics Letters*, 118(9), 2021.

[76] Henry Travaglini and Dong Yu. Nonlocal helicity dependent photocurrent response in topological insulators. In *APS March Meeting Abstracts*, volume 2022, pages Z52–011, 2022.

[77] Ryo Mori, Samuel Ciocys, Kazuaki Takasan, Ping Ai, Kayla Currier, Takahiro Morimoto, Joel E Moore, and Alessandra Lanzara. Spin-polarized spatially indirect excitons in a topological insulator. *Nature*, 614(7947):249–255, 2023.

[78] Donna Strickland and Gerard Mourou. Compression of amplified chirped optical pulses. *Optics communications*, 55(6):447–449, 1985.

[79] Ferenc Krausz and Misha Ivanov. Attosecond physics. *Reviews of modern physics*, 81(1):163, 2009.

[80] Kathrin Klünder, JM Dahlström, Mathieu Gisselbrecht, Thomas Fordell, Marko Swoboda, Diego Guenot, Per Johnsson, Jérémie Caillat, Johan Mauritsson, A Maquet, et al. Probing single-photon ionization on the attosecond time scale. *Physical Review Letters*, 106(14):143002, 2011.

[81] Theodore C Oakberg. Magneto-optic kerr effect. *Hinds Instruments*, 1(1), 2005.

[82] DR THEODORE C OAKBERG. Using a mechanical chopper with a pem to measure v. 2005.

[83] Peter F Moulton. Spectroscopic and laser characteristics of ti: Al 2 o 3. *JOSA B*, 3(1):125–133, 1986.

[84] MO Scully, MS Zubairy, et al. Quantum optics cambridge university press. *Cambridge, CB2 2RU, UK*, 1997.

[85] P Michler, A Imamoğlu, MD Mason, PJ Carson, GF Strouse, and SK Buratto. Quantum correlation among photons from a single quantum dot at room temperature. *Nature*, 406(6799):968–970, 2000.

[86] Zhouxiaosong Zeng, Yufan Wang, Anlian Pan, and Xiao Wang. Ultrafast photocurrent detection in low-dimensional materials. *physica status solidi (RRL)*, page 2300120, 2023.

[87] Qiong Ma, Roshan Krishna Kumar, Su-Yang Xu, Frank HL Koppens, and Justin CW Song. Photocurrent as a multiphysics diagnostic of quantum materials. *Nature Reviews Physics*, 5(3):170–184, 2023.

[88] Kuan-Chun Lin, Ming-Yang Li, DC Ling, CC Chi, and Jeng-Chung Chen. Evolution of hot carrier dynamics in graphene with the fermi level tuned across the dirac point. *Physical Review B*, 91(12):125440, 2015.

[89] Lan Jiang and Hai-Lung Tsai. Improved two-temperature model and its application in ultrashort laser heating of metal films. 2005.

[90] TQ Qiu and CL Tien. Short-pulse laser heating on metals. *International Journal of Heat and Mass Transfer*, 35(3):719–726, 1992.

[91] JK Chen, DY Tzou, and JE Beraun. A semiclassical two-temperature model for ultrafast laser heating. *International journal of heat and mass transfer*, 49(1-2):307–316, 2006.

[92] GE Shoemake, JA Rayne, and RW Ure Jr. Specific heat of n-and p-type bi 2 te 3 from 1.4 to 90 k. *Physical Review*, 185(3):1046, 1969.

[93] Mauricio Segovia and Xianfan Xu. High accuracy ultrafast spatiotemporal pump–probe measurement of electrical thermal transport in thin film gold. *Nano Letters*, 21(17):7228–7235, 2021.

[94] Giriraj Jnawali, Samuel Linser, Iraj Abbasian Shojaei, Seyyedesadaf Pournia, Howard E Jackson, Leigh M Smith, Ryan F Need, and Stephen D Wilson. Revealing optical transitions and carrier recombination dynamics within the bulk band structure of bi2se3. *Nano letters*, 18(9):5875–5884, 2018.

[95] Dong Sun, Grant Aivazian, Aaron M Jones, Jason S Ross, Wang Yao, David Cobden, and Xiaodong Xu. Ultrafast hot-carrier-dominated photocurrent in graphene. *Nature nanotechnology*, 7(2):114–118, 2012.

[96] RD Averitt and AJ Taylor. Ultrafast optical and far-infrared quasiparticle dynamics in correlated electron materials. *Journal of Physics: Condensed Matter*, 14(50):R1357, 2002.

[97] Yuri D Glinka, Sercan Babakiray, Trent A Johnson, Mikel B Holcomb, and David Lederman. Effect of carrier recombination on ultrafast carrier dynamics in thin films of the topological insulator bi2se3. *Applied Physics Letters*, 105(17), 2014.

[98] Utku Uzun, Caterina Lamuta, and Mehmet Yetmez. Friction and wear characteristics of bismuth selenide topological insulator. *Materials letters*, 344:134402, 2023.

[99] Yu-Ting Wang, Chih-Wei Luo, Atsushi Yabushita, Kaung-Hsiung Wu, Takayoshi Kobayashi, Chang-Hsiao Chen, and Lain-Jong Li. Ultrafast multi-level logic gates with spin-valley coupled polarization anisotropy in monolayer mos2. *Scientific reports*, 5(1):8289, 2015.

[100] Kai Yao, Siqi Li, Zhiliang Liu, Yiran Ying, Petr Dvořák, Linfeng Fei, Tomáš Šikola, Haitao Huang, Peter Nordlander, Alex K-Y Jen, et al. Plasmon-induced trap filling at grain boundaries in perovskite solar cells. *Light: Science & Applications*, 10(1):219, 2021.

[101] Lin Fu, Hui Li, Lian Wang, Ruiyang Yin, Bo Li, and Longwei Yin. Defect passivation strategies in perovskites for an enhanced photovoltaic performance. *Energy & Environmental Science*, 13(11):4017–4056, 2020.

[102] John A Carr and Sumit Chaudhary. The identification, characterization and mitigation of defect states in organic photovoltaic devices: a review and outlook. *Energy & Environmental Science*, 6(12):3414–3438, 2013.

[103] Qingkai Qian, Guanhong Li, Yuanhao Jin, Junku Liu, Yuan Zou, Kaili Jiang, Shoushan Fan, and Qunqing Li. Trap-state-dominated suppression of electron conduction in carbon nanotube thin-film transistors. *ACS nano*, 8(9):9597–9605, 2014.

[104] Subhamoy Ghatak, Atindra Nath Pal, and Arindam Ghosh. Nature of electronic states in atomically thin mos2 field-effect transistors. *ACS nano*, 5(10):7707–7712, 2011.

[105] Yasen Hou, Rui Xiao, Senlei Li, Lang Wang, and Dong Yu. Nonlocal chemical potential modulation in topological insulators enabled by highly mobile trapped charges. *ACS Applied Electronic Materials*, 2(10):3436–3442, 2020.

[106] Didier Goguenheim, Dominique Vuillaume, Gilbert Vincent, and Noble M Johnson. Accurate measurements of capture cross sections of semiconductor insulator interface states by a trap-filling experiment: The charge-potential feedback effect. *Journal of applied physics*, 68(3):1104–1113, 1990.

[107] Mauro Aresti, Michele Saba, Roberto Piras, Daniela Marongiu, Guido Mula, Francesco Quochi, Andrea Mura, Carla Cannas, Mauro Mureddu, Andrea Ardu, et al. Colloidal bi2s3 nanocrystals: quantum size effects and midgap states. *Advanced Functional Materials*, 24(22):3341–3350, 2014.

[108] JW McIver, David Hsieh, Steven G Drapcho, Darius Hosseinzadeh Torchinsky, Dillon Richard Gardner, Young S Lee, and Nuh Gedik. Theoretical and experimental study of second harmonic generation from the surface of the topological insulator bi 2 se 3. *Physical Review B*, 86(3):035327, 2012.

[109] Gopinadhan Kalon, Young Jun Shin, Viet Giang Truong, Alan Kalitsov, and Hyunsoo Yang. The role of charge traps in inducing hysteresis: Capacitance–voltage measurements on top gated bilayer graphene. *Applied Physics Letters*, 99(8), 2011.

[110] D Carrad, AM Burke, D Waddington, R Lyttleton, HH Tan, PJ Reece, O Klochan, AR Hamilton, A Rai, D Reuter, et al. The origin of gate hysteresis in p-type si-doped algaas/gaas heterostructures. In *COMMAD 2012*, pages 9–10. IEEE, 2012.

[111] I Lundström, S Christensson, and C Svensson. Carrier trapping hysteresis in mos transistors. *Physica status solidi (a)*, 1(3):395–407, 1970.

[112] Sung-Min Joe and Jong-Ho Lee. Investigation of hysteresis phenomenon in floating-gate nand flash memory cells. *IEEE Transactions on Electron Devices*, 62(9):2738–2744, 2015.

[113] Simon M Sze, Yiming Li, and Kwok K Ng. *Physics of semiconductor devices*. John wiley & sons, 2021.

[114] Yujin Park and Byoungnam Park. Interfacial energy band bending and carrier trapping at the vacuum-deposited mapbi3 perovskite/gate dielectric interface. *Results in Physics*, 11:302–305, 2018.

[115] Amador Pérez-Tomás, A Fontserè, S Sánchez, MR Jennings, PM Gammon, and Y Cordier. Gate traps inducing band-bending fluctuations on algan/gan heterojunction transistors. *Applied Physics Letters*, 102(2), 2013.

[116] Tyler Otto, Chris Miller, Jason Tolentino, Yao Liu, Matt Law, and Dong Yu. Gate-dependent carrier diffusion length in lead selenide quantum dot field-effect transistors. *Nano letters*, 13(8):3463–3469, 2013.

[117] Byung Hee Son, Jae-Ku Park, Jung Taek Hong, Ji-Yong Park, Soonil Lee, and Yeong Hwan Ahn. Imaging ultrafast carrier transport in nanoscale field-effect transistors. *ACS nano*, 8(11):11361–11368, 2014.

[118] Leonhard Prechtel, Li Song, Stephan Manus, Dieter Schuh, Werner Wegscheider, and Alexander W Holleitner. Time-resolved picosecond photocurrents in contacted carbon nanotubes. *Nano Letters*, 11(1):269–272, 2011.

[119] Katsumasa Yoshioka, Taro Wakamura, Masayuki Hashisaka, Kenji Watanabe, Takashi Taniguchi, and Norio Kumada. Ultrafast intrinsic optical-to-electrical conversion dynamics in a graphene photodetector. *Nature Photonics*, 16(10):718–723, 2022.

[120] Michelle M Gabriel, Erik M Grumstrup, Justin R Kirschbrown, Christopher W Pinion, Joseph D Christesen, David F Zigler, Emma EM Cating, James F Cahoon, and John M Papanikolas. Imaging charge separation and carrier recombination in nanowire pin junctions using ultrafast microscopy. *Nano letters*, 14(6):3079–3087, 2014.

[121] John Stewart Bell. *Speakable and unspeakable in quantum mechanics: Collected papers on quantum philosophy*. Cambridge university press, 2004.

[122] Hugh D Young, Roger A Freedman, TR Sandin, and A Lewis Ford. *University physics*, volume 9. Addison-Wesley Reading, MA, 1996.

[123] Yongfu Sun, Hao Cheng, Shan Gao, Qinghua Liu, Zhihu Sun, Chong Xiao, Changzheng Wu, Shiqiang Wei, and Yi Xie. Atomically thick bismuth selenide freestanding single layers achieving enhanced thermoelectric energy harvesting. *Journal of the American Chemical Society*, 134(50):20294–20297, 2012.

[124] Nevill F Mott. The basis of the electron theory of metals, with special reference to the transition metals. *Proceedings of the Physical Society. Section A*, 62(7):416, 1949.

[125] Nevill F Mott. The transition to the metallic state. *Philosophical Magazine*, 6(62):287–309, 1961.

[126] Euan Hendry, Mattijs Koeberg, and Mischa Bonn. Exciton and electron-hole plasma formation dynamics in zno. *Physical Review B*, 76(4):045214, 2007.

[127] Raffaele Resta. Thomas-fermi dielectric screening in semiconductors. *Physical Review B*, 16(6):2717, 1977.

[128] Charles Kittel and Paul McEuen. *Introduction to solid state physics*. John Wiley & Sons, 2018.

[129] WA Little. Possibility of synthesizing an organic superconductor. *Physical Review*, 134(6A):A1416, 1964.

[130] Philip W Anderson. Absence of diffusion in certain random lattices. *Physical review*, 109(5):1492, 1958.

[131] Gabriel Kotliar, Sergej Y Savrasov, Kristjan Haule, Viktor S Oudovenko, O Parcollet, and CA Marianetti. Electronic structure calculations with dynamical mean-field theory. *Reviews of Modern Physics*, 78(3):865, 2006.

[132] Daniele Guerci, Massimo Capone, and Michele Fabrizio. Exciton mott transition revisited. *Physical Review Materials*, 3(5):054605, 2019.

[133] André Schleife, Claudia Rödl, Frank Fuchs, Karsten Hannewald, and Friedhelm Bechstedt. Optical absorption in degenerately doped semiconductors: Mott transition or mahan excitons? *Physical review letters*, 107(23):236405, 2011.

[134] S Iwai, M Ono, A Maeda, H Matsuzaki, H Kishida, H Okamoto, and Y Tokura. Ultrafast optical switching to a metallic state by photoinduced mott transition in a halogen-bridged nickel-chain compound. *Physical review letters*, 91(5):057401, 2003.

[135] RW Helmes, TA Costi, and A Rosch. Mott transition of fermionic atoms in a three-dimensional optical trap. *Physical review letters*, 100(5):056403, 2008.

[136] Takeshi Suzuki and Ryo Shimano. Exciton mott transition in si revealed by terahertz spectroscopy. *Physical Review Letters*, 109(4):046402, 2012.

[137] Jagdeep Shah, M Combescot, and AH Dayem. Investigation of exciton-plasma mott transition in si. *Physical Review Letters*, 38(25):1497, 1977.

[138] Michael Stern, Valery Garmider, V Umansky, and Israel Bar-Joseph. Mott transition of excitons in coupled quantum wells. *Physical review letters*, 100(25):256402, 2008.

[139] Marijn AM Versteegh, Tim Kuis, HTC Stoof, and Jaap I Dijkhuis. Ultrafast screening and carrier dynamics in zno: Theory and experiment. *Physical Review B*, 84(3):035207, 2011.

[140] Sudeshna Sen, Patrick J Wong, and Andrew K Mitchell. The mott transition as a topological phase transition. *Physical Review B*, 102(8):081110, 2020.

[141] Stephan Rachel and Karyn Le Hur. Topological insulators and mott physics from the hubbard interaction. *Physical Review B*, 82(7):075106, 2010.

[142] Amal Medhi, Vijay B Shenoy, and HR Krishnamurthy. Synchronous and asynchronous mott transitions in topological insulator ribbons. *Physical Review B*, 85(23):235449, 2012.

[143] Tsuneya Yoshida, Robert Peters, Satoshi Fujimoto, and Norio Kawakami. Characterization of a topological mott insulator in one dimension. *Physical review letters*, 112(19):196404, 2014.

[144] Srinivas Raghu, Xiao-Liang Qi, Carsten Honerkamp, and Shou-Cheng Zhang. Topological mott insulators. *Physical review letters*, 100(15):156401, 2008.

[145] Matthew Brahlek, Nikesh Koirala, Namrata Bansal, and Seongshik Oh. Transport properties of topological insulators: Band bending, bulk metal-to-insulator transition, and weak anti-localization. *Solid State Communications*, 215:54–62, 2015.

[146] GD Mahan. Excitons in degenerate semiconductors. *Physical Review*, 153(3):882, 1967.

[147] Gerald D Mahan. Excitons in metals: Infinite hole mass. *Physical Review*, 163(3):612, 1967.

[148] Yuri D Glinka, Junzi Li, Tingchao He, and Xiao Wei Sun. Clarifying ultrafast carrier dynamics in ultrathin films of the topological insulator bi2se3 using transient absorption spectroscopy. *ACS Photonics*, 8(4):1191–1205, 2021.

[149] Wenqing Liu, Damien West, Liang He, Yongbing Xu, Jun Liu, Kejie Wang, Yong Wang, Gerrit Van Der Laan, Rong Zhang, Shengbai Zhang, et al. Atomic-scale magnetism of cr-doped bi2se3 thin film topological insulators. *ACS nano*, 9(10):10237–10243, 2015.

[150] Cui-Zu Chang and Mingda Li. Quantum anomalous hall effect in time-reversal-symmetry breaking topological insulators. *Journal of Physics: Condensed Matter*, 28(12):123002, 2016.

[151] Judy J Cha, James R Williams, Desheng Kong, Stefan Meister, Hailin Peng, Andrew J Bestwick, Patrick Gallagher, David Goldhaber-Gordon, and Yi Cui. Magnetic doping and kondo effect in bi2se3 nanoribbons. *Nano letters*, 10(3):1076–1081, 2010.

[152] Bushra Irfan and Ratnamala Chatterjee. Magneto-transport and kondo effect in cobalt doped bi2se3 topological insulators. *Applied Physics Letters*, 107(17), 2015.

[153] David Flötotto, Yuichi Ota, Yang Bai, Can Zhang, Kozo Okazaki, Akihiro Tsuzuki, Takahiro Hashimoto, James N Eckstein, Shik Shin, and Tai-Chang Chiang. Superconducting pairing of topological surface states in bismuth selenide films on niobium. *Science advances*, 4(4):eaar7214, 2018.

[154] Alex Taekyung Lee, Myung Joon Han, and Kyungwha Park. Magnetic proximity effect and spin-orbital texture at the bi 2 se 3/eus interface. *Physical Review B*, 90(15):155103, 2014.

[155] Jonas A Krieger, Yunbo Ou, Marco Caputo, Alla Chikina, Max Döbeli, M-A Husanu, I Keren, Thomas Prokscha, Andreas Suter, Cui-Zu Chang, et al. Do topology and ferromagnetism cooperate at the eus/bi 2 se 3 interface? *Physical Review B*, 99(6):064423, 2019.

[156] AA Taskin, Satoshi Sasaki, Kouji Segawa, and Yoichi Ando. Achieving surface quantum oscillations in topological insulator thin films of bi2se3. *Advanced Materials*, 24(41):5581–5585, 2012.

[157] Liang Yang, Zhenhua Wang, Mingze Li, Xuan PA Gao, and Zhidong Zhang. The dimensional crossover of quantum transport properties in few-layered bi 2 se 3 thin films. *Nanoscale Advances*, 1(6):2303–2310, 2019.

[158] Devendra Kumar and Archana Lakhani. Large linear magnetoresistance from neutral defects in bi2se3 single crystal. *physica status solidi (RRL)–Rapid Research Letters*, 12(12):1800088, 2018.

[159] Sourabh Singh, RK Gopal, Jit Sarkar, Atul Pandey, Bhavesh G Patel, and Chiranjib Mitra. Linear magnetoresistance and surface to bulk coupling in topological insulator thin films. *Journal of Physics: Condensed Matter*, 29(50):505601, 2017.

[160] Ferdinand Kisslinger, Christian Ott, and Heiko B Weber. Origin of nonsaturating linear magnetoresistivity. *Physical Review B*, 95(2):024204, 2017.

[161] Rahul Singh, Vinod K Gangwar, DD Daga, Abhishek Singh, AK Ghosh, Manoranjan Kumar, A Lakhani, Rajeev Singh, and Sandip Chatterjee. Unusual negative magnetoresistance in bi2se3–ysy topological insulator under perpendicular magnetic field. *Applied Physics Letters*, 112(10), 2018.

[162] Praveen Deorani, Jaesung Son, Karan Banerjee, Nikesh Koirala, Matthew Brahlek, Seongshik Oh, and Hyunsoo Yang. Observation of inverse spin hall effect in bismuth selenide. *Physical Review B*, 90(9):094403, 2014.

[163] Mahdi Jamali, Joon Sue Lee, Jong Seok Jeong, Farzad Mahfouzi, Yang Lv, Zhengyang Zhao, Branislav K Nikolic, K Andre Mkhoyan, Nitin Samarth, and Jian-Ping Wang. Giant spin pumping and inverse spin hall effect in the presence of surface and bulk spin- orbit coupling of topological insulator bi2se3. *Nano letters*, 15(10):7126–7132, 2015.

[164] Hailin Peng, Keji Lai, Desheng Kong, Stefan Meister, Yulin Chen, Xiao-Liang Qi, Shou-Cheng Zhang, Zhi-Xun Shen, and Yi Cui. Aharonov–bohm interference in topological insulator nanoribbons. *Nature materials*, 9(3):225–229, 2010.

[165] Hai-Zhou Lu and Shun-Qing Shen. Weak localization and weak anti-localization in topological insulators. In *Spintronics Vii*, volume 9167, pages 263–273. SPIE, 2014.

[166] Hai-Zhou Lu and Shun-Qing Shen. Finite-temperature conductivity and magnetoconductivity of topological insulators. *Physical review letters*, 112(14):146601, 2014.

[167] Yong Seung Kim, Matthew Brahlek, Namrata Bansal, Eliav Edrey, Gary A Kapilevich, Keiko Iida, Makoto Tanimura, Yoichi Horibe, Sang-Wook Cheong, and Seongshik Oh. Thickness-dependent bulk properties and weak antilocalization effect in topological insulator bi 2 se 3. *Physical Review B*, 84(7):073109, 2011.

[168] Minhao Liu, Jinsong Zhang, Cui-Zu Chang, Zuocheng Zhang, Xiao Feng, Kang Li, Ke He, Li-li Wang, Xi Chen, Xi Dai, et al. Crossover between weak antilocalization and weak localization in a magnetically doped topological insulator. *Physical review letters*, 108(3):036805, 2012.

[169] Duming Zhang, Anthony Richardella, David W Rench, Su-Yang Xu, Abhinav Kandala, Thomas C Flanagan, Haim Beidenkopf, Andrew L Yeats, Bob B Buckley, Paul V Klimov, et al. Interplay between ferromagnetism, surface states, and quantum corrections in a magnetically doped topological insulator. *Physical Review B*, 86(20):205127, 2012.

[170] Qi I Yang, Merav Dolev, Li Zhang, Jinfeng Zhao, Alexander D Fried, Elizabeth Schemm, Min Liu, Alexander Palevski, Ann F Marshall, Subhash H Risbud, et al. Emerging weak localization effects on a topological insulator–insulating ferromagnet (bi 2 se 3-eus) interface. *Physical Review B*, 88(8):081407, 2013.

[171] Murong Lang, Liang He, Xufeng Kou, Pramey Upadhyaya, Yabin Fan, Hao Chu, Ying Jiang, Jens H Bardarson, Wanjun Jiang, Eun Sang Choi, et al. Competing weak localization and weak antilocalization in ultrathin topological insulators. *Nano letters*, 13(1):48–53, 2013.

[172] Ion Garate and Leonid Glazman. Weak localization and antilocalization in topological insulator thin films with coherent bulk-surface coupling. *Physical Review B*, 86(3):035422, 2012.

[173] Shinobu Hikami, Anatoly I Larkin, and Yosuke Nagaoka. Spin-orbit interaction and magnetoresistance in the two dimensional random system. *Progress of Theoretical Physics*, 63(2):707–710, 1980.

[174] Jian Liao, Yunbo Ou, Haiwen Liu, Ke He, Xucun Ma, Qi-Kun Xue, and Yongqing Li. Enhanced electron dephasing in three-dimensional topological insulators. *Nature communications*, 8(1):16071, 2017.

[175] Judy J Cha, Desheng Kong, Seung-Sae Hong, James G Analytis, Keji Lai, and Yi Cui. Weak antilocalization in bi2 (se x te1–x) 3 nanoribbons and nanoplates. *Nano letters*, 12(2):1107–1111, 2012.

[176] Bascom S Deaver Jr and Gordon B Donaldson. An experimental demonstration of winding number dependence of the aharonov-bohm effect. *Physics Letters A*, 89(4):178–180, 1982.

[177] Akira Inomata. Remarks on the experiment of winding number dependence of the aharonov-bohm effect. *Physics Letters A*, 95(3-4):176–178, 1983.

[178] Adrian Bachtold, Christoph Strunk, Jean-Paul Salvetat, Jean-Marc Bonard, Laszló Forró, Thomas Nussbaumer, and Christian Schönenberger. Aharonov–bohm oscillations in carbon nanotubes. *Nature*, 397(6721):673–675, 1999.

[179] Hiroshi Ajiki and Tsuneya Ando. Aharonov-bohm effect in carbon nanotubes. *Physica B: Condensed Matter*, 201:349–352, 1994.

[180] G Timp, AM Chang, JE Cunningham, TY Chang, P Mankiewich, R Behringer, and RE Howard. Observation of the aharonov-bohm effect for ω c τ¿ 1. *Physical review letters*, 58(26):2814, 1987.

[181] Alexander Van Oudenaarden, Michel H Devoret, Yu V Nazarov, and JE Mooij. Magneto-electric aharonov–bohm effect in metal rings. *Nature*, 391(6669):768–770, 1998.

[182] M Tsubota, K Inagaki, T Matsuura, and S Tanda. Aharonov-bohm effect in charge-density wave loops with inherent temporal current switching. *Europhysics Letters*, 97(5):57011, 2012.

[183] B Bucher, P Steiner, and P Wachter. Excitonic insulator phase in tmse 0.45 te 0.55. *Physical review letters*, 67(19):2717, 1991.

[184] W Yu, Vito Clericò, C Hernández Fuentevilla, Xiaoyan Shi, Y Jiang, D Saha, Wen-Kai Lou, Kai Chang, DH Huang, Godfrey Gumbs, et al. Anomalously large resistance at the charge neutrality point in a zero-gap inas/gasb bilayer. *New Journal of Physics*, 20(5):053062, 2018.

[185] William Boncher, Haydee Dalafu, Nicholas Rosa, and Sarah Stoll. Europium chalcogenide magnetic semiconductor nanostructures. *Coordination Chemistry Reviews*, 289:279–288, 2015.

[186] AV Matetskiy, IA Kibirev, T Hirahara, S Hasegawa, AV Zotov, and AA Saranin. Direct observation of a gap opening in topological interface states of mnse/bi2se3 heterostructure. *Applied Physics Letters*, 107(9), 2015.

[187] Weidong Luo and Xiao-Liang Qi. Massive dirac surface states in topological insulator/magnetic insulator heterostructures. *Physical Review B*, 87(8):085431, 2013.

[188] TR McGuire, e BE Argyle, r MW Shafer, and JS Smart. Magnetic properties of some divalent europium compounds. *Journal of Applied Physics*, 34(4):1345–1346, 1963.

[189] Jingyun Zou, Yumeng Yang, Dianyi Hu, Lixing Kang, Chao Zhu, Dan Tian, Xiaodong Lv, Govindan Kutty, Yuxi Guo, Manzhang Xu, et al. Controlled growth of ultrathin ferromagnetic β-mnse semiconductor. *SmartMat*, 3(3):482–490, 2022.

[190] Subramanian Mathimalar, Satyaki Sasmal, Archit Bhardwaj, Sekar Abhaya, Rajasekhar Pothala, Saurabh Chaudhary, Biswarup Satpati, and Karthik V Raman. Sig-

nature of gate-controlled magnetism and localization effects at bi2se3/eus interface. *npj Quantum Materials*, 5(1):64, 2020.

[191] Hong-Seok Kim, Tae-Ha Hwang, Nam-Hee Kim, Yasen Hou, Dong Yu, H-S Sim, and Yong-Joo Doh. Adjustable quantum interference oscillations in sb-doped bi2se3 topological insulator nanoribbons. *ACS nano*, 14(10):14118–14125, 2020.

[192] Jens H Bardarson, PW Brouwer, and JE Moore. Aharonov-bohm oscillations in disordered topological insulator nanowires. *Physical review letters*, 105(15):156803, 2010.

[193] RA Römer and ME Raikh. Aharonov-bohm effect for an exciton. *Physical Review B*, 62(11):7045, 2000.

[194] Seung Sae Hong, Yi Zhang, Judy J Cha, Xiao-Liang Qi, and Yi Cui. One-dimensional helical transport in topological insulator nanowire interferometers. *Nano letters*, 14(5):2815–2821, 2014.

[195] Dohun Kim, Paul Syers, Nicholas P Butch, Johnpierre Paglione, and Michael S Fuhrer. Coherent topological transport on the surface of bi2se3. *Nature communications*, 4(1):2040, 2013.

[196] Alexander Pergament. Metal–insulator transition: the mott criterion and coherence length. *Journal of Physics: Condensed Matter*, 15(19):3217, 2003.

[197] Pete Singer. A reality check with intel. *Solid State Technology*, 52(11):3–4, 2009.

[198] David Awschalom, Daniel Loss, and Nitin Samarth. *Semiconductor spintronics and quantum computation*. Springer Science & Business Media, 2002.

[199] Julie Grollier, Damien Querlioz, KY Camsari, Karin Everschor-Sitte, Shunsuke Fukami, and Mark D Stiles. Neuromorphic spintronics. *Nature electronics*, 3(7):360–370, 2020.

[200] Yi Wang, Dapeng Zhu, Yang Wu, Yumeng Yang, Jiawei Yu, Rajagopalan Ramaswamy, Rahul Mishra, Shuyuan Shi, Mehrdad Elyasi, Kie-Leong Teo, et al. Room temperature magnetization switching in topological insulator-ferromagnet heterostructures by spin-orbit torques. *Nature communications*, 8(1):1364, 2017.

[201] David Hsieh, Yuqi Xia, L Wray, Dong Qian, Arijeet Pal, JH Dil, J Osterwalder, F Meier, G Bihlmayer, CL Kane, et al. Observation of unconventional quantum spin textures in topological insulators. *Science*, 323(5916):919–922, 2009.

[202] Chris Jozwiak, Cheol-Hwan Park, Kenneth Gotlieb, Choongyu Hwang, Dung-Hai Lee, Steven G Louie, Jonathan D Denlinger, Costel R Rotundu, Robert J Birgeneau, Zahid Hussain, et al. Photoelectron spin-flipping and texture manipulation in a topological insulator. *Nature Physics*, 9(5):293–298, 2013.

[203] Alexandra Junck, Gil Refael, and Felix von Oppen. Photocurrent response of topological insulator surface states. *Physical Review B*, 88(7):075144, 2013.

[204] Dmitry Panna, Raja Marjieh, Evyatar Sabag, Leonid Rybak, Amit Ribak, Amit Kanigel, and Alex Hayat. Linear-optical access to topological insulator surface states. *Applied Physics Letters*, 110(21), 2017.

[205] JW McIver, David Hsieh, Hadar Steinberg, Pablo Jarillo-Herrero, and Nuh Gedik. Control over topological insulator photocurrents with light polarization. *Nature nanotechnology*, 7(2):96–100, 2012.

[206] Yua A Bychkov and É I Rashba. Properties of a 2d electron gas with lifted spectral degeneracy. *JETP lett*, 39(2):78, 1984.

[207] Dmytro Pesin and Allan H MacDonald. Spintronics and pseudospintronics in graphene and topological insulators. *Nature materials*, 11(5):409–416, 2012.

[208] Aurelien Manchon, Hyun Cheol Koo, Junsaku Nitta, Sergey M Frolov, and Rembert A Duine. New perspectives for rashba spin–orbit coupling. *Nature materials*, 14(9):871–882, 2015.

[209] MI Dyakonov and VI Perel. Spin relaxation of conduction electrons in noncentrosymmetric semiconductors. *Soviet Physics Solid State, Ussr*, 13(12):3023–3026, 1972.

[210] R _ J Elliott. Theory of the effect of spin-orbit coupling on magnetic resonance in some semiconductors. *Physical Review*, 96(2):266, 1954.

[211] Y Yafet. g factors and spin-lattice relaxation of conduction electrons. In *Solid state physics*, volume 14, pages 1–98. Elsevier, 1963.

[212] Hyun Cheol Koo, Jae Hyun Kwon, Jonghwa Eom, Joonyeon Chang, Suk Hee Han, and Mark Johnson. Control of spin precession in a spin-injected field effect transistor. *Science*, 325(5947):1515–1518, 2009.

[213] Michel I Dyakonov and AV Khaetskii. *Spin physics in semiconductors*, volume 1. Springer, 2008.

[214] Igor Žutić, Jaroslav Fabian, and S Das Sarma. Spintronics: Fundamentals and applications. *Reviews of modern physics*, 76(2):323, 2004.

[215] B Andrei Bernevig, J Orenstein, and Shou-Cheng Zhang. Exact su (2) symmetry and persistent spin helix in a spin-orbit coupled system. *Physical review letters*, 97(23):236601, 2006.

[216] Jake D Koralek, Christopher P Weber, Joe Orenstein, B Andrei Bernevig, Shou-Cheng Zhang, Shawn Mack, and DD Awschalom. Emergence of the persistent spin helix in semiconductor quantum wells. *Nature*, 458(7238):610–613, 2009.

[217] Mikhail I Dyakonov and VI Perel. Current-induced spin orientation of electrons in semiconductors. *Physics Letters A*, 35(6):459–460, 1971.

[218] Robert Karplus and JM Luttinger. Hall effect in ferromagnetics. *Physical Review*, 95(5):1154, 1954.

[219] Edurne Sagasta, Yasutomo Omori, Miren Isasa, Martin Gradhand, Luis E Hueso, Yasuhiro Niimi, YoshiChika Otani, and Fèlix Casanova. Tuning the spin hall effect of pt from the moderately dirty to the superclean regime. *Physical Review B*, 94(6):060412, 2016.

[220] Mikhail I Dyakonov. Possibility of orienting electron spins with current. *JETP Lett. USSR*, 13:467, 1971.

[221] JE Hirsch. Spin hall effect. *Physical review letters*, 83(9):1834, 1999.

[222] YD Chong. Berry's phase and the anomalous velocity of bloch wavepackets. *Physical Review B*, 81(5):052303, 2010.

[223] Jairo Sinova, Sergio O Valenzuela, Jörg Wunderlich, CH Back, and T Jungwirth. Spin hall effects. *Reviews of modern physics*, 87(4):1213, 2015.

[224] Di Xiao, Ming-Che Chang, and Qian Niu. Berry phase effects on electronic properties. *Reviews of modern physics*, 82(3):1959, 2010.

[225] Yuichiro K Kato, Roberto C Myers, Arthur C Gossard, and David D Awschalom. Observation of the spin hall effect in semiconductors. *science*, 306(5703):1910–1913, 2004.

[226] NS Averkiev and MI Dyakonov. Current due to nonhomogeneous spin orientation in semiconductors. *JETP Lett*, 35:196, 1983.

[227] AA Bakun, BP Zakharchenya, AA Rogachev, MN Tkachuk, and VG Fleisher. Observation of a surface photocurrent caused by optical orientation of electrons in a semiconductor. *JETP Lett*, 40(11), 1984.

[228] O Mosendz, JE Pearson, FY Fradin, GEW Bauer, SD Bader, and A Hoffmann. Quantifying spin hall angles from spin pumping: Experiments and theory. *Physical review letters*, 104(4):046601, 2010.

[229] Andrew J Berger, Eric RJ Edwards, Hans T Nembach, Olof Karis, Mathias Weiler, and Thomas J Silva. Determination of the spin hall effect and the spin diffusion length of pt from self-consistent fitting of damping enhancement and inverse spin-orbit torque measurements. *Physical Review B*, 98(2):024402, 2018.

[230] Qi Lu, Ping Li, Zhixin Guo, Guohua Dong, Bin Peng, Xi Zha, Tai Min, Ziyao Zhou, and Ming Liu. Giant tunable spin hall angle in sputtered bi2se3 controlled by an electric field. *Nature communications*, 13(1):1650, 2022.

[231] Mahendra Dc, Jun-Yang Chen, Thomas Peterson, Protuysh Sahu, Bin Ma, Naser Mousavi, Ramesh Harjani, and Jian-Ping Wang. Observation of high spin-to-charge conversion by sputtered bismuth selenide thin films at room temperature. *Nano letters*, 19(8):4836–4844, 2019.

[232] Jinling Yu, Xiaolin Zeng, Liguo Zhang, Chunming Yin, Yonghai Chen, Yu Liu, Shuying Cheng, Yunfeng Lai, Ke He, and Qikun Xue. Inverse spin hall effect induced by linearly polarized light in the topological insulator bi 2 se 3. *Optics express*, 26(4):4832–4841, 2018.

[233] Yang Liu, Jean Besbas, Yi Wang, Pan He, Mengji Chen, Dapeng Zhu, Yang Wu, Jong Min Lee, Lan Wang, Jisoo Moon, et al. Direct visualization of current-induced spin accumulation in topological insulators. *Nature communications*, 9(1):1–6, 2018.

[234] Jinling Yu, Xiaolin Zeng, Liguo Zhang, Ke He, Shuying Cheng, Yunfeng Lai, Wei Huang, Yonghai Chen, Chunming Yin, and Qikun Xue. Photoinduced inverse spin hall effect of surface states in the topological insulator bi2se3. *Nano letters*, 17(12):7878–7885, 2017.

[235] Jinling Yu, Lijia Xia, Kejing Zhu, Qinggao Pan, Xiaolin Zeng, Yonghai Chen, Yu Liu, Chunming Yin, Shuying Cheng, Yunfeng Lai, et al. Control of circular photogalvanic effect of surface states in the topological insulator bi2te3 via spin injection. *ACS applied materials & interfaces*, 12(15):18091–18100, 2020.

[236] Rui Sun, Shijia Yang, Xu Yang, A Kumar, Eric Vetter, Wenhua Xue, Yan Li, Na Li, Yang Li, Shihao Zhang, et al. Visualizing tailored spin phenomena in a reduced-dimensional topological superlattice. *Advanced Materials*, 32(49):2005315, 2020.

[237] Youwei Zhang, Hui Li, Lu Wang, Haomin Wang, Xiaomin Xie, Shi-Li Zhang, Ran Liu, and Zhi-Jun Qiu. Photothermoelectric and photovoltaic effects both present in mos2. *Scientific reports*, 5(1):7938, 2015.

[238] Hadas Soifer, Alexandre Gauthier, Alexander F Kemper, Costel R Rotundu, S-L Yang, Hongyu Xiong, Donghui Lu, Makoto Hashimoto, Patrick S Kirchmann, Jonathan A Sobota, et al. Band-resolved imaging of photocurrent in a topological insulator. *Physical Review Letters*, 122(16):167401, 2019.

[239] Viktor Iosifovich Belinicher and Boris Itskhakovich Sturman. The photogalvanic effect in media lacking a center of symmetry. *Soviet Physics Uspekhi*, 23(3):199, 1980.

[240] Jessica L Boland, Djamshid A Damry, Chelsea Q Xia, Piet Schonherr, Dharmalingam Prabhakaran, Laura M Herz, Thorsten Hesjedal, and Michael B Johnston. Narrow-

band, angle-tunable, helicity-dependent terahertz emission from nanowires of the topological dirac semimetal cd3as2. *ACS photonics*, 10(5):1473–1484, 2023.

[241] NV Leppenen and LE Golub. Linear photogalvanic effect in surface states of topological insulators. *Physical Review B*, 107(16):L161403, 2023.

[242] Zhurun Ji, Gerui Liu, Zachariah Addison, Wenjing Liu, Peng Yu, Heng Gao, Zheng Liu, Andrew M Rappe, Charles L Kane, Eugene J Mele, et al. Spatially dispersive circular photogalvanic effect in a weyl semimetal. *Nature materials*, 18(9):955–962, 2019.

[243] Fernando De Juan, Adolfo G Grushin, Takahiro Morimoto, and Joel E Moore. Quantized circular photogalvanic effect in weyl semimetals. *Nature communications*, 8(1):15995, 2017.

[244] Helene Plank, LE Golub, S Bauer, VV Bel'kov, Tobias Herrmann, P Olbrich, M Eschbach, L Plucinski, CM Schneider, J Kampmeier, et al. Photon drag effect in (bi 1- x sb x) 2 te 3 three-dimensional topological insulators. *Physical Review B*, 93(12):125434, 2016.

[245] Yu Xia, Min Li, Aifeng Wang, Xiaodan Tang, Mingyang He, Haihui Lv, Ling Zhang, Shuai Yuan, Xiaoyuan Zhou, and Heping Zeng. Highly efficient terahertz emission from layered zrte5 crystal with strong anisotropy and high in-plane carrier mobility. *Journal of Luminescence*, 241:118487, 2022.

[246] Ralph von Baltz and Wolfgang Kraut. Theory of the bulk photovoltaic effect in pure crystals. *Physical Review B*, 23(10):5590, 1981.

[247] Boris Itskhakovich Sturman. Ballistic and shift currents in the bulk photovoltaic effect theory. *Physics-Uspekhi*, 63(4):407, 2020.

[248] Benjamin M Fregoso, Rodrigo A Muniz, and JE Sipe. Jerk current: A novel bulk photovoltaic effect. *Physical review letters*, 121(17):176604, 2018.

[249] GB Ventura, DJ Passos, JM Viana Parente Lopes, and JMB Lopes Dos Santos. Comment on "jerk current: A novel bulk photovoltaic effect". *Physical Review Letters*, 126(25):259701, 2021.

[250] Pavan Hosur. Circular photogalvanic effect on topological insulator surfaces: Berry-curvature-dependent response. *Physical Review B*, 83(3):035309, 2011.

[251] Jifa Tian, Cüneyt Şahin, Ireneusz Miotkowski, Michael E Flatté, and Yong P Chen. Opposite current-induced spin polarizations in bulk-metallic bi 2 se 3 and bulk-insulating bi 2 te 2 se topological insulator thin flakes. *Physical Review B*, 103(3):035412, 2021.

[252] David Hsieh, Dong Qian, Lewis Wray, Yiman Xia, Yew San Hor, Robert Joseph Cava, and M Zahid Hasan. A topological dirac insulator in a quantum spin hall phase. *Nature*, 452(7190):970–974, 2008.

[253] G Schmidt, D Ferrand, LW Molenkamp, AT Filip, and BJ Van Wees. Fundamental obstacle for electrical spin injection from a ferromagnetic metal into a diffusive semiconductor. *Physical Review B*, 62(8):R4790, 2000.

[254] EI Rashba. Theory of electrical spin injection: Tunnel contacts as a solution of the conductivity mismatch problem. *Physical Review B*, 62(24):R16267, 2000.

[255] Sergey D Ganichev and Wilhelm Prettl. Spin photocurrents in quantum wells. *Journal of physics: Condensed matter*, 15(20):R935, 2003.

[256] Kenta Kuroda, J Reimann, KA Kokh, OE Tereshchenko, A Kimura, J Güdde, and U Höfer. Ultrafast energy-and momentum-resolved surface dirac photocurrents in the topological insulator sb 2 te 3. *Physical Review B*, 95(8):081103, 2017.

[257] Shivaramakrishnan Pancharatnam. Achromatic combinations of birefringent plates: part i. an achromatic circular polarizer. In *Proceedings of the Indian Academy of Sciences-Section A*, volume 41, pages 130–136. Springer, 1955.

[258] Kuen Wai Tang, Bob Minyu Wang, Henry Clark Travaglini, and Dong Yu. Modeling of the photocurrent induced by inverse spin hall effect under local circularly polarized photoexcitation. *Physical Review B*, 104(20):205413, 2021.

[259] COMSOL Multiphysics. Introduction to comsol multiphysics®. *COMSOL Multiphysics, Burlington, MA, accessed Feb*, 9(2018):32, 1998.

[260] Di Fan, Rei Hobara, Ryota Akiyama, and Shuji Hasegawa. Inverse spin hall effect induced by asymmetric illumination of light in topological insulator b i 2 s e 3. *Physical Review Research*, 2(2):023055, 2020.

[261] C Ojeda-Aristizabal, MS Fuhrer, Nicholas P Butch, Johnpierre Paglione, and I Appelbaum. Towards spin injection from silicon into topological insulators: Schottky barrier between si and bi2se3. *Applied Physics Letters*, 101(2), 2012.

[262] Dieter K Schroder. *Semiconductor material and device characterization*. John Wiley & Sons, 2015.

[263] Amro Anwar, Bahram Nabet, James Culp, and Fransisco Castro. Effects of electron confinement on thermionic emission current in a modulation doped heterostructure. *Journal of applied physics*, 85(5):2663–2666, 1999.

[264] Bob Minyu Wang, Yuqing Zhu, Henry Clark Travaglini, Renzhi Sun, Sergey Y Savrasov, William Hahn, Klaus van Benthem, and Dong Yu. Spatially dispersive

helicity-dependent photocurrent in dirac semimetal cd 3 as 2 nanobelts. *Physical Review B*, 108(16):165405, 2023.

[265] Qinsheng Wang, Jingchuan Zheng, Yuan He, Jin Cao, Xin Liu, Maoyuan Wang, Junchao Ma, Jiawei Lai, Hong Lu, Shuang Jia, et al. Robust edge photocurrent response on layered type ii weyl semimetal wte2. *Nature communications*, 10(1):5736, 2019.

[266] Kui Yu and Kirk S Schanze. Commemorating the nobel prize in chemistry 2023 for the discovery and synthesis of quantum dots, 2023.

Appendix A: Cleanroom Lore

Lithography SOP

1. Bake wafer at 200C for 2 minutes to dehydrate surface
2. Spincoat wafer with LOR: 5000 RPM (no ramp) for 60 seconds, ensure that wafer is evenly coated with no air bubbles
3. Bake at 185 C for 5 minutes
4. Spincoat with S1813: 3000 RPM (5 seconds at 500 RPM) for 30 seconds with 500 rpm ramp rate
5. Bake wafer at 100C for 3 minutes
6. Expose with stepper or contact aligner
7. Develop in CD-26: 50 seconds
8. Rinse in DI water–DI water should be exchanged semi-frequently to prevent scumming of patterns
9. Bake at 100C to dehydrate surface
10. Deposit metals
11. Strip in 1165 indefinitely until liftoff is complete
12. Rinse in a fresh solution of 1165

13. Rinse in DI water and blow dry

After development, the patterns have residual photoresist: proper rinsing of the wafers following development is critical to avoid scumming. This can also be the result of dirty photomasks or improper wedge compensation and thus tends to be a biger issue with contact alignment.

The patterns have poor liftoff and/or significant fencing: this is caused by sidewall adhesion, which can be uniformly blamed on poor undercut formation. The proper choice of a copolymer (LOR 3A works very well) will eliminate this issue, but this can also be addressed by tuning the post-exposure bake (time and temperature) and development time if a monolayer photoresist is needed to minimize a pattern's critical feature size.